# Differential Absorption Lidar Measurements of Atmospheric Water Vapor Using a Pseudonoise Code Modulated AlGaAs Laser

Jonathan A. R. Rall
*NASA Goddard Space Flight Center*
*Greenbelt, Maryland*

DIFFERENTIAL ABSORPTION LIDAR MEASUREMENTS OF ATMOSPHERIC WATER VAPOR

USING A PSEUDONOISE CODE MODULATED AlGaAs LASER

BY

Jonathan A. R. Rall

## ABSTRACT

Lidar measurements using pseudonoise code modulated AlGaAs lasers are reported. Horizontal path lidar measurements were made at night to terrestrial targets at ranges of 5 and 13 km with 35 mW of average power and integration times of one second. Cloud and aerosol lidar measurements were made to thin cirrus clouds at 13 km altitude with Rayleigh (molecular) backscatter evident up to 9 km. Average transmitter power was 35 mW and measurement integration time was 20 minutes. An AlGaAs laser was used to characterize spectral properties of water vapor absorption lines at 811.617, 816.024, and 815.769 nm in a multipass absorption cell using derivative spectroscopy techniques. Frequency locking of an AlGaAs laser to a water vapor absorption line was achieved with a laser center frequency stability measured to better than one-fifth of the water vapor Doppler linewidth over several minutes. Differential absorption lidar measurements of atmospheric water vapor were made in both integrated path and range-resolved modes using an externally modulated AlGaAs laser. Mean water vapor number density was estimated from both integrated path and range-resolved DIAL measurements and agreed with measured humidity values to within 6.5% and 20%, respectively. Error sources were identified and their effects on estimates of water vapor number density calculated.

## ACKNOWLEDGMENTS

This dissertation reflects nearly four years of work performed in the Experimental Instrumentation Branch at NASA Goddard Space Flight Center. This work would not have been possible without the support and direction of Dr. James B. Abshire. It was his vision of applying AlGaAs laser technology, previously developed for a satellite laser communications program, to remote sensing of the atmosphere. I would also like to thank Dr. David E. Smith for "taking a chance" and bringing yet another engineer into the Laboratory for Terrestrial Physics.

I would like to acknowledge and thank the many people that contributed to the success of AlGaAs Lidar, particularly, Serdar S. Manizade, Lewis Wan, Inna Gorin, Dr. Daniel Reusser, and Michael Humphrey.

I would also like to acknowledge Paul L. Spadin, Jimmie D. Fitzgerald, and William H. Schaefer, the three people who were instrumental in my early "education" at NASA Goddard Space Flight Center.

I am deeply indebted to my parents, Col. & Mrs. Lloyd L. Rall, for the educational foundation that they provided me in my early years and the unwavering support even in my rebellious years. Finally, I would like to thank my wife, Dr. Allison F. Lung, for leading the way in this process and never compromising her integrity or dedication to quality in pursuit of a goal.

# TABLE OF CONTENTS

## LIST OF TABLES

# LIST OF ILLUSTRATIONS

# 1. INTRODUCTION & BACKGROUND

Water vapor comprises ≤3.0% of the Earth's atmosphere but is extremely important to both life processes and atmospheric physics. The importance to atmospheric physics is defined in a strategic research plan[1] developed during an October 1990 workshop held by the Global Energy and Water Cycle Experiment (GEWEX). Water vapor is: (1) by virtue of its latent heat transfer property, a principal medium by which energy is exchanged among the components of the Earth system, *i.e.* atmosphere, hydrosphere, cryosphere, and biosphere; (2) the predominant greenhouse gas, playing a crucial role in many radiative processes which regulate the global climate; and (3) essential in many atmospheric processes, *e.g.* cloud formation and precipitation, which determine climate variations, especially on regional scales. Currently, our lack of knowledge of the distribution of atmospheric water vapor and its variability prevents reliable assessment of potential regional or global climate change. This deficiency may be corrected through a combined campaign of observations and modeling of atmospheric water vapor.

## 1.1 Water vapor & global circulation modeling

Global circulation models (GCM's) attempt to parameterize all significant processes which drive atmospheric circulation. Since water vapor plays a major role in most of these processes, parameterization of moist processes is critical. Understanding these complex water vapor processes and developing parameters which accurately describe them requires a detailed knowledge of atmospheric water vapor distribution and

1

its variability. The desired spatial resolution is horizontal grids less than 200 km on a side and 1 km vertical layers up to the tropopause. The measurements should be temporally resolved to permit sensing of diurnal variations. Total column-content measurements are also needed to initialize these models with realistic total atmospheric water vapor content.

## 1.2  Current water vapor measurement techniques

A global upper air balloon sounding network provides regular radiosonde measurements of atmospheric water vapor.[2] These radiosondes have numerous short-comings. Geographical spacing of sounding sites is typically 400 km in North America and western Europe and sparse elsewhere. There is little or no radiosonde coverage over the oceans. Temporal resolution is also poor with measurements made at twelve hour intervals. Variation in sensor types and reporting practices used in different countries leads to significant uncertainties in humidity data. Almost no data is collected in the upper troposphere since measurement accuracy degrades at temperatures below -30°C and most sondes do not report in conditions less than -40°C.[3]

Satellite observations of water vapor provide more complete geographical coverage, improved temporal resolution, better horizontal resolution, and in some cases better vertical resolution compared to radiosondes. Current operational satellite techniques include passive infrared and microwave radiometers in both vertical and limb-scanning modes.

Passive infrared radiometers typically use several broadband infrared channels in the 6-14 $\mu$m region to observe water vapor radiance's from different layers of the atmosphere. An example is the High Resolution Infrared Spectrometer (HIRS/2)

instrument of the Tiros Operational Vertical Sounder (TOVS) investigation flown on the TIROS-N and NOAA 6 through 10 satellites.[4] The water vapor content at three vertical levels of the atmosphere may be calculated from these radiances. Unfortunately radiance observations are inhibited by cloud cover, therefore, water vapor profiles cannot be retrieved from overcast areas and are only estimated over partially cloudy areas. When used in a limb-scanning mode, radiometers such as the Stratospheric Aerosol & Gas Experiment (SAGE II) instrument on the Earth Radiation Budget Satellite (ERBS) can provide 1 km vertical resolution profiles of water vapor in the upper troposphere and stratosphere.[5] However, due to the tangential path geometry of the measurement, the horizontal resolution in this mode is poor. Also, since the limb-scanning or solar-occultation mode requires specific alignment of the sun, earth, and spacecraft the measurements have a limited coverage.

Passive microwave sounding instruments, *e.g.* Scanning Multichannel Microwave Radiometer (SMMR) on the Nimbus-7 satellite, make total column measurements of atmospheric water vapor over the oceans by measuring the differential absorption strength of water vapor between 18 and 21 GHz.[6] The accuracy of the column content measurements is considered to be better than ± 10%.[1] However, vertical profiles of water vapor cannot be obtained and measurements are not made over land, sea ice, or areas of precipitation.

### 1.3 Laser remote sensing of water vapor

There has been significant sustained interest in using laser remote sensing techniques to make measurements of atmospheric water vapor at high spatial and temporal resolution. The ultimate goal is making spaceborne measurements of atmospheric water vapor profiles and total column content. Most laser remote sensing

measurements of atmospheric water vapor have used either ground based Raman or differential absorption lidar (DIAL) approaches.

### 1.3.1 Raman lidar

Measurements of atmospheric water vapor profiles using Raman lidar were first reported by Melfi, Lawrence, and McCormick[7] and Cooney[8] using a second harmonic of a ruby laser and by Strauch, Derr, and Cupp[9] using a $N_2$ laser. The Raman scattering technique involves detecting radiation which has been shifted in wavelength due to interaction with the scattering molecule. This wavelength shift, or Stokes shift, is equal in energy to a vibrational-rotational or rotational transition in the scattering molecule. The backscattered power of the wavelength shifted signal is proportional to the concentration of Raman scattering molecules and inversely proportional to $\lambda^{-4}$. Thus, the primary advantage of Raman lidar is that it offers a direct measure of species concentration or mixing ratio by comparing the Raman signal of water vapor to the Raman signal of $N_2$ or $O_2$. However, Raman scattering is a very weak process and the Raman backscatter signal for water vapor is typically two to four orders of magnitude weaker than the elastic backscattered signal. This creates problems with isolating the inelastic scattering signal from the elastic backscatter.[10] Also, the weak scattering cross section typically limits water vapor Raman lidar to nighttime measurements at ranges of less than 10 km. To increase the Raman signal and make daytime measure-ments, high power lidar systems have been developed to operate at wavelengths from 248.5 to 268.5 nm. Unfortunately at these wavelengths absorption by molecular oxygen and ozone can attenuate the transmitted beam and solar irradiance can obscure the backscattered water vapor Raman signal.

4

## 1.3.2 Water vapor absorption spectroscopy

The water vapor DIAL technique employs elastic scattering of radiation by aerosols and molecules and absorption by water molecules to estimate the number density of atmospheric water vapor. The near-infrared spectrum of water vapor has many absorption lines with absorption line strengths spanning several orders of magnitude. There are three prominent water vapor absorption bands in the near infrared, centered at 720, 820, and 940 nm. Figure 1 is a plot of atmospheric transmission of solar irradiance calculated using the LOWTRAN database[11] and the 1976 U.S. Standard Atmosphere.

WAVENUMBER (cm^-1)
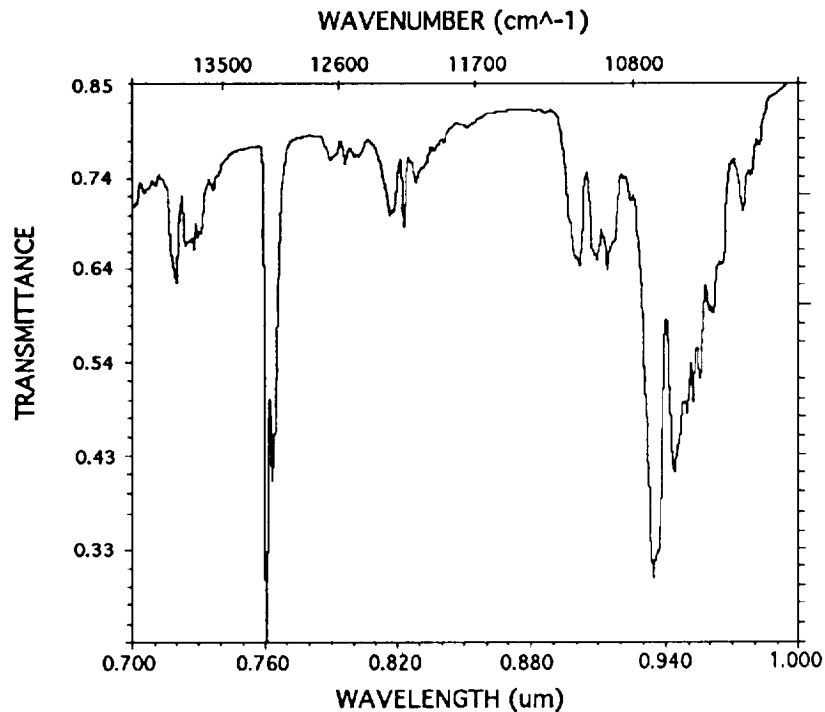
Figure 1. Atmospheric transmittance of solar irradiance from 0.7 - 1.0 μm. Vertical path through entire atmosphere as calculated with LOWTRAN

5

The strong absorption feature at 760 nm is due to the oxygen ($O_2$) A-band. The water vapor bands centered at 720, 820, and 940 nm correspond to electronic ground state, vibration-rotation (VR) transitions of the water molecule, a semi-rigid rotator, asymmetric top structure belonging to the symmetry point group $c_{2v}$.[12] The 720 and 940 nm bands have been extensively studied[13,14,15,16,17,18,19] while the 820 nm band has received less attention.[20] The prominent VR transitions in the 820 nm region originate in the $v_1v_2v_3$ = 211 vibration state and terminate in the vibration ground state, $v_1v_2v_3$ = 000. Figure 2, calculated using the HITRAN database and the 1976 U.S. Standard Atmosphere, shows atmospheric transmission for a wavenumber range 12000-12400 $cm^{-1}$ over a 5 km horizontal path at sea-level.
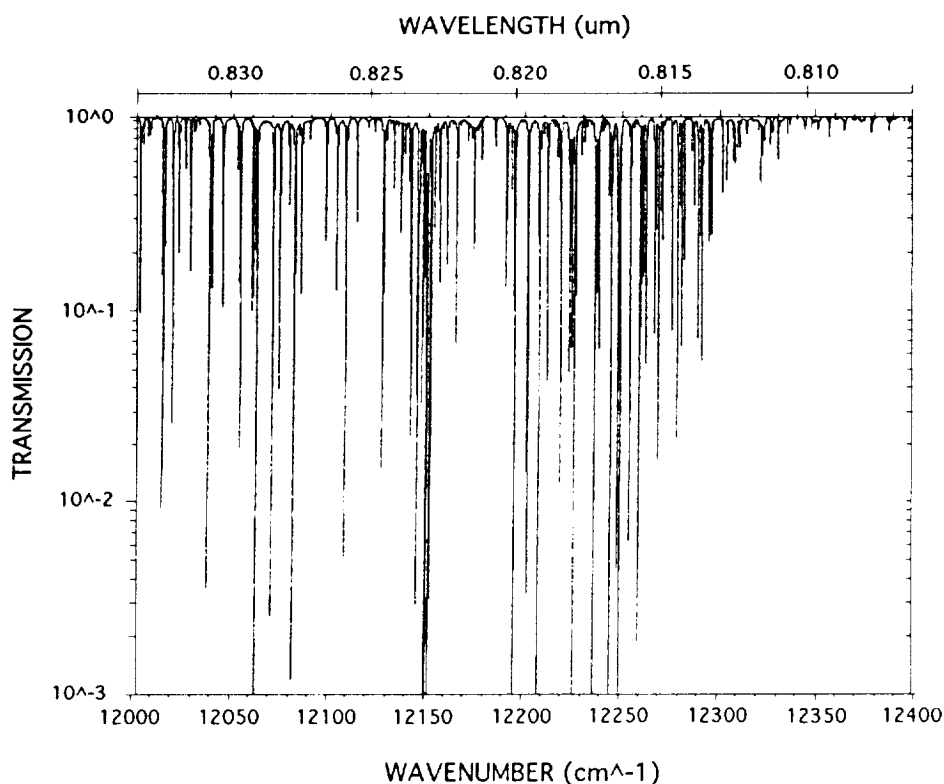


**Figure 2.** Atmospheric transmission spectra vs wavenumber showing individual water vapor lines for a 5 km horizontal path at sea level.

Figure 2 shows that individual water vapor absorption lines in this region are resolved. The specific line assignments are determined by the upper and lower state rotational quantum numbers $J', K'_a, K'_b$ & $J'', K''_a, K''_b$ , respectively, and are shown in Figure 3.
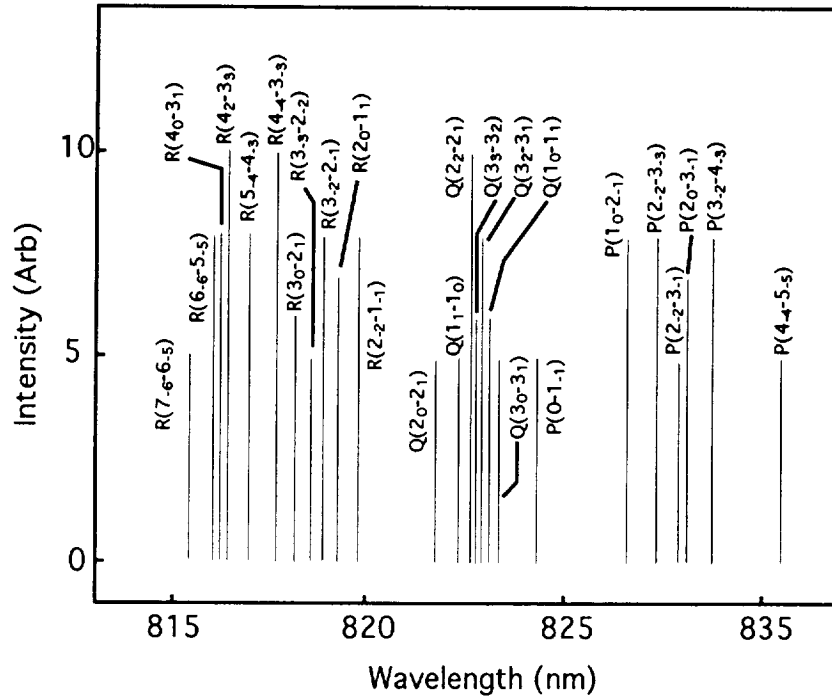


**Figure 3.** Line assignment and relative intensities of strong water vapor lines in the (2,1,1) band.[21]

The line assignments have been abbreviated using the notation $(J'_{\tau'} - J''_{\tau''})$ where $\tau' = (K'_a - K'_b)$. The $R$, $Q$, and $P$ branches correspond to $\Delta J = 1, 0, -1$, respectively.

The absorption cross section $\sigma$ for a particular water vapor absorption line is a function of wavelength, pressure, and temperature and can be expressed as the ratio of the line strength $S(T)$ to the Lorentz linewidth $\gamma(p,T)$[22]

$$\sigma(\lambda, p, T) = \frac{S(T)}{\pi \cdot \gamma(p,T)} \cdot f(\lambda - \lambda_m),$$ (1)

where $f(\lambda - \lambda_m)$ is the wavelength dependence of the cross section referenced to maximum absorption at $\lambda_m$. If the laser linewidth is one-fifth or less the width of the absorption line, then $f(\lambda - \lambda_m)$ may be taken as unity. In DIAL measurements, the on-line laser should be spectrally narrower than the absorption line of the atmospheric species of interest to maximize measurement sensitivity. Ponsardin et al. reported that the laser linewidth must be no larger than one-quarter of the absorption linewidth to ensure that no systematic error is made when estimating water vapor number density from DIAL lidar data.[23] Water vapor absorption lines in the 820 nm region typically have pressure broadened linewidths, at STP, of 1-5 GHz full width at half maximum (FWHM).

Atmospheric temperature and pressure vary with altitude, therefore the dependence of the absorption cross section on temperature and pressure as well as pressure shift of the absorption line center can be a significant source of error in water vapor DIAL measurements. Pressure broadening effects can be dealt with by using spectrally narrow lasers while pressure shift effects can be minimized by locking the laser to line center at lower pressures. This compensates for pressure induced shifts of the line center by locking the laser at a vapor pressure equivalent to a higher altitude. Temperature sensitive parameters have been derived for the 720 & 940 nm water vapor absorption bands.[14,16,18,19]

The 820 nm water vapor absorption band is attractive for atmospheric DIAL measurements due to the abundance of both strong and weak water vapor lines and the

availability of both photon counting detectors and high power AlGaAs laser diodes in this wavelength region. A large dynamic range of line strengths is required for DIAL measurements to accommodate various measurement ranges and varying water vapor concentrations.

### 1.3.3 Differential absorption lidar

Schotland first proposed measuring vertical distributions of atmospheric water vapor using DIAL techniques in 1966.[24] The DIAL technique employs two wavelengths to estimate atmospheric water vapor number density. One wavelength $\lambda_{on}$ is selected to coincide with the center of a water vapor absorption line while a second wavelength $\lambda_{off}$ is selected to fall in a nearby nonabsorbing region. If $\lambda_{on}$ and $\lambda_{off}$ are within a few $cm^{-1}$ of one another, then the elastic scattering properties of the atmosphere are assumed to be identical and can be neglected. Laser power at both wavelengths is transmitted into the atmosphere (either simultaneously or sequentially) and is elastically scattered by molecules and aerosols into the field of view (FOV) of the lidar receiver. Provided that the transmitted laser power is low and the receiver FOV is small, multiple scattering effects may be neglected. The received power $P(\lambda_L, R)$ of the scattered light, at each wavelength, $\lambda_{on}$ and $\lambda_{off}$, and range $R$, is given by the single scattering lidar equation[25]

$$P(\lambda_L, R) = P_L \, \frac{A_o}{R^2} \, \tau_{sys} \, \xi(R) \beta_\pi (\lambda_L, R) \Delta R \cdot e^{-2 \int_0^R \kappa(\lambda_L, R) dR}.$$  (2)

Here $P_L$ is the transmitted laser power, $A_o$ is the area of the telescope, $R$ is the range, $\tau_{sys}$ is the lidar system optical transmission, $\beta_\pi(\lambda_L, R)$ is the atmospheric backscatter

coefficient at range $R$ and $\lambda_L$, $\xi(R)$ is the overlap function of the laser divergence with the receiver FOV, $\Delta R = c\tau_L/2$ is the length of the atmospheric measurement cell, $\tau_L$ is the receiver integration time, and $\kappa(\lambda_L, R)$ is the total attenuation coefficient due to aerosol and molecular scattering and absorption.
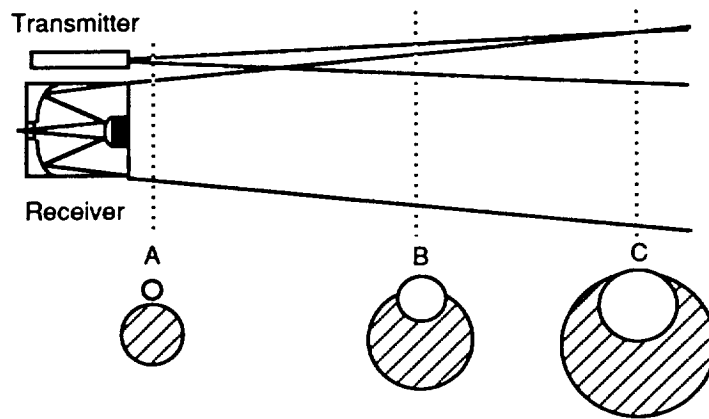


**Figure 4.** Overlap of laser transmitter and receiver FOV, (A) zero overlap, (B) partial overlap, and (C) complete overlap.

Biaxial lidar systems have separate transmitter and receiver optical paths which require that the transmitter and receiver be carefully aligned to one another. The overlap function, $\xi(R)$, gives the range dependence of transmitter energy crossing into the receiver FOV. The overlap function of a biaxial lidar is graphically depicted in Figure 4.

Equation (2) may be rearranged and simplified to give the expected received lidar signal in photoelectrons per second for a homogeneous atmospheric path. For most measurement ranges of interest, there is complete overlap ($\xi = 1$). The total attenuation coefficient for a homogeneous path can be broken into its constituents and the expected on-line photoelectron count rate $\dot{N}_{on}$ becomes

$$\dot{N}_{on}(\lambda_{on},R) = \frac{P_L \eta}{E_{ph}} \frac{A_0}{R^2} \tau_{sys} \beta_\pi (\lambda_{on},R) \Delta R \cdot e^{-2R(k_m+\sigma_m+k_a+\sigma_a)}.$$ (3)

Here $\eta$ is the quantum efficiency of the detector, $E_{ph} = hc/\lambda_L$ is the laser photon energy, $k_m$ is the water vapor absorption coefficient, $\sigma_m$ is the molecular scattering coefficient, $k_a$ is the aerosol absorption coefficient, and $\sigma_a$ is the aerosol scattering coefficient. Mean values for the volume backscatter coefficient, $\beta_\pi(\lambda_L,R)$, and individual attenuation coefficients have been measured and are catalogued as functions of wavelength, altitude, latitude, and season and are available from several sources.[26,27]

The DIAL technique can be used to estimate the number density of water vapor molecules at a specific range (range resolved) or the average for a path. The water vapor absorption cross section, $\sigma(cm^2)$, and water vapor absorption coefficient, $k_m(cm^{-1})$, are related by[25]

$$k_m(\lambda_L,R) = n(R) \cdot \sigma(\lambda_L,R),$$ (4)

where $n(R)$ is the number density of water vapor molecules in the atmosphere at range $R$.

When the laser is tuned off of the water vapor absorption line, the water vapor absorption coefficient $k_m = 0$, and the expected photoelectron count rate is

$$\dot{N}_{off}(\lambda_{off},R) = \frac{P_L \eta}{E_{ph}} \frac{A_0}{R^2} \tau_{sys} \beta_\pi (\lambda_{off},R) \Delta R \cdot e^{-2R(\sigma_m+k_a+\sigma_a)}.$$ (5)

The backscatter coefficient, $\beta_\pi(\lambda_L, R)$, which is assumed to be constant between $\lambda_{on}$ and $\lambda_{off}$, can be estimated from lidar measurements and the visibility or meteorological range representing the atmospheric conditions at the time of the measurement. The average number density of water vapor molecules, $n(\Delta R)$, in a single range bin defined as $\Delta R = R_2 - R_1$, can be expressed in a simplified DIAL equation. The DIAL equation is derived by taking $\ln\left(N_{on}/N_{off}\right)$ for a range $R_1$ and subtracting $\ln\left(N_{on}/N_{off}\right)$ for an adjacent range $R_2$, and solving for the water vapor absorption coefficient $k_m$. Using the difference in absorption cross section $\Delta\sigma$, the mean number density of water vapor between $R_1$ and $R_2$ can be expressed as

$$n(\Delta R) \cong \frac{1}{2\Delta\sigma \cdot \Delta R} \ln\left[\frac{N_{on}(R_1)N_{off}(R_2)}{N_{on}(R_2)N_{off}(R_1)}\right].$$

$(6)$

Here $\Delta\sigma = \sigma(\lambda_{on}) - \sigma(\lambda_{off})$ is the difference in water vapor absorption cross section between $\lambda_{on}$ and $\lambda_{off}$. $N_{on} = \dot{N}_{on}T$ and $N_{off} = \dot{N}_{off}T$ are the integrated photoelectron counts at $\lambda_{on}$ and $\lambda_{off}$ respectively, $T$ is the lidar measurements integration time, and $R_1$ and $R_2$ are ranges which define the boundaries of $\Delta R$, the range bin of interest.

Simulations of spaceborne water vapor DIAL measurements at night indicate that accuracy's of <10% with horizontal resolutions of 100 km and vertical resolutions of less than 1 km can be achieved with a 5 Hz, 150 mJ pulsed laser at 727 nm.[28] A nadir-pointing DIAL instrument using an alexandrite laser transmitter has recently measured water vapor profiles from a NASA research aircraft.[29]

12

Currently operational water vapor DIAL and Raman lidar systems use solid state, gas, dye, or excimer laser systems.[30] These laser transmitters are large, bulky and inefficient with complex optical pumping systems. Due to these limitations, these laser transmitters are not viable candidates for remote sensing applications where size, mass, and power are constrained.

## 1.4 AlGaAs lasers

Semiconductor AlGaAs laser diodes are much smaller and more efficient laser sources than there solid-state counter parts. Current single element, single longitudinal mode lasers are capable of reliably producing 200 mW of continuous power. Recent developments of master oscillator-power amplifier (MOPA) devices have boosted this CW power to the 1-10 W level. With continued improvements in power levels, MOPA devices based on AlGaAs semiconductor lasers, can be considered for aircraft and spaceborne DIAL remote sensing instruments. The emission wavelength of AlGaAs devices, between 780 and 860 nm, is well matched both to atmospheric water vapor absorption bands and to photomultipliers and silicon detectors.

Some of the earliest operational lasers were gallium arsenide (GaAs) homo-junction diodes which were cryogenically cooled.[31] However, due to high threshold current densities, cooling requirements, and erratic lifetimes, these early laser diodes were not practical for many applications. The introduction of aluminum to these devices, creating $Al_{(x)}Ga_{(1-x)}As$ compounds and the development of the double heterostructure (DH) geometry resolved both the high current density and reliability problems which plagued these early lasers.

AlGaAs has the useful property that the bandgap energy can be varied over a wide range by changing the $Al_{(x)}Ga_{(1-x)}$ ratio, with only a negligible change in lattice parameter. The lattice parameter, $a_o$, changes only 0.14 % when changing $Al_{(x)}Ga_{(1-x)}As$ from AlAs to GaAs. This substantially improved the reliability of AlGaAs lasers by reducing lattice mismatch while permitting a broad manufacturing range of the emission wavelength.

A potential barrier or quantum well which simultaneously confined the injected carriers and created a rectangular optical waveguide was created by burying the double heterostructure laser in undoped AlGaAs material and tailoring the bandgap. The waveguide confined the laser emission and reduced absorption losses in the GaAs substrate. Subsequent improvements in epitaxial layer growth, wafer material purity, and lattice matching resulted in lower threshold current densities and subsequently longer lived lasers. Current commercially available quantum well AlGaAs lasers are the smallest, most efficient, and least expensive lasers available, and have demonstrated lifetimes of greater than 30,000 hours.

However, single mode laser diodes are limited in the peak optical power that they can produce due to the possibility of catastrophic facet damage. Catastrophic facet damage is mechanical failure or melting of the facet due to intense optical fields.[31] The width of the emitting region and the pulse length are important factors which determine the power density level (watts/cm$^2$) at which failure occurs. With this limited capability to produce high peak powers, conventional short pulse lidar measurement techniques are not practical using single mode AlGaAs lasers. These lasers are, however, well suited for pseudonoise (PN) code modulation, which has a nearly 50% duty cycle

and whose noise-like correlation properties permit range resolved backscatter measurements.[32]

## 1.5 Pseudonoise (PN) codes

Maximal length pseudonoise codes (PN codes) are the longest non-repeating series of ones and zeroes that can be generated by a digital shift register of a given length.[32] Digital shift registers with feedback can be used to produce maximum length PN sequences of $2^n - 1$ bits, where $n$ is the number of stages of the shift register, and a bit is a single element (1 or 0) of the sequence. Long shift register code generators, typically 8 to 12 stages, produce more useful code lengths, from 255 to 4095 bits. PN code modulation affords range resolved measurements with range resolution determined by the modulation rate and a maximum unambiguous range determined by the code length.

A simplified block diagram of a PN code lidar system is shown in Figure 5 and is described as follows, a PN code modulated laser beam is transmitted through the atmosphere and a small fraction, less than one photon per bit, is backscattered into the receiver. The receiver detects these photons and synchronously accumulates a photoelectron count over $10^4$ to $10^6$ repetitions of the code. This received histogram is a record of counts versus time delay (range bins). The histogram represents the convolution of the atmospheric backscatter function with the transmitted code. Correlating the histogram with a stored version of the PN code yields the atmospheric lidar signal.

In PN code lidar, the correlation function is used to compute the lidar signal from the detected backscattered photons. The noise-like correlation properties of the PN code permit recovery of the lidar signal by cross-correlating the received histogram with

the transmitted sequence. The received stream of photons has been modified by the atmospheric path and target. Hence, the correlation function, which computes the lidar backscatter signal vs. range, contains atmospheric backscatter and absorption information as a function of range.
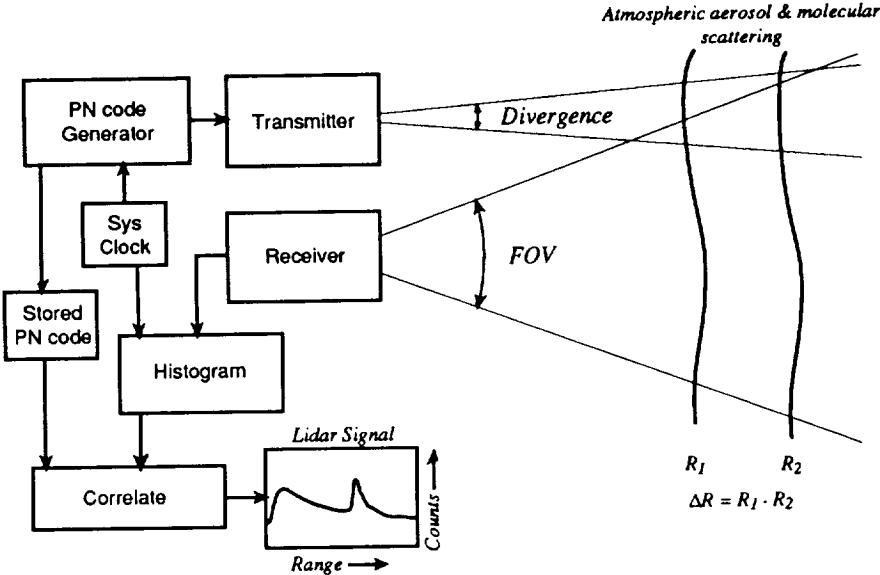


**Figure 5.** Simplified block diagram of PN code lidar system.

## 1.6 PN code lidar background

Several previous lidar systems have used PN code modulation to obtain range resolved signals with low peak power lasers. In 1983, Takeuchi et al. externally modulated an Argon laser, at 514.5 nm, with a PN code to measure the lidar return from a smoke plume at 1 km.[33] In 1986, Takeuchi et al. demonstrated a PN code aerosol lidar using a single 30 mW AlGaAs laser diode transmitter.[34] This system measured lidar returns from falling snow, smoke, nighttime aerosols, and cloud structure. In 1988, Norman and Gardner proposed a PN code technique for performing laser ranging measurements to satellites, and presented a signal and error analysis.[35] In 1992,

Abshire et al. reported nighttime measurements to tree canopies using a PN code modulated AlGaAs laser.[36] With a modified version of this system, Rall et al. reported measuring nighttime aerosol profiles to 4.0 km altitude and cloud returns to 8.6 km altitude.[37] In 1993, Abshire and Rall reported a simplified PN code lidar theory and nighttime measurements to cirrus clouds at 13.5 km and terrestrial targets at 13 km.[38]

Chapter 2 follows with a thorough analysis of PN code lidar theory and operation. In addition, the performance of an AlGaAs water vapor DIAL system is predicted based on the single scattering lidar equation and the system parameters of an existing breadboard lidar.

Chapter 3 reviews water vapor absorption spectroscopy. Criteria for selecting near-ideal absorption lines for water vapor DIAL measurements are developed. Candidate absorption lines are selected and profiled with a laser diode in a multipass absorption cell using derivative spectroscopy. Spectroscopic parameters including linewidth and line center wavelength are measured for the candidate absorption lines. In addition, a technique for actively stabilizing the laser diode frequency to a water vapor absorption line is developed.

Chapter 4 describes two prototype AlGaAs lidar systems that have been assembled and tested. The first system described is a cloud and aerosol lidar and the second is a wavelength stabilized, water vapor DIAL system. System diagrams and instrument characterization are included for each lidar.

Chapter 5 presents lidar data acquired with each system and subsequent data analysis. Lidar measurements over horizontal paths to terrestrial targets are compared with theory using the single scattering lidar equation. Water vapor density is estimated

from DIAL measurements and is compared with ground based humidity measurements made at local airports. Frequency stability of the actively stabilized laser diode is estimated.

Chapter 6 summarizes results of the laser diode frequency stabilization effort, the cloud and aerosol lidar experiments, and the water vapor DIAL measurements. Future work on AlGaAs lidar and altimetry is discussed.

## 2. PHOTON COUNTING AlGaAs LIDAR THEORY

The theory governing the operation of AlGaAs lidar may be developed by considering a laser transmitter which is intensity modulated with a maximal length pseudonoise (PN) code, of length $m$, and the single scattering lidar equation. An expression for the detected lidar signal may be derived by assuming a single reflector or scatterer at a fixed range. This expression may then be generalized by extending it to multiple scatterers at distributed ranges. The lidar, Figure 5, transmits the PN code modulated light into the atmosphere and a fraction of these photons are scattered into the FOV of the lidar receiver and detected. The detected photons produce a sequence of photoelectron emissions which, for a single scatterer, occur in the range bins of the original PN code but lagging the original code by a time delay corresponding to the roundtrip range delay. These photoelectron emissions are accumulated into a histogram and stored in memory. Cross-correlating the histogram with the original PN code yields the atmospheric lidar signal.

### 2.1 PN codes and their properties

PN codes have three noise-like properties which are important to their use in ranging and lidar measurements[39]: (1) The number of ones and zeroes are nearly equal, always one more one than zero. (2) The distribution of ones and zeroes in a sequence is well defined and always the same from one sequence to the next. (3) The normalized autocorrelation function of the sequence yields unity correlation for zero relative delay and near zero correlation for all other values of delay.

A nearly equal number of ones and zeroes allows the transmitting laser to operate with a ~50% duty cycle, with the peak operating power twice the average power. Laser diodes are well suited to operating at such high duty cycles. The distribution of ones and zeroes within a PN code sequence determines its noise-like correlation and spectral properties. Although maximal length PN sequences do repeat (and are deterministic), a sampling of ones and zeroes within the sequence is nearly random and can be made arbitrarily close to random by simply increasing the sequence length. The auto-correlation function of a PN code measures the degree of agreement between a code and a time delayed replica of itself.

A maximal length PN code, $a_i$, has elements $a_i = (0,1)$, where $i = 0, \dots, m-1$. The sequence may be generated by an $n$-stage shift register where the code length $m$ is related to $n$ by

$$m = 2^n - 1.$$ 
(7)

An example of a 7-bit PN code, generated by a three stage shift register, is shown in Figure 6.
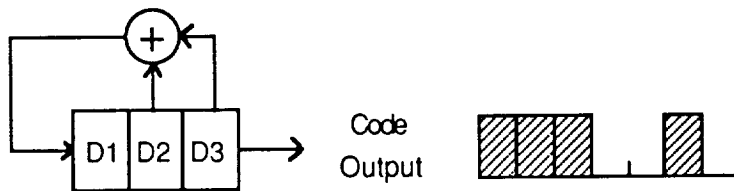


**Figure 6.** Three stage shift register and the 7-bit code it produces when the initial state is the all ones state. The feedback taps are added modulo-2 with an EX-OR gate.

An $m$-bit code sequence has $(m+1)/2$ ones and $(m-1)/2$ zeroes. The $m$-bit code, $a_i$, with elements (0,1) may be expressed alternatively as the code, $a'_i$, with elements (-1, 1) generated by

$$a'_i = 2a_i - 1.$$
(8)

This alternate form of the code is useful in lidar where the amplitude of the correlation function contains information regarding atmospheric backscatter and extinction properties. An example of a 255 bit, amplitude shifted PN code is shown in Figure 7.
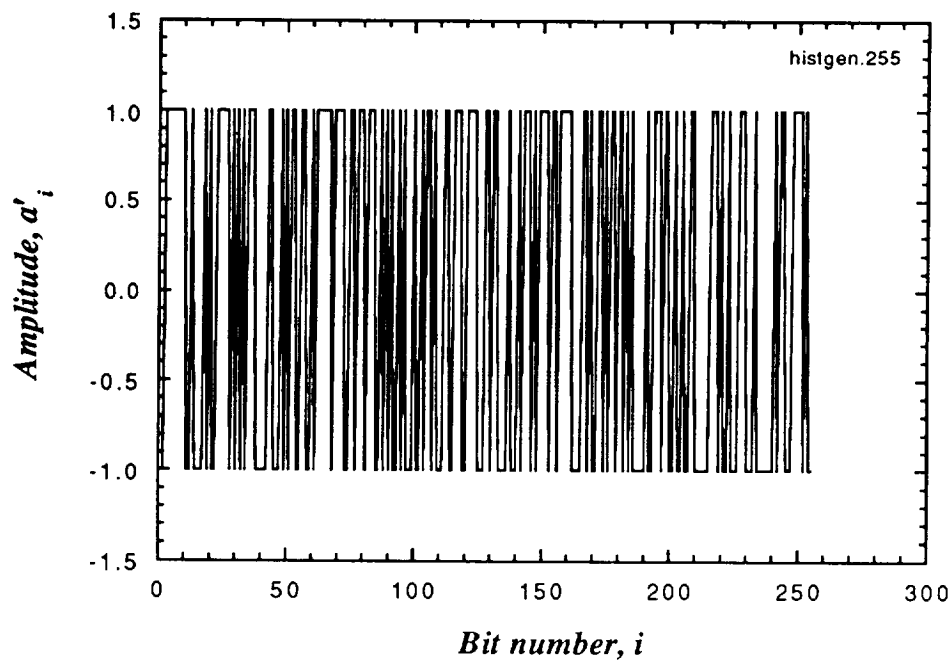


Figure 7. Example of a 255 bit $a'_i$ PN code.

21

### 2.1.1 Autocorrelation & cross-correlation

The autocorrelation function measures the degree of agreement between a code sequence and a time delayed replica of itself. The autocorrelation function, $\phi_{xx}[n]$, of a function, $x[n]$, is defined as[40]

$$\phi_{xx}(n) = \sum_{m=-\infty}^{+\infty} x_{m+n} x_m .$$  (9)

Computing the autocorrelation function for the code, $a_i'$, yields[34]

$$\phi_{a'a'}(j) \equiv \frac{1}{m} \sum_{i=0}^{m-1} a_i' a_{i+j}' = \begin{cases} 1 & j = 0 \\ -1/m & j \neq 0, \end{cases}$$  (10)

where $j$ is modulo-$m$. In PN code lidar, the cross-correlation function is used to compute the lidar signal from the detected backscattered photons. The cross-correlation function, $\phi_{xy}[n]$, of the functions $x[n]$ and $y[n]$ is defined as[40]

$$\phi_{xy}(n) = \sum_{m=-\infty}^{+\infty} x_{m+n} y_m .$$  (11)

It is important to note that the cross-correlation function possesses odd symmetry such that

$$\phi_{xy}[n] = \phi_{yx}[-n] .$$  (12)

22

Computing the cross-correlation function for the code sequences $a_i$ and $a_i'$ yields the correlation function $\phi_{aa'}(j)$ which is shown in Figure 8

$$\phi_{aa'}(j) \equiv \sum_{i=0}^{m-1} a_i a_{i+j}' = \begin{cases} (m+1)/2 & j = 0 \\ 0 & j \neq 0. \end{cases} \tag{13}$$

$\phi_{aa'}(j)$

(m+1)/2

$j$

$j=0$
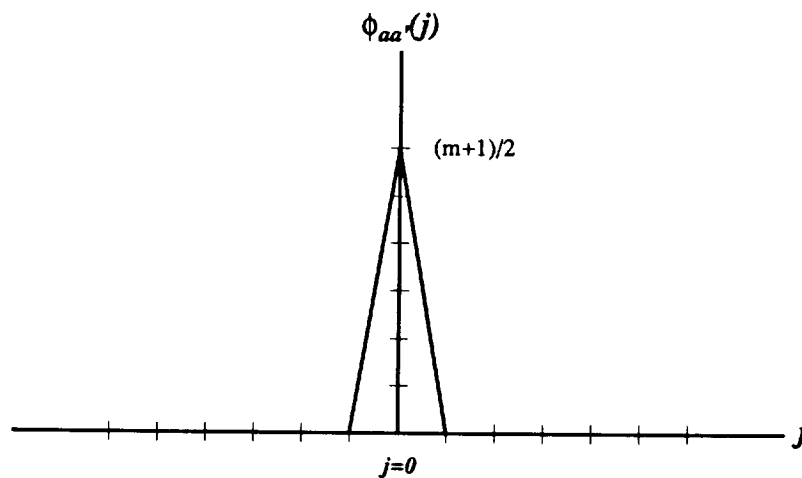
**Figure 8.** The correlation function $\phi_{aa'}(j)$ of a PN sequence of length m.

The peak value of the correlation function occurs at zero time shift to the original code, $j = 0$, and its amplitude is equal to the number of 1's in the code, $(m+1)/2$. For other values of time delay $j$, the correlation function is zero. The cross-correlation function, $\phi_{aa'}(j)$, is more easily visualized in Figure 9 with a 7-bit PN code.

23
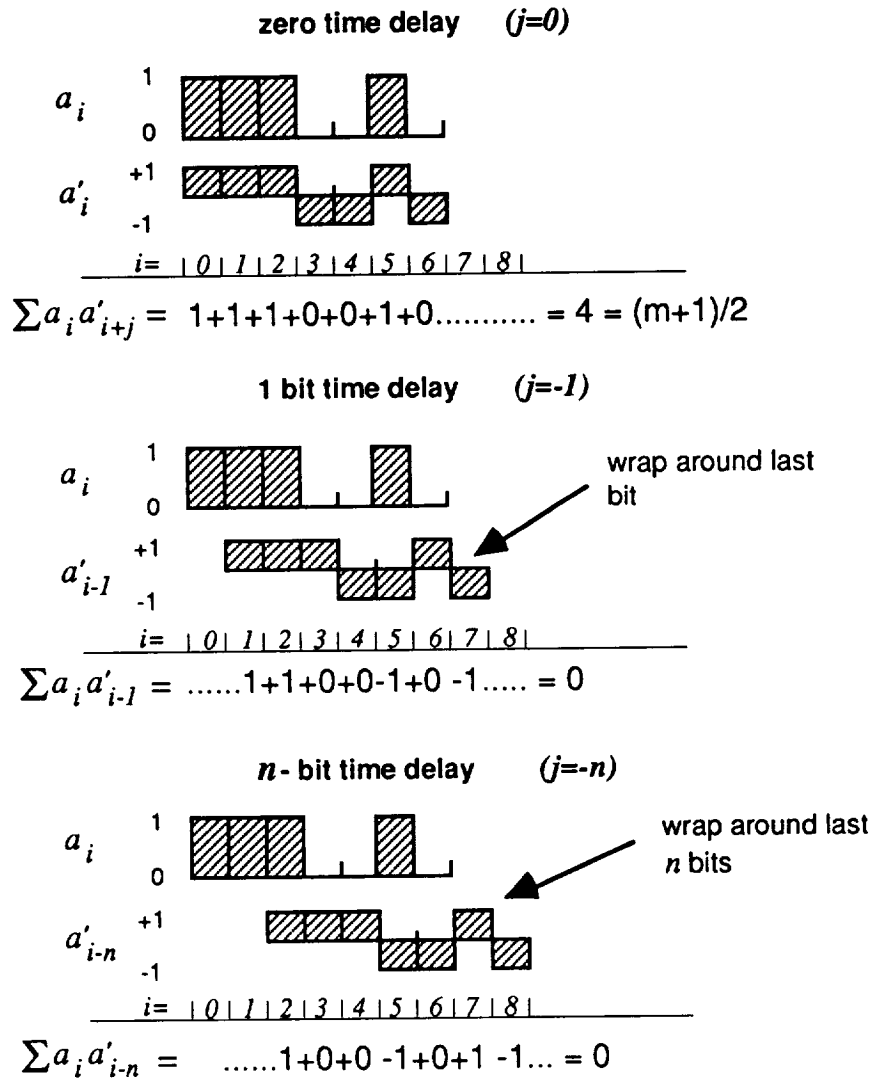
**Figure 9.** Sample cross-correlation function, $\phi_{aa'}(j)$, for a 7-bit PN code. Note that $a_i'$ has been amplitude shifted as in Eq. 8 and that for time delays other than zero, the "extra" $n$ bits of $a_i'$ correlate with the first $n$ bits of $a_i$.

## 2.1.2 Maximum range and range resolution

If the transmitter modulation rate or bit frequency is denoted $f_b$, then the bit period or time duration for each bit is $t_b = 1/f_b$. The lidar system range resolution is

$$\Delta R = (c/2) \cdot t_b,$$

(14)

where the factor of two is due to the roundtrip traveled by the light. The code sequence length $m$ and the bit period $t_b$ determine the maximum unambiguous range which may be measured with an $m$-bit code sequence. The maximum range is given by

$$R_{max} = m \cdot (c/2) \cdot t_b.$$

(15)

Since the sequence repeats identically after $m$-bits, if $R_{max}$ is too small, there can be an ambiguous situation where light is scattered from two ranges, separated by one-half of the code sequence length, $(m \cdot \Delta R)/2$. This constitutes a "wrap-around" of consecutive code sequences and the return (correlation peak) from the more distant target occurs in the same range bin as the closer target. To avoid this, $m$ must be selected which has a maximum unambiguous range, $R_{max}$, greater than the anticipated maximum range.

## 2.2 Expected AlGaAs lidar signal & signal-to-noise ratio

If the laser is operating with an average power, $P_o$, then the transmitted laser power of the $i^{th}$ bit of $a_i$ is

$$p_i = 2P_o \cdot a_i = \begin{cases} 2P_o, & a_i = 1 \\ 0, & a_i = 0 \end{cases}. \tag{16}$$

The expected received power $P$, scattered from range $R_j$, is governed by the single scattering lidar equation and can be written as

$$P(\lambda_L, R_j) = P_o \cdot \frac{A_o}{R_j^2} \cdot \tau_{sys} \cdot \xi(R)\beta_\pi(\lambda_L, R_j)\Delta R \cdot e^{-2\int_0^{R_j} \kappa(\lambda_L, R)dR}, \tag{17}$$

where $P_o$ is the transmitter average laser power, $A_o$ is the effective area of the receiver telescope, $R_j = j \cdot \Delta R$ is the distance to the scatterer, $\tau_{sys}$ is the lidar receiver optical transmission, $\xi(R)$ is the laser divergence and receiver FOV overlap function, $\beta_\pi(\lambda_L, R_j)$ is the atmospheric backscatter coefficient $\left(km^{-1} \cdot sr^{-1}\right)$ at wavelength $\lambda_L$ and range $R_j$, $\Delta R = (c/2) \cdot \tau_b$ is the range cell size, and $\kappa(\lambda_L, R)$ is the total attenuation coefficient $\left(km^{-1}\right)$ due to scattering and absorption by aerosols and molecules. The expected received power may be converted into an expected photoelectron count rate using the energy of the transmitted photons and the quantum efficiency of the detector. The instantaneous photoelectron count rate, $\dot{N}_j$, produced by a photon counting receiver is

$$\dot{N}(\lambda_L, R_j) = p_{i-j} \cdot \frac{\eta}{E_{ph}} \cdot \frac{A_o}{R_j^2} \tau_{sys} \cdot \beta(\lambda_L, R_j) \cdot \Delta R \cdot e^{-2\int_0^{R_j} \kappa(\lambda_L, R)dR}, \tag{18}$$

where $\dot{N}$ denotes the instantaneous photoelectron count rate for range bin $j$, $p_{i-j}$ is the instantaneous transmitted power of the $i^{th}$ bit reflected from the $j^{th}$ range bin, $\eta$ is the

26

quantum efficiency of the detector, $E_{ph} = hc/\lambda_L$ is the laser photon energy, and the overlap function $\xi(R)$ has been assumed to be unity. The expectation value of the photoelectron count rate at the $i^{th}$ bit of the PN code scattered from the $j^{th}$ range cell therefore may be written as

$$\dot{N}_{i,j} = p_{i-j} \cdot \gamma \cdot \frac{\beta(\lambda_L, R_j)}{R_j^2} \cdot \Delta R \cdot e^{-2 \int_0^{R_j} \kappa(\lambda_L, R) dR} , \qquad (19)$$

where

$$\gamma = \frac{\eta \cdot A_o \cdot \tau_{sys}}{hc/\lambda} , \qquad (20)$$

is the combined lidar system parameters. Equation 19 may be simplified by defining

$$G_j = \frac{\beta_\pi(\lambda_L, R_j)}{R_j^2} \cdot \Delta R \cdot e^{-2 \int_0^{R_j} \kappa(\lambda_L, R) dR} , \qquad (21)$$

as an atmospheric scattering and extinction function. The expression for the expected photoelectron count rate from the $j^{th}$ range bin, $\dot{N}_i$, becomes

$$\dot{N}_{i,j} = p_{i-j} \cdot \gamma \cdot G_j . \qquad (22)$$

In addition to the signal photoelectrons, a term for background light must be included. This term, $\dot{b}_i$, is the background photoelectron count rate in the $i^{th}$ bin due to

27

unmodulated laser transmitter light and solar radiation scattered into the FOV of the receiver. This background photoelectron count rate can be expressed as

$$\dot{b}_i = \int_{\Delta\lambda} \frac{S_b(\lambda)}{hc/\lambda} \cdot \tau_{sys} \cdot \Omega_o A_o \cdot \tau_b \, d\lambda, \tag{23}$$

where $S_b(\lambda)$ represents the spectral radiance of the sky background, $\Delta\lambda$ is the spectral width of the receiver's band pass filter, $\tau_{sys}$ is the receiver transmission efficiency, $\Omega_o$ is the receiver acceptance solid angle, $A_o$ is the area of the receiver telescope aperture, and $\tau_b$ is the bit period. The total expected photoelectron count rate in the $i^{th}$ bin due to signal photoelectrons scattered from the $j^{th}$ range cell and background photoelectrons is

$$\dot{N}_{i,j} = p_{i-j} \cdot \gamma \cdot G_j + \dot{b}_i. \tag{24}$$

These photoelectron counts are accumulated into receiver bins synchronously with the transmitted code sequence, creating a histogram of received counts over the integration period. Each receiver bin corresponds to one bit of the PN code sequence. If the signal is accumulated over $L$ cycles of the code sequence, then the receiver integrates for $L \cdot t_b$ seconds at each bin. The total integration time is $T = m \cdot L \cdot t_b$ seconds. The total integrated counts in the $i^{th}$ bin is then

$$N_{i,j} = L \cdot t_b \cdot p_{i-j} \cdot \gamma \cdot G_j + L \cdot t_b \cdot \dot{b}_i. \tag{25}$$

28

This gives the functional form of the lidar return for a single scatterer. The extension to multiple scatterers at distributed ranges is done by summing over all range bins $j$, where $j$ is modulo-$m$ yielding

$$N_i = L \cdot t_b \cdot \gamma \sum_{j=0}^{m-1} p_{i-j} \cdot G_j + L \cdot t_b \cdot \dot{b}_i \ . \tag{26}$$

$N_i$ represents the histogram of received counts in each of $i$ receiver bins due to signal scattering from range cells $j = 0...m-1$ and background counts. The histogram contains information about the atmospheric path or transfer function which transformed the input photons to the received photoelectrons. The lidar signal, $S_n$, may be generated by cross-correlating the histogram, $N_i$, with the modulation code, $a'_i$,

$$S_n = \sum_{i=0}^{m-1} N_i a'_{i-n} = L \cdot t_b \cdot \gamma \left\{ \sum_{i=0}^{m-1} \sum_{j=0}^{m-1} p_{i-j} G_j a'_{i-n} + \sum_{i=0}^{m-1} \dot{b}_i a'_{i-n} \right\}, \tag{27}$$

where $n$ is modulo-$m$ and the property of odd symmetry Eq (12) has been used. Substituting $p_{i-j} = 2P_o \cdot a_{i-j}$ yields

$$S_n = 2P_o L \cdot t_b \cdot \gamma \sum_{i=0}^{m-1} \sum_{j=0}^{m-1} a_{i-j} G_j a'_{i-n} + L \cdot t_b \cdot \sum_{i=0}^{m-1} \dot{b}_i a'_{i-n} \ . \tag{28}$$

Exchanging the order of summation,

$$S_n = 2P_o L \cdot t_b \cdot \gamma \sum_{j=0}^{m-1}\sum_{i=0}^{m-1} a_{i-j} G_j a'_{i-n} + L \cdot t_b \cdot \sum_{i=0}^{m-1} \dot{b}_i a'_{i-n} , \qquad (29)$$

and using the properties of PN code cross-correlation[41] from Equation 13

$$\phi_{aa'}(j-n) \equiv \sum_{i=0}^{m-1} a_{i-j} a'_{i-n} = \begin{cases} (m+1)/2 & n = j \\ 0 & n \neq j \end{cases} , \qquad (30)$$

yields,

$$S_n = 2P_o L \cdot t_b \cdot \gamma \sum_{j=0}^{m-1} \phi_{aa'}(j-n) G_j + \overline{b} . \qquad (31)$$

The background count rate, $\dot{b}_i$, has been assumed independent of the modulation code $a'_i$ and therefore replaced with a time averaged background count, $\overline{b} = L \cdot t_b \cdot \dot{b}_i$ which can be dealt with independently of the signal photoelectrons. The cross-correlation is non zero for $n = j$ only, yielding the lidar signal

$$S_n = P_o L \cdot t_b \cdot \gamma (m+1) G_n . \qquad (32)$$

Equation 32 represents the lidar signal (without integrated background counts) as a function of range bin index $n$ which is identical to range index $j$ used earlier. The response function or atmospheric response may be derived by solving this equation for $G_n$ once $S_n$ has been calculated from the histogrammed data.

Due to the nature of light detection, the photoelectron counts in the received histogram $N_i$ Eq. (26) have a Poisson distribution. The probability function of the Poisson distribution is

$$P_p(x,\mu) \equiv \frac{\mu^x}{x!} e^{-\mu},\tag{33}$$

The average count $\bar{x}$ is an estimate of the mean, $\mu$, of the Poisson distribution. The mean is found by calculating the expectation value of $x$

$$\langle x \rangle = \sum_{x=0}^{\infty}\left(x \cdot \frac{\mu^x}{x!} e^{-\mu}\right) = \mu e^{-\mu} \cdot \sum_{x=0}^{\infty}\frac{\mu^{x-1}}{(x-1)!} = \mu e^{-\mu} \sum_{y=0}^{\infty}\frac{\mu^y}{y!} = \mu \tag{34}$$

where the last summation in Eq (34) is the series expansion of the exponential

$$\sum_{y=0}^{\infty}\frac{\mu^y}{y!} = e^{\mu}.\tag{35}$$

The counts in each bin of the histogram Eq (26) have a Poisson distribution. The photoelectron counts fluctuate from observation to observation simply because random samples of events distributed randomly in time contain numbers of events which fluctuate from sample to sample.[42] For Poisson distributions, the mean equals the variance and the standard deviation is the square root of the variance. To compute the lidar signal for each range bin, Eq (29) sums the counts from each histogram bin over the entire received sequence. Therefore the variance of each lidar signal range bin (correlation space) is the sum of the variances of each histogram bin (histogram space)

31

which is the sum of all signal and background counts accumulated. Consequently, all range bins of the lidar signal $S_n$ Eq (32) have the same variance given by

$$\text{var}(S_n) = \sigma_{s_n}^2 = \sum_{i=0}^{m-1} N_i .$$

(36)

The signal-to-noise ratio (SNR) of the lidar signal in any range bin $n$ is the signal count in that range bin (minus the average background count) divided by the standard deviation, $\sigma$,

$$SNR(n) = \frac{S_n}{\sqrt{\text{var}(S_n)}} = \frac{P_o L \cdot t_b \cdot \gamma(m+1)G_n}{\sqrt{\sum_{i=0}^{m-1} N_i}} .$$

(37)

## 2.3 Performance calculations

The expected performance of a single-color AlGaAs lidar is estimated using the single scattering lidar equation Eq. (18). These performance estimates are used to predict the performance of a differential absorption water vapor AlGaAs lidar. The lidar system parameters used were based on the existing prototype AlGaAs lidar and are listed in Table 1. The atmospheric conditions, including backscatter coefficient and total extinction coefficient, were adapted from the 1962 U.S. Standard Atmosphere and the AFGL MidLatitude-Summer model. The total extinction coefficient, $\kappa(\lambda_L, R)$, can be expressed as the sum

$$\kappa(\lambda_L, R) = k_m + \sigma_m + k_a + \sigma_a ,$$

(38)

where $k_m$ is the water vapor absorption coefficient, $\sigma_m$ is the molecular scattering coefficient, $k_a$ is the aerosol absorption coefficient, and $\sigma_a$ is the aerosol scattering coefficient. Values for the individual attenuation coefficients have been adapted from the AFGL MidLatitude-Summer model based on the U.S. Standard Atmosphere (USSA) 1962 and are catalogued as functions of wavelength, altitude, latitude, and season.[26] The individual attenuation coefficient values for 0.86 μm are listed in Table 2 as a function of altitude.

**Table 1**

AlGaAs lidar prototype system parameters.

| | |
|---|---|
| Laser power | 35 mW Average |
| Laser wavelength | 810 nm |
| Photon energy @ 810 nm | 2.44E-19 J/photon |
| Transmitter divergence | 100 μrad |
| Telescope Area (20 cm diam./8 cm obscur.) | 0.026 m$^2$ |
| Telescope Field of view (FOV) | 160 μrad |
| Detector detection probability | 0.25 PE/photon @ 830 nm |

**Table 2**

Calculated off-line values for individual attenuation coefficients at 0.86 μm as a function of altitude, latitude, and season.

| Height $(km)$ | Molecular (H2O) | | Aerosol (clear) | |
|---|---|---|---|---|
| | $k_m\left(km^{-1}\right)$ | $\sigma_m\left(km^{-1}\right)$ | $k_a\left(km^{-1}\right)$ | $\sigma_a\left(km^{-1}\right)$ |
| 0 | < 10E-6 | 1.93E-3 | 1.52E-2 | 9.03E-2 |
| 1 | < 10E-6 | 1.84E-3 | 1.01E-2 | 5.99E-2 |
| 2 | < 10E-6 | 1.66E-3 | 4.41E-3 | 2.61E-2 |
| 5 | < 10E-6 | 1.22E-3 | 5.58E-4 | 3.30E-3 |
| 10 | < 10E-6 | 7.11E-4 | 3.10E-4 | 1.83E-3 |

Note: Values for attenuation coefficients are for Midlatitude Summer conditions

The original USSA 1962 did not contain a water vapor distribution which was added later.[43] The water vapor number density used to calculate the water vapor attenuation coefficient[26] is listed in Table 3.

**Table 3**

Atmospheric water vapor density vertical profile.

| Height (km) | Pressure (mbar) | Temperature (K) | Water vapor (g/m$^3$) | Number density (molecules/cm$^3$) |
|---|---|---|---|---|
| 0 | 1013 | 294 | 14.0 | 4.60e17 |
| 1 | 902 | 290 | 9.3 | 3.10e17 |
| 2 | 802 | 285 | 5.9 | 1.96e17 |
| 5 | 554 | 267 | 1.0 | 3.33e16 |
| 10 | 281 | 235 | 0.064 | 2.13e15 |

The on-line water vapor attenuation coefficient $k_m$ is calculated for an absorption line at 811.617 nm, adjusted for pressure and is listed in Table 4.

**Table 4**

Atmospheric water vapor attenuation coefficient $k_m$ vs altitude.

| Height (km) | $k_m$ (km$^{-1}$) |
|---|---|
| 0 | 0.44 |
| 1 | 0.33 |
| 2 | 0.24 |
| 5 | 0.059 |
| 10 | 0.007 |

The received photoelectron count rate was calculated for single color horizontal path lidar measurements at altitudes of sea-level, 1, 2, 5, and 10 km and one-way path lengths of 1, 2, 5, and 10 km. Estimated values for the volume backscattering coefficient[44] and the off-line total attenuation coefficient are listed in Table 5. When

34

the laser is wavelength tuned to the center of an absorption line, the molecular absorption term, $k_m$, dominates the total attenuation coefficient, $\kappa(\lambda_L, R)$. However, the other attenuation coefficients may not be neglected. As an example, the absorption line at 811.617 nm was used to estimate photoelectron count rates for horizontal path DIAL measurements made at the center of the absorption line. The line strength for this line is $2.54 \times 10^{-24}$ $cm^{-1}/molecule \cdot cm^{-2}$ which makes it a moderately strong absorption line in the 820 nm band. The total on-line attenuation coefficient was calculated using the water vapor absorption coefficients listed in Table 4 and are listed in the last column of Table 5.

### Table 5

Backscatter coefficient $\beta_\pi$ and total attenuation coefficients $\kappa_{off}$ & $\kappa_{on}$ vs altitude.

| $alt(km)$ | $\beta_\pi\left(m^{-1} \cdot sr^{-1}\right)$ | $\kappa_{off}\left(km^{-1}\right)$ | $\kappa_{on}\left(km^{-1}\right)$ |
|---|---|---|---|
| 0 | 2E-6 | 0.1074 | 0.547 |
| 1 | 4E-7 | 0.0718 | 0.401 |
| 2 | 2E-7 | 0.0321 | 0.272 |
| 5 | 1E-7 | 0.0050 | 0.064 |
| 10 | 6E-8 | 0.0028 | 0.010 |

The estimated off-line photoelectron count rates vs altitude and horizontal range are listed in Table 6. These estimated photoelectron count rates are applicable as the off-line DIAL measurement of tropospheric water vapor. The estimated photoelectron count rates vs altitude and horizontal range for the on-line channel are listed in Table 7.

## Table 6

Expected off-line photoelectron count rates for various length horizontal path aerosol lidar measurements vs altitudes.

| Off-line | Horizontal Range (km) | | | |
|---|---|---|---|---|
| Altitude (km) | 1 | 2 | 5 | 10 |
| 0 | 1.12E+05 | 2.26E+04 | 1.90E+03 | 1.62E+02 |
| 1 | 2.41E+04 | 5.22E+03 | 5.43E+02 | 6.62E+01 |
| 2 | 1.31E+04 | 3.06E+03 | 4.04E+02 | 7.31E+01 |
| 5 | 6.89E+03 | 1.71E+03 | 2.65E+02 | 6.29E+01 |
| 10 | 4.15E+03 | 1.03E+03 | 1.62E+02 | 3.94E+01 |

## Table 7

Expected on-line photoelectron count rates for 811.617 nm water vapor absorption line for various length horizontal path lidar measurements vs altitude.

| On-line | Horizontal Range (km) | | | |
|---|---|---|---|---|
| Altitude (km) | 1 | 2 | 5 | 10 |
| 0 | 4.52E+04 | 3.66E+03 | 2.00E+01 | 1.80E-02 |
| 1 | 1.22E+04 | 1.34E+03 | 1.82E+01 | 7.40E-02 |
| 2 | 8.03E+03 | 1.16E+03 | 3.57E+01 | 5.71E-01 |
| 5 | 6.12E+03 | 1.34E+03 | 1.46E+02 | 1.91E+01 |
| 10 | 4.09E+03 | 1.00E+03 | 1.51E+02 | 3.39E+01 |

An estimate of the relative measurement error inherent to the AlGaAs DIAL technique can be derived by looking at the statistical fluctuations of the photoelectron count about the mean. Taking a ratio of the expressions for $N_{on}$ and $N_{off}$, Equations (3) and (5), we find

$$\frac{N_{on}}{N_{off}} = \exp\left\{-2\int_0^R k_m(R)dR\right\},\qquad (39)$$

where the contents within the brackets is the optical thickness due to attenuation by water vapor absorption. Rearranging this equation yields a relation between water vapor absorption and the on and off line photoelectron counts

$$\int_0^R k_m(R)dR = -\tfrac{1}{2}\ln\left[\frac{N_{on}}{N_{off}}\right].$$
(40)

The statistics of the water vapor absorption integral depend upon the statistics of the ratio of $N_{on}/N_{off}$. We can describe these fluctuations for $N_{on}$ and $N_{off}$ as

$$N_{on} = \langle N_{on}\rangle\cdot\left(1+\frac{\Delta N_{on}}{\langle N_{on}\rangle}\right)$$
(41)

and

$$N_{off} = \langle N_{off}\rangle\cdot\left(1+\frac{\Delta N_{off}}{\langle N_{off}\rangle}\right).$$
(42)

The equations may be simplified by defining the fluctuating part as

$$\varepsilon_{on} = \frac{\Delta N_{on}}{\langle N_{on}\rangle}$$
(43)

and

$$\varepsilon_{off} = \frac{\Delta N_{off}}{\langle N_{off}\rangle},$$
(44)

respectively. Since $\varepsilon_{on}$ and $\varepsilon_{off}$ fluctuate symmetrically about the mean, $\langle\varepsilon_{on}\rangle = \langle\varepsilon_{off}\rangle = 0$. For large values of $N$,

37

$$\frac{\Delta N}{\langle N \rangle} \ll 1 \Leftrightarrow \varepsilon \ll 1. \tag{45}$$

Therefore the variance of the fluctuating part, $\varepsilon$, is

$$\text{var}(\varepsilon) \cong \frac{1}{N} \tag{46}$$

and the standard deviation is

$$\sigma(\varepsilon) \cong \frac{1}{\sqrt{N}} \tag{47}$$

Forming the ratio

$$\frac{N_{on}}{N_{off}} = \frac{\langle N_{on} \rangle \cdot (1 + \varepsilon_{on})}{\langle N_{off} \rangle \cdot (1 + \varepsilon_{off})} \tag{48}$$

and simplifying,

$$\frac{N_{on}}{N_{off}} = \frac{\langle N_{on} \rangle \cdot (1 + \varepsilon_{on})}{\langle N_{off} \rangle \cdot (1 + \varepsilon_{off})} \cdot \frac{(1 - \varepsilon_{off})}{(1 - \varepsilon_{off})}, \tag{49}$$

yields an expression for $N_{on}/N_{off}$

$$\frac{N_{on}}{N_{off}} = \frac{\langle N_{on} \rangle \cdot (1 + \varepsilon_{on} - \varepsilon_{off} - \varepsilon_{on}\varepsilon_{off})}{\langle N_{off} \rangle \cdot (1 + \varepsilon^2_{off})}. \tag{50}$$

Since $\varepsilon_{on}$ and $\varepsilon_{off} \ll 1$, the cross product and square terms may be ignored leaving

$$\frac{N_{on}}{N_{off}} = \frac{\langle N_{on} \rangle}{\langle N_{off} \rangle}\left(1 + \varepsilon_{on} - \varepsilon_{off}\right).$$

(51)

The mean value $\langle N_{on}/N_{off} \rangle$ may be formed yielding

$$\left\langle \frac{N_{on}}{N_{off}} \right\rangle = \frac{\langle N_{on} \rangle}{\langle N_{off} \rangle}\left(1 + \langle \varepsilon_{on} \rangle - \langle \varepsilon_{off} \rangle\right) = \frac{\langle N_{on} \rangle}{\langle N_{off} \rangle},$$

(52)

because $\langle \varepsilon_{on} \rangle = \langle \varepsilon_{off} \rangle = 0$. The variance of $\langle N_{on}/N_{off} \rangle$ is the square of the expectation value $\langle N_{on}/N_{off} \rangle$ multiplied by the sum of the variances of $N_{on}$ and $N_{off}$,

$$\mathrm{var}\left(\frac{N_{on}}{N_{off}}\right) = \left(\frac{\langle N_{on} \rangle}{\langle N_{off} \rangle}\right)^2 \left(\mathrm{var}(\varepsilon_{on}) + \mathrm{var}(\varepsilon_{off})\right).$$

(53)

Substituting expressions for variances from Equation 46 yields,

$$\mathrm{var}\left(\frac{N_{on}}{N_{off}}\right) = \left(\frac{\langle N_{on} \rangle}{\langle N_{off} \rangle}\right)^2 \left(\frac{1}{N_{on}} + \frac{1}{N_{off}}\right).$$

(54)

The standard deviation is the square root of the variance,

$$\sigma\left(\frac{N_{on}}{N_{off}}\right) = \frac{\langle N_{on} \rangle}{\langle N_{off} \rangle}\sqrt{\frac{1}{\langle N_{on} \rangle} + \frac{1}{\langle N_{off} \rangle}}$$

(55)

and the relative error in the ratio $N_{on}/N_{off}$ is defined as the standard deviation divided by the mean,

39

$$\frac{\sigma}{\mu} = \frac{\frac{\langle N_{on} \rangle}{\langle N_{off} \rangle} \sqrt{\frac{1}{\langle N_{on} \rangle} + \frac{1}{\langle N_{off} \rangle}}}{\frac{\langle N_{on} \rangle}{\langle N_{off} \rangle}} , \tag{56}$$

which yields

$$\frac{\sigma}{\mu} = \sqrt{\frac{1}{\langle N_{on} \rangle} + \frac{1}{\langle N_{off} \rangle}} . \tag{57}$$

For ease of plotting, assign $f = N_{on}/N_{off}$, where $f$ represents the water vapor absorption, then the expression for relative error becomes

$$rel.\ error = \frac{1}{\sqrt{N_{off}}} \sqrt{1 + \frac{1}{f}} . \tag{58}$$

This expression for relative error of $N_{on}/N_{off}$ vs. $N_{off}$, the off-line photoelectron count rate, is plotted in Figure 10 for $0.1 \leq f \leq 1.0$. Figure 10 indicates that for DIAL measurements with less than 10% relative measurement error and off-line photo-electron count rate greater than 1000 counts/sec the fractional absorption $f$ must not be less than 0.1. That is, greater absorption of the on-line channel by water vapor will lead to a larger relative error. However, the figure is misleading. It suggests that weaker absorption lines, which will yield less fractional absorption, will also yield a smaller relative error.
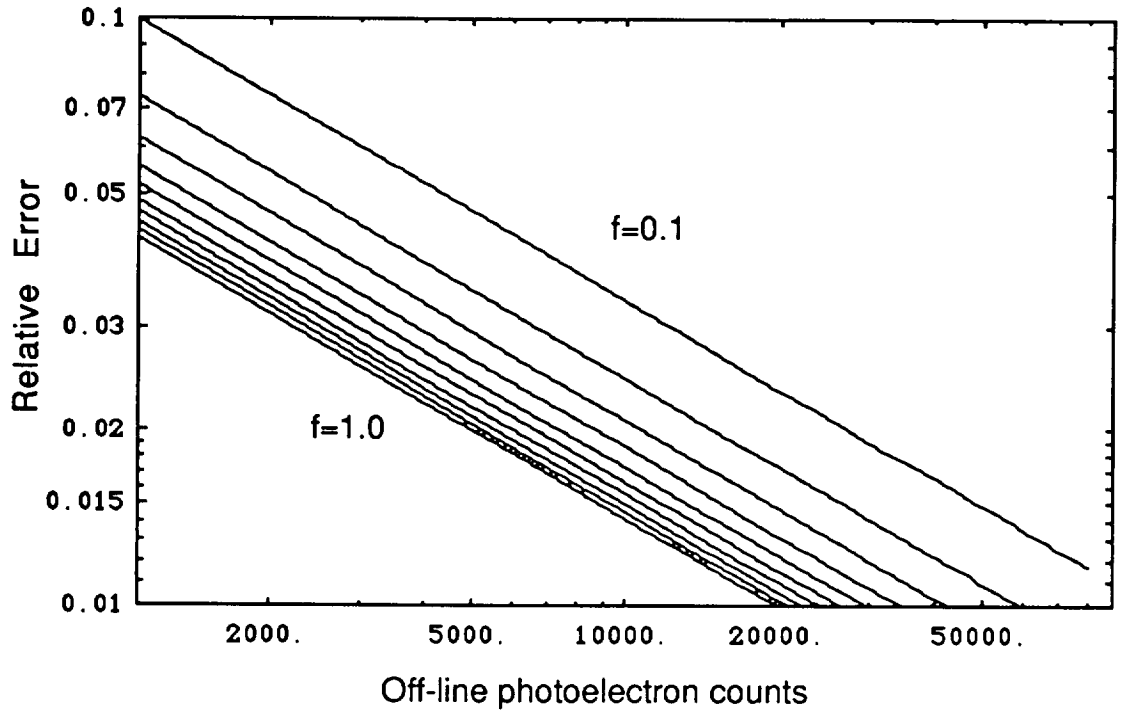
**Figure 10.** Plot of relative error of $N_{on}/N_{off}$ vs. $N_{off}$ for $0.1 \leq f \leq 1.0$.

But as the fractional absorption approaches 1,

$$\lim_{f \Rightarrow 1} \ln\left(\frac{N_{on}}{N_{off}}\right) \Rightarrow 0 .$$

(59)

A more important error to be determined is the relative error in the estimate of the water vapor number density, $n(\Delta R)$. The functional form for this error may be derived by using Eq (6), the DIAL equation, and the expression for the standard deviation of the ratio $N_{on}/N_{off}$, Eq. (55). The DIAL equation is

$$n(\Delta R) \cong \frac{1}{2\Delta\sigma\Delta R} \ln\left[\frac{N_{on}(R_1)N_{off}(R_2)}{N_{on}(R_2)N_{off}(R_1)}\right] .$$

(60)

41

The desired expression is the relative error of $n(\Delta R)$. Eq (60) has the form:

$$n(\Delta R) \cong C \ln[x] .$$

(61)

where C is a constant including the prefactors in Eq (60), and $x = u \cdot v$. Here $u = N_{on}(R_1)/N_{off}(R_1)$, and $v = N_{off}(R_2)/N_{on}(R_2)$. The quantities u and v are assumed independent of each other. The relative error of $n(\Delta R)$ may be expressed as

$$\sigma_n = \sigma_x \frac{dn}{dx}$$

(62)

where

$$\frac{\sigma_x^2}{x^2} = \frac{\sigma_u^2}{u^2} + \frac{\sigma_v^2}{v^2}$$

(63)

and

$$\frac{dn}{dx} = C \cdot \frac{d}{dx} \ln(x) = C \cdot \frac{1}{x} .$$

(64)

Substituting the expressions $x = u \cdot v$, Eq (63) & (64) into Eq (62) yields the expression for the standard deviation of $n(\Delta R)$

$$\sigma_n = C \cdot \sqrt{\frac{1}{N_{on}(1)} + \frac{1}{N_{off}(1)} + \frac{1}{N_{on}(2)} + \frac{1}{N_{off}(2)}} .$$

(65)

The relative error is formed by taking the ratio of Eq (65) with Eq (60), the expression for $n(\Delta R)$ yielding

4 2

$$\frac{\sigma_n}{n} = \frac{\sqrt{\dfrac{1}{N_{on}(1)} + \dfrac{1}{N_{off}(1)} + \dfrac{1}{N_{on}(2)} + \dfrac{1}{N_{off}(2)}}}{\ln\left[\dfrac{N_{on}(1)}{N_{off}(1)}\right] - \ln\left[\dfrac{N_{off}(2)}{N_{on}(2)}\right]}$$

(66)

This expression may be simplified using the properties of the natural logarithm function yielding

$$\frac{\sigma_n}{n} = \frac{\sqrt{\dfrac{1}{N_{on}(1)} + \dfrac{1}{N_{off}(1)} + \dfrac{1}{N_{on}(2)} + \dfrac{1}{N_{off}(2)}}}{\ln\left[\dfrac{N_{on}(1)}{N_{off}(1)}\right] + \ln\left[\dfrac{N_{on}(2)}{N_{off}(2)}\right]} \; .$$

(67)

For small range bin sizes, $N_{on}(1) \approx N_{on}(2)$ and $N_{off}(1) \approx N_{off}(2)$ and Eq (67) becomes

$$\frac{\sigma_n}{n} = \frac{\sqrt{\dfrac{2}{N_{off}}}\sqrt{1 + \dfrac{1}{f}}}{2 \ln f} \; ,$$

(68)

where $f = N_{on}/N_{off}$, the fractional absorption due to water vapor. The expression in Eq (68) is plotted in Figure 11. As the absorption due to water vapor decreases, i.e. $f \Rightarrow 1$ the relative error blows up and Eq (68) reduces to

$$\frac{\sigma_n}{n} = \frac{1}{\sqrt{N_{off}} \ln(1)} \Rightarrow \infty \; .$$

(69)

43

Conversely, as the absorption due to water vapor increases, $f \Rightarrow 0$, Eq (68) becomes indeterminate. Both the numerator and denominator of Eq (68) approach infinity. Applying L'Hopital's rule to Eq (68) and simplifying yields

$$\frac{\sigma_n}{n} = \frac{-1}{\sqrt{f^2 + f}} \tag{70}$$

which blows up to infinity as $f \Rightarrow 0$.
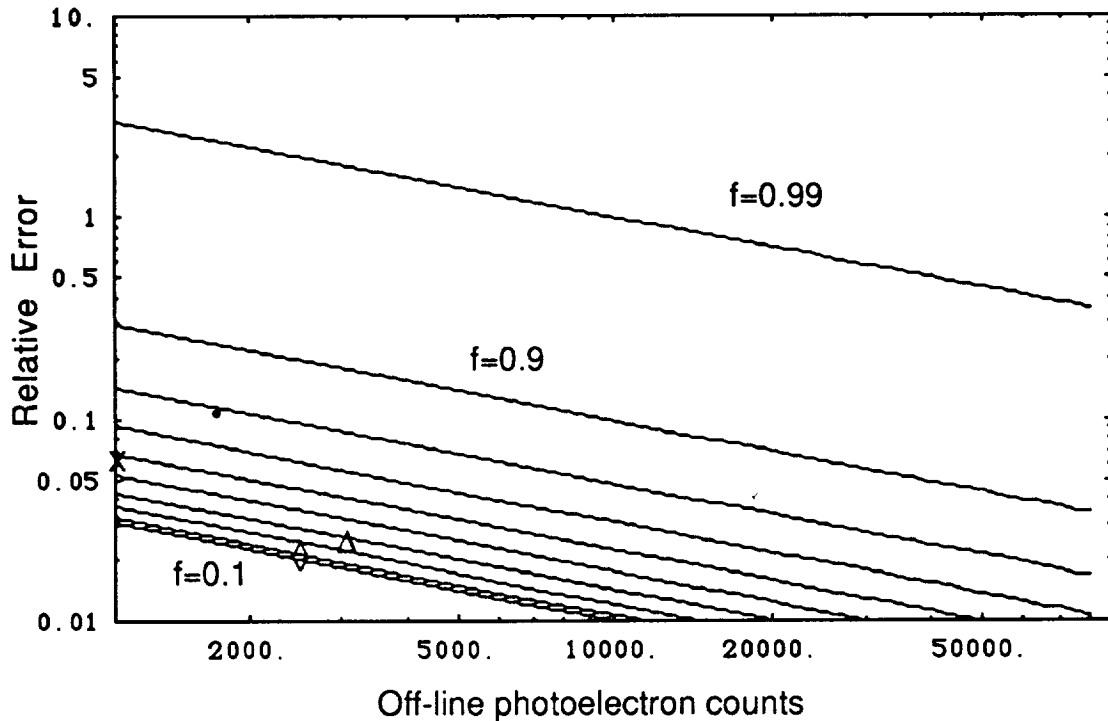


**Figure 11.** Relative error of water vapor number density estimate as a function of off-line photoelectron counts and fractional absorption due to water vapor, $f = N_{on}/N_{off}$.

Also plotted in Figure 11 are four data points from the estimated performance of the prototype AlGaAs lidar system. The on-line and off-line photoelectron count rates,

44

Tables 6 & 7, are based on system parameters listed in Table 1 and the 811.617 nm absorption line. The "X" indicates the expected lidar performance at 5 km altitude and 5 km horizontal range; the "•" marks the lidar performance at 5 km altitude and 2 km horizontal range; the "Δ" indicates lidar performance at 2 km altitude and 2 km horizontal range; and the "◊" marks the expected lidar performance at sea-level and 2 km horizontal range. The 811.617 nm line is too strong to make low altitude (≤2 km) DIAL measurements of water vapor over horizontal ranges greater than 2 km. However, the line is too weak to make short path DIAL measurements above 2 km altitude, where water vapor density is lower and $f \Rightarrow 1$. Also, at higher altitudes where the backscatter coefficient is much weaker, the average laser power is too low to make long range (≥5 km) DIAL measurements. For a water vapor DIAL lidar to be accurate (minimal relative error) and have a practical range of up to several kilometers, Figure 11 indicates that a more powerful laser transmitter (higher $N_{off}$) and both weak and strong absorption lines are required. However, too strong of an absorption line will completely attenuate the on-line signal and the relative error will blow up as in Eq (70). In conclusion, for a given laser power, several water vapor lines with a wide range of absorption strengths must be selected to accommodate varying atmospheric conditions, *i.e.* changes in humidity and backscatter coefficient, in order to make accurate DIAL measurements of atmospheric water vapor over a practical range of ~1- 10 km.

The next chapter reviews water vapor absorption spectroscopy. Candidate absorption lines are selected for DIAL experiments. Linewidth and line center wavelength are measured for these candidate absorption lines. Frequency stability requirements are determined for the water vapor DIAL laser transmitter and a stabilization technique is developed and tested.

## 3. H₂0 VAPOR SPECTROSCOPY, ABSORPTION LINE PROFILING, AND LINE LOCKING EXPERIMENTS

Remote sensing of atmospheric water vapor using the DIAL technique requires selecting water vapor absorption lines which have absorption cross sections appropriate for the water vapor density and measurement range of interest. For vertical path DIAL measurements lines should be insensitive to variations in temperature and pressure over the measurement range. Further, criteria must be established for selecting absorption lines, taking into consideration not only temperature sensitivity and line strength but pressure shift effects, broadening effects, and interference due to neighboring lines. Once established, these criteria may be used to select specific water vapor lines appropriate for DIAL measurements of tropospheric water vapor.

The DIAL method employs the difference in the water vapor absorption cross section between $\lambda_{on}$ and $\lambda_{off}$ to estimate water vapor number density in the atmospheric path. The absorption cross section Eq.(1) is a function of line strength, $S$, and linewidth, $\gamma$, both of which are functions of pressure and temperature. Therefore, the temperature and pressure characteristics of $S(T)$ and $\gamma(p,T)$ must be examined before selecting absorption lines for DIAL measurements. The three water vapor absorption bands in the near infrared, Figure 1, centered at 720, 820, and 940 nm, originate in the vibrational ground state with different vibrational overtones as their upper states. The weak to moderate line strengths typical of the 720 and 820 nm bands are best suited to DIAL measurements in the wetter troposphere while stronger lines near 940 nm are better suited for the dryer tropopause and stratosphere. Commercial,

high power AlGaAs lasers are most readily available from 780 to 860 nm, therefore the

820 nm band is best suited to DIAL measurements of tropospheric water vapor using

AlGaAs lasers. It should be noted that the expressions for water vapor line strength and

line shape in the 820 nm band are identical to those in the 720 and 940 nm bands.

Water vapor absorption linewidths are broadened in the atmosphere by two

processes, pressure broadening and Doppler broadening, which are represented by the

Lorentz lineshape and the Doppler or Gaussian lineshape, respectively. Variations in

absorption line shapes due to pressure are not critical since the spectral linewidth of

AlGaAs lasers (1-10 MHz) is two to three orders of magnitude narrower than typical

water vapor absorption linewidths (1-5 GHz). Any uncertainties due to pressure shift

of line center can be minimized by stabilizing the laser wavelength to the center

frequency of the absorption line at a lower pressure, i.e. higher altitude.[45] Therefore,

pressure shift and broadening effects are not dealt with in this work.

### 3.1 Absorption lineshape, line strength, and cross section

The shape of a water vapor absorption line can be represented by a Lorentz line

shape when atmospheric pressure broadening dominates, i.e. altitudes $\leq$ 15 km.[45] The

absorption coefficient for a Lorentz line shape is

$$k_m(v) = n\sigma_a = n \cdot \frac{S}{\pi} \cdot \frac{\gamma/2}{(v - v_o)^2 + (\gamma/2)^2} , \qquad (71)$$

where $n$ is the number density of water molecules $(molec / cm^3)$, $\sigma_a$ is the absorption

cross section $(cm^2 / molec)$, $\gamma$ is the Lorentz linewidth $(cm^{-1})$, $v_o$ is the frequency at

47

line center $\left(cm^{-1}\right)$, and $S$ is the line strength with units of $cm^{-1}/\left(molecules \cdot cm^{-2}\right)$. Figure 12 shows a plot of the Lorentz line shape using the linewidth and center frequency of a water vapor absorption line at 811.617 nm.
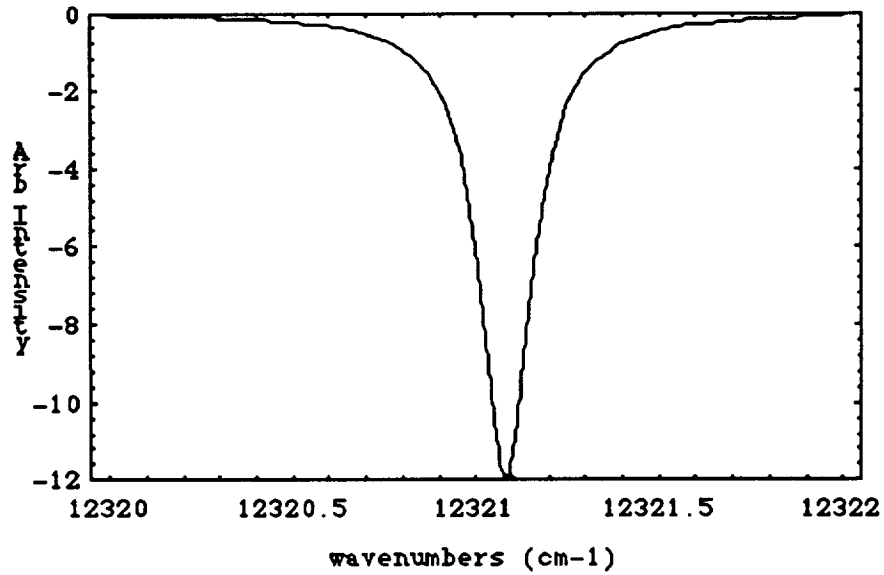


**Figure 12.** Plot of Lorentz lineshape for water vapor absorption line at 811.617 nm with half-width, $\gamma = 0.0837cm^{-1} / atm$.

The pressure and temperature dependence of the Lorentz linewidth, $\gamma(p,T)$, is given by[46]

$$\gamma = \gamma_o \cdot \left(\frac{P}{P_o}\right) \cdot \left(\frac{T_o}{T}\right)^{\alpha}, \qquad (72)$$

where $p$ is pressure, $T$ is temperature, the subscript "$o$" denotes initial or STP values, and $\alpha$ is the linewidth temperature dependent parameter. Measured values of

$\alpha$, for lines in the 720 nm band, vary widely, from 0.28 to 0.88 with 0.62 the value most often used.[47] At line center, the absorption coefficient, $k_m(v)$, reduces to

$$k_o = n \cdot \frac{S_o}{\pi \cdot \gamma_o},$$

(73)

which is the absorption cross section, $\sigma$, multiplied by the number density, $n$. The line strength is related to the dipole moment of the water vapor molecule by[48]

$$S_o = \frac{e^2 f_o \pi}{2 m_e \varepsilon_o c},$$

(74)

where the oscillator strength, $f_o$, of a dipole transition is[49]

$$f_o = \frac{4 \pi m_e v_{fi}}{3 e^2 \hbar} \cdot |\mu_{fi}|^2,$$

(75)

and $v_{fi}$ is the frequency of the transition, $e$ is the charge of the electron, $m_e$ is the electron mass, and $\mu_{fi}$ is the transition dipole moment. The temperature dependence of the absorption line strength, $S$, for a triatomic molecule, e.g. water, is given by[50]

$$S(T) = S(T_o) \cdot \frac{Q_v(T_o) Q_r(T_o)}{Q_v(T) Q_r(T)} \cdot \exp\left[\frac{E'' hc}{k} \cdot \left(\frac{T - T_o}{T \cdot T_o}\right)\right],$$

(76)

where $Q_v$ is the vibrational partition function, $Q_r$ is the rotational partition function, $E''$ is the ground state energy, $h$ is Planck's constant, and $k$ is Boltzmann's constant. For the water molecule, the vibrational partition function varies negligibly from unity over the temperature range 175-325K and the temperature dependence of the rotational partition function is given by[51]

$$\left(\frac{T_o}{T}\right)^{j}, \tag{77}$$

where $j = 3/2$ . The expression for the temperature-dependent line strength reduces to

$$S(T) = S(T_o) \cdot \left(\frac{T_o}{T}\right)^{3/2} \cdot \exp\left[\frac{E'' hc}{k} \cdot \left(\frac{1}{T_o} - \frac{1}{T}\right)\right]. \tag{78}$$

Given the temperature dependencies of the line strength and linewidth, the temperature sensitivity of the absorption cross section, at line center, may be calculated.

### 3.2 Temperature sensitivity of 820 nm water vapor absorption lines

The temperature sensitivity of water vapor absorption cross section at 820 nm is calculated using the same procedure as was previously done for the 720 and 940 nm water vapor bands.[46,52] Substituting the temperature dependent expressions for line strength Eq (78) and linewidth Eq (72) into the expression for absorption cross section, Eq (1), yields

50

$$\sigma_o = \frac{S(T_o)\left(\frac{T_o}{T}\right)^{\frac{3}{2}} \cdot \exp\left[\frac{E''hc}{k} \cdot \left(\frac{1}{T_o} - \frac{1}{T}\right)\right]}{\pi \cdot \gamma_o \cdot \left(\frac{P}{P_o}\right) \cdot \left(\frac{T_o}{T}\right)^{\alpha}}. \qquad (79)$$

After simplifying the expression and consolidating terms in the denominator with like terms in the numerator, the absorption cross section at line center is written as

$$\sigma_o = \frac{1}{\pi} \frac{S_o}{\gamma_o} \left(\frac{P_o}{P}\right) \cdot \left(\frac{T_o}{T}\right)^{\left(\frac{3}{2} - \alpha\right)} \cdot \exp\left[\frac{E''hc}{k} \cdot \left(\frac{1}{T_o} - \frac{1}{T}\right)\right]. \qquad (80)$$

Taking the derivative of $\sigma_o$ with respect to temperature once yields the change in absorption cross section at line center as a function of temperature, which is written as

$$\frac{d\sigma_o}{dT} = \frac{1}{\pi} \frac{S_o}{\gamma_o} \left(\frac{P_o}{P}\right) \cdot \frac{d}{dt}\left\{\left(\frac{T}{T_o}\right)^{\left(\alpha - \frac{3}{2}\right)} \cdot \exp\left[\frac{E''hc}{k} \cdot \left(\frac{1}{T_o} - T^{-1}\right)\right]\right\}, \qquad (81)$$

where the expression within the braces has the form $c_1 f_1(t) \cdot \exp(c_2 \cdot f_2(t))$. Applying the product rule for differentiation and simplifying the result yields

$$\frac{d\sigma_o}{dT} = \frac{1}{\pi} \frac{S_o}{\gamma_o} \left(\frac{P_o}{P}\right) \cdot \exp\left[\frac{E''hc}{k} \cdot \left(\frac{1}{T_o} - \frac{1}{T}\right)\right] \cdot \left(\frac{T}{T_o}\right)^{\left(\alpha - \frac{3}{2}\right)} \left\{\frac{\left(\alpha - \frac{3}{2}\right)}{T} + \frac{E''hc}{kT^2}\right\}. \qquad (82)$$

Recognizing that the expression on the right hand side of Equation (82), excluding the curly braces, is equivalent to the expression for absorption cross section, $\sigma_o$, as in Eq. (80), then the expression simplifies to,

$$\frac{d\sigma_o}{dT} = \frac{\sigma_o}{T} \cdot \left\{ \left( \alpha - \tfrac{3}{2} \right) + \frac{E''hc}{kT} \right\}. \tag{83}$$

Setting this expression equal to zero yields

$$\frac{d\sigma_o}{dT} = 0 = \frac{\sigma_o}{T} \cdot \left\{ \left( \alpha - \tfrac{3}{2} \right) + \frac{E''hc}{kT} \right\}. \tag{84}$$

Since $\sigma_o$ does not equal zero within an absorption line, the term in the braces on the right hand side of Eq. (84) must equal zero for the expression to hold,

$$\left( \alpha - \tfrac{3}{2} \right) + \frac{E''hc}{kT} = 0. \tag{85}$$

Solving this equation for temperature yields an expression for the temperature neutral points of a given absorption line as a function of the ground state energy level, $E''$ , and the linewidth temperature dependent parameter, $\alpha$,

$$T_n = \frac{E''hc}{k\left( \alpha - \tfrac{3}{2} \right)}. \tag{86}$$

Equation (83) may be plotted for given values of $\alpha$ and $E''$. Dividing $d\sigma_o/dT$ by $\sigma_o$

and plotting the result as a function of temperature yields the fractional change in cross

section due to changes in temperature. Figures 13, 14, and 15 show temperature

sensitivity of absorption cross section, for Lorentz profile lines, as a function of $E''$

for $\alpha$ =0.62, 0.88, & 0.28 respectively. These values of $\alpha$ reflect the most often used,

0.62, and the measured extremes, 0.88 and 0.28. Therefore Figure 13 may be used in

general to select temperature insensitive absorption lines while Figures 14 and 15 may

be taken as the upper and lower bounds.
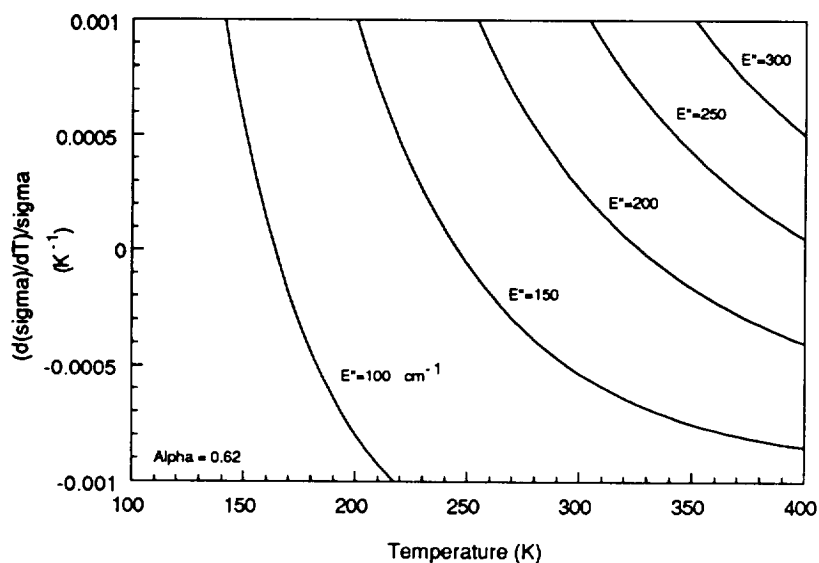


**Figure 13.** The change in absorption cross section, $\sigma_o$ = sigma, as a function of temperature, ground state energy level, $E''(cm^{-1})$, and temperature dependent linewidth parameter, $\alpha = 0.62$.
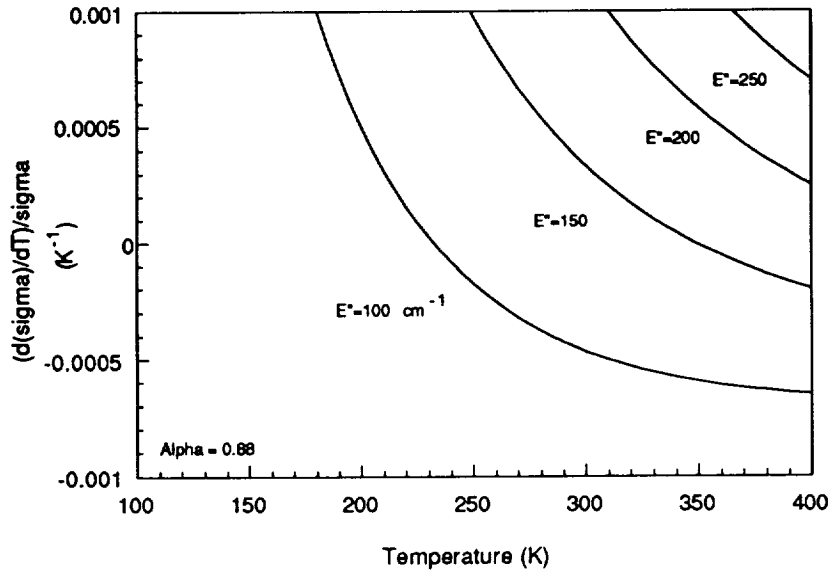
**Figure 14.** The change in absorption cross section, $\sigma_o$ = sigma, as a function of temperature, ground state energy level, $E''(cm^{-1})$, and temperature dependent linewidth parameter, $\alpha = 0.88$.

The temperature neutral points defined in equation (86) are the zero crossings of each $E''$ curve in the figures. For mid-latitude, spring/summer conditions the Earth's troposphere ranges in temperature from 288 K, at the surface, down to 210 K, at the tropopause. By selecting water vapor absorption lines with $E'' = 100 - 250\ cm^{-1}$, the error in absorption cross section due to temperature variation may be limited to less than ±0.1%. In addition to temperature sensitivity, selection criteria must take into consideration the absorption line strength and separation from neighboring lines.
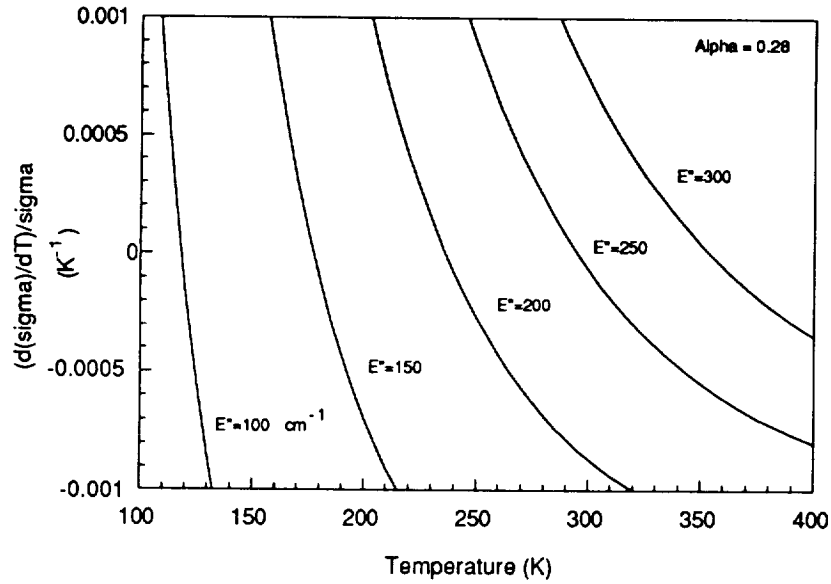
**Figure 15.** The change in absorption cross section, $\sigma_o =$ sigma, as a function of temperature, ground state energy level, $E''(cm^{-1})$, and temperature dependent linewidth parameter, $\alpha = 0.28$.

### 3.3 Absorption line strength and optical thickness

Optical thickness or optical depth is a concept used to define attenuation of a beam propagating through a medium. In our case, the medium is an atmospheric path containing water vapor. The path length, $x$, and volume extinction coefficient, $\beta_{ex}$, which includes scattering and absorption due to both molecules and particles, determines the one-way optical thickness, $T_{ex}$, which is defined as

$$T_{ex} = \int_0^x \beta_{ex}(x)dx. \tag{87}$$

55

This is the general expression for the optical thickness, applicable to both homogenous paths and paths with variable extinction. A one way optical thickness with a value near unity is considered near optimal for making DIAL measurements of water vapor.[53] Since extinction coefficient and path length determine optical thickness, any practical DIAL system will require operation at several different wavelengths in order to access absorption lines of varying strength in order to maintain an optical thickness near unity over the expected measurement range and water vapor density. The volume extinction coefficient $\beta_{ex}$ is used interchangeably with $\kappa(\lambda, R)$ the total extinction coefficient, Eq. (38). When the laser is tuned to the center of an absorption line, the total extinction coefficient, $\kappa(\lambda, R)$, is dominated by the water vapor absorption coefficient, $k_m$. However, the other attenuation coefficients may not be neglected. For a homogenous path, the integral in Eq. (87) reduces to a product, and the optical thickness, as a function of absorption line parameters, may be written by substituting Eq. (73) into Eq. (87) for $\beta_{ex}$ yielding

$$T_{ex} = \left( \frac{n \cdot S_o}{\pi \cdot \gamma_L} + \sigma_m + k_a + \sigma_a \right) \cdot x, \tag{88}$$

where $n$ is the density of water molecules along the path of length $x$. This permits calculation of optical thickness for various measurement ranges and selected water vapor absorption lines. Using the molar mass of the water molecule, 18.0152 grams/mole, the mass of a single water molecule is found by dividing the molar mass by Avogadro's number, yielding

$$Mass(H_2O) = \frac{18.01}{6.025 \times 10^{23}} \cong 3.00 \times 10^{-23} (grams / molecule). \tag{89}$$

56

The mean density of water vapor at sea level for mid latitude summer conditions[54] is ~14.0 g/m³ which corresponds to a water vapor number density of

$$n_{H_2O} = [H_2O] = \frac{14.0g/m^3}{3.00 \times 10^{-23}g/molec} = 4.6 \times 10^{17} molecules/cm^3.$$  (90)

Using this number density, the optical thickness for several candidate absorption lines, is presented in Table 8 as function of measurement range (horizontal path at sea-level).

**Table 8**

Calculated optical thickness vs measurement range for selected absorption lines.

| Wavenumber | Wavelength | Line Strength | Linewidth | Optical Thickness @ Range | | | |
|---|---|---|---|---|---|---|---|
| cm-1 | nm | cm-1/mol cm-2 | cm-1*atm | 1 km | 2 km | 5 km | 10 km |
| 12254.533 | 816.024 | 1.51E-23 | 0.0829 | 2.70 | 5.40 | 13.51 | 27.02 |
| 12259.498 | 815.694 | 4.01E-24 | 0.0579 | 1.02 | 2.05 | 5.13 | 10.27 |
| 12259.572 | 815.689 | 1.20E-23 | 0.0583 | 3.05 | 6.10 | 15.26 | 30.53 |
| 12261.018 | 815.593 | 6.28E-24 | 0.0904 | 1.03 | 2.06 | 5.15 | 10.30 |
| 12349.352 | 809.759 | 2.07E-25 | 0.0937 | 0.03 | 0.07 | 0.16 | 0.33 |
| 12356.828 | 809.269 | 4.42E-25 | 0.0869 | 0.08 | 0.15 | 0.38 | 0.75 |
| 12359.925 | 809.066 | 1.26E-25 | 0.0923 | 0.02 | 0.04 | 0.10 | 0.20 |
| 12365.038 | 808.732 | 4.50E-25 | 0.0972 | 0.07 | 0.14 | 0.34 | 0.69 |
| 12375.118 | 808.073 | 1.88E-25 | 0.0879 | 0.03 | 0.06 | 0.16 | 0.32 |

3.4  DIAL absorption line selection criteria

To reduce errors in the DIAL measurements due to interference from neighboring lines, individual absorption lines should be resolved from neighboring lines by 10 - 20 pm, or 1-2 absorption linewidths.  The following selection criteria have been applied to a listing of water vapor absorption lines from the HITRAN database.

1) Single lines separated by $0.2\, cm^{-1}$ or ~10 pm from neighboring lines

57

2) Lower level energies of $E'' = 100 - 250 \ cm^{-1}$

3) Line strengths of $10^{-25} - 10^{-23} \ cm^{-1}/ molecule \cdot cm^{-2}$

Based on the optical thickness calculations in Table 8, temperature sensitivity, and wavelength separation, the lines most attractive in the 820 nm band for DIAL measurements of atmospheric water vapor are listed in Table 9.

## Table 9

Water vapor absorption lines which meet selection criteria for DIAL measurements.

| Effective Range | Wavelength (nm) | Line Strength $(\times 10^{-23})$ | Lower State Energy $E''$ $(cm^{-1})$ |
|---|---|---|---|
| Short Range ($\leq 2$ km) | 816.024 | 1.51 | 300 |
| | 815.694 | 1.20 | 447 |
| | 815.593 | 0.63 | 275 |
| Long Range ($\geq 2$ km) | 810.861 | 0.017 | 142 |
| | 811.464 | 0.045 | 173 |
| | 808.732 | 0.094 | 136 |

### 3.5 Absorption line profiling experiments

An experimental setup has been built using a multipass absorption cell and an AlGaAs laser to detect and profile selected water vapor absorption lines near 820 nm. This line profile data is used to estimate water vapor absorption linewidth and line center wavelength. Figure 16 shows a block diagram of the experimental set-up. A temperature and current controlled AlGaAs laser is used to profile the absorption lines. The laser is used with a chopper wheel, to modulate the light, and lockin amplifier in a phase sensitive detection scheme. The wavelength is monitored with a vacuum wavemeter, Burleigh WA-20, which yields an absolute accuracy of $\pm 1$ part in $10^6$ providing that the laser linewidth is $\lesssim 2$ GHz. This corresponds to better than 1 pm accuracy at 820 nm but is limited by the instrument readout precision of 1 pm. Once

lines have been profiled, the chopper wheel is replaced with a current dither in order to perform the derivative spectroscopy measurements. The dither current modulates the frequency of the laser, which, when scanned through an absorption line, can be demodulated to generate the first, second, or third derivative of the absorption line with respect to current.
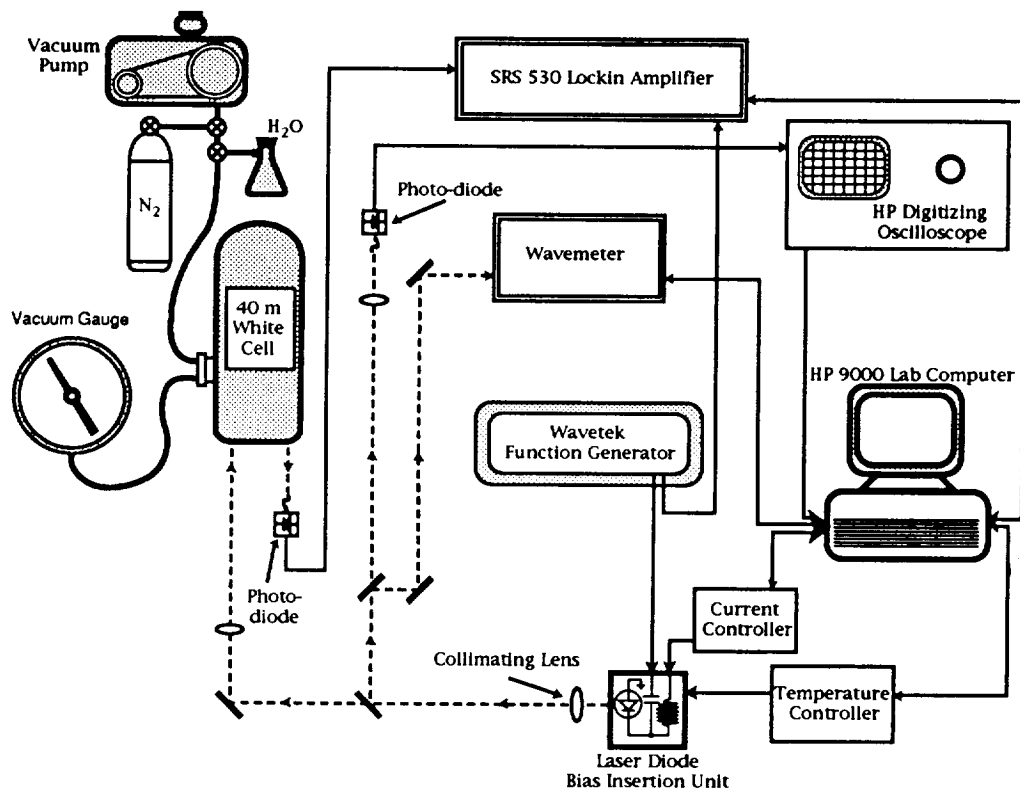


**Figure 16.** Block diagram of water vapor absorption line profiling experiment.

### 3.5.1 AlGaAs laser diode characterization for line profiling

The laser diode used to profile absorption lines was a Mitsubishi ML 5412N 30 mW device. The laser was fully characterized before it was mounted in the test set up. This characterization included measuring the optical output power vs bias current at

different case temperatures ( $T_c$ ), characterizing the emission spectra with an optical spectrum analyzer, and measuring the emission wavelength vs. bias current as a function of temperature. Figures 17-20 show PI curves for Mitsubishi device 87-17003, taken at $T_c$=15, 20, 25, and 30°C, respectively. This device, was used to probe water vapor lines near 816 nm. The slope efficiency, $\eta$, of the device is estimated to be 0.62 mW/mA with a threshold current, $I_{th}$, of approximately 42 mA at $T_c$=15°C. As $T_c$ is increased to 20°C, $I_{th}$ increases and $\eta$ decreases to 0.61 mW/mA. The typical slope of $I_{th}$ vs $T_c$ is 0.66 mA/°C and $\eta$ vs. $T_c$ is -0.0014 mW/mA per °C
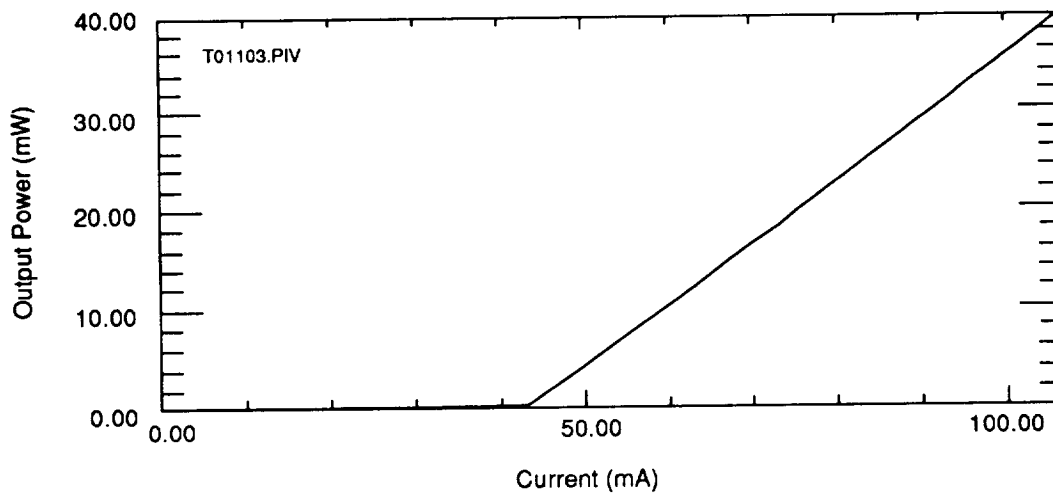


**Figure 17.** PI curve for Mitsubishi ML5412N laser diode (serial #87-17003) operating at $T_c$=15°C.
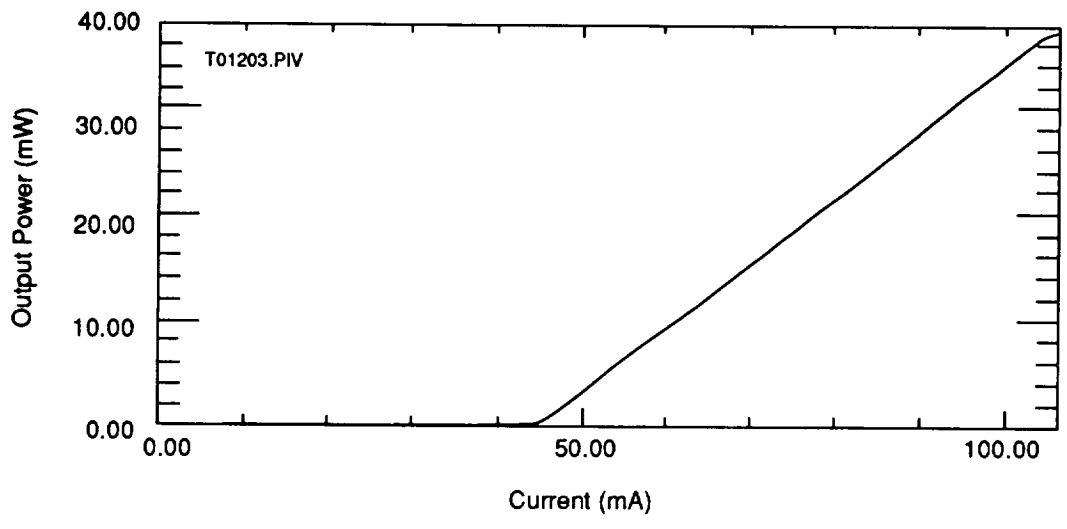
**Figure 18.** PI curve for Mitsubishi ML5412N laser diode (serial #87-17003) operating at $T_c$=20°C.
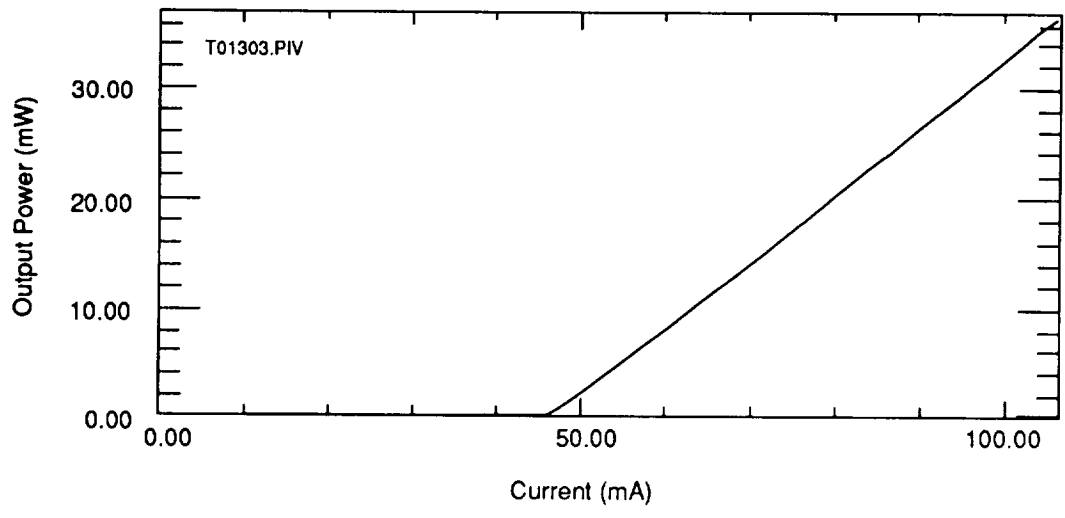


**Figure 19.** PI curve for Mitsubishi ML5412N laser diode (serial #87-17003) operating at $T_c$=25°C.
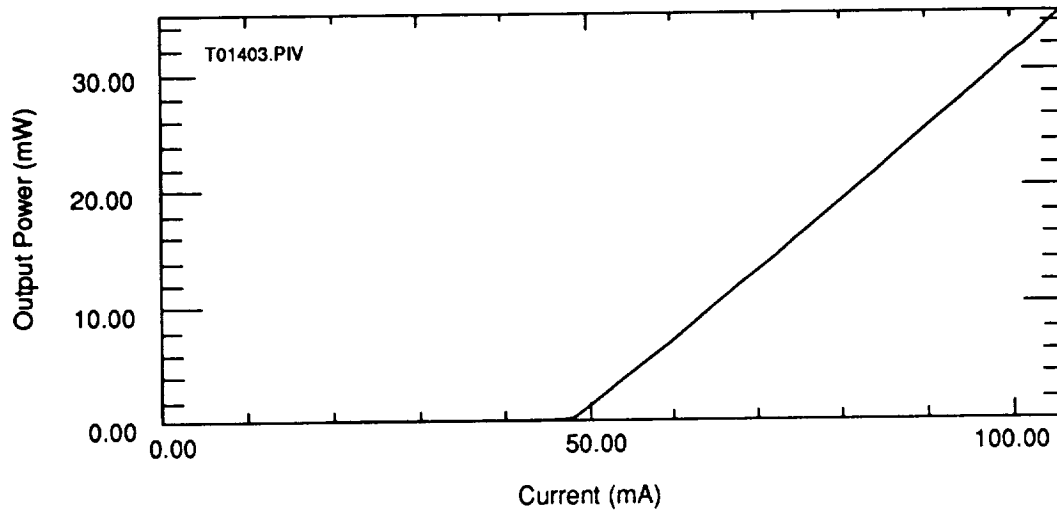
**Figure 20.** PI curve for Mitsubishi ML5412N laser diode (serial #87-17003) operating at $T_c$=30°C.

The emission spectra of device 87-17003 is shown in Figure 21 for different temperatures. These spectra were taken with the laser diode operating at 97 mA bias current using a grating optical spectrum analyzer with 0.1 nm resolution. The laser operated single longitudinal mode at each temperature. Laser wavelength increased with temperature. The -3 dB points on these spectral curves match the instrument resolution implying that the laser linewidth is ≤ 0.1 nm.
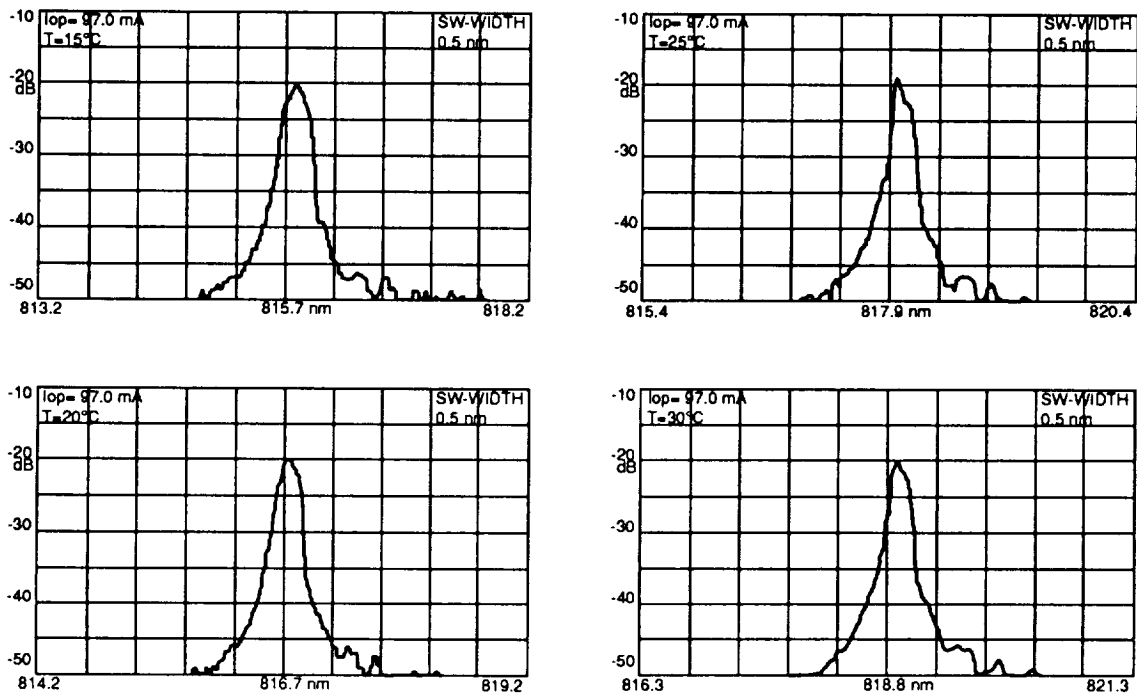
**Figure 21.** Emission spectra of Mitsubishi ML5412N laser diode (serial #87-17003) operating at $I_{op}$=97.0 mA and $T_c$ =15, 20, 25, and 30°C.

The wavelength of an AlGaAs laser is tunable with bias current. Figure 22 shows the current tuning characteristics for different temperatures. This data was taken with the grating spectrum analyzer to measure the peak emission wavelength and to ensure single mode operation at each temperature. The data for each curve was taken only with increasing bias current to avoid hysteresis inherent in AlGaAs laser wavelength tuning. The figure also shows the maximum temperature tuning range of this device to be approximately 4.0 nm with the laser operating at its 30 mW rated power level.
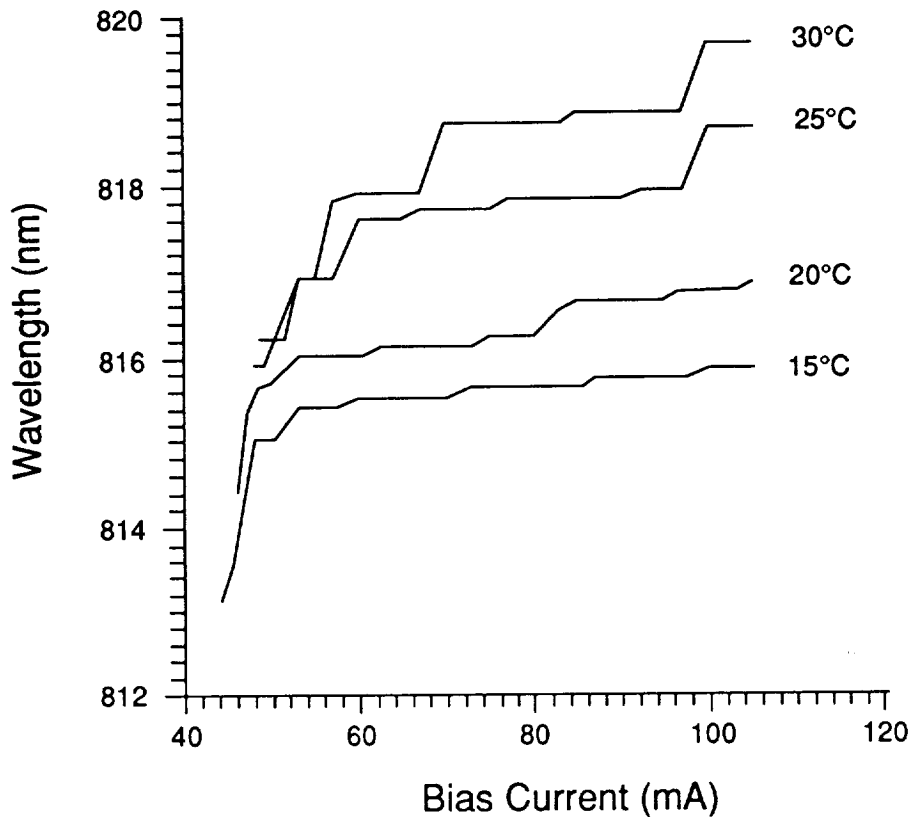
**Figure 22.** Wavelength dependence on bias current for Mitsubishi ML5412N laser diode (serial #87-17003) operating at $T_c = 15$, 20, 25, and 30°C.

### 3.5.2 Profiling water vapor lines

Profiling water vapor lines and estimating their linewidths and line center

wavelengths were done by scanning the wavelength of the laser through a known water

vapor absorption line while detecting a signal transmitted through the White cell with a

photodiode. The White cell was evacuated and backfilled with pure water to a vapor

pressure of ~20 Torr. The temperature of the White cell was not controlled but assumed

constant throughout each measurement. The absorption line profiles were observed by

modulating the light at ~4 kHz with a chopper wheel and detecting the chopped signal,

through the White cell, with a photodiode and a Stanford Research Systems SRS 530

lockin amplifier.  The lockin amplifier acts as a tunable, narrowband filter useful for

sensing weak signals in the presence of noise.  The experimental set-up was controlled

by a Hewlett-Packard computer which also acted as the data acquisition system.  The

computer recorded the laser diode bias current, lockin error voltage, and wavelength.

The temperature of the laser diode was sensed initially by an integrated circuit

temperature sensor (AD-590) which fed a proportional-integral temperature

controller which controlled the current to a thermoelectric cooler.  The temperature

control loop held the temperature stable to better than 0.1°C.  The AD-590 was later

replaced by a 10 k$\Omega$ thermistor which improved the temperature sensing resolution to

0.02°C.

The laser diode bias current was manually adjusted to its preset starting current

before each scan.  This was necessary to coax the laser into the correct longitudinal mode

for the desired water vapor line.  Once in the right laser mode, the lockin amplifier

parameters, including sensitivity, dynamic reserve, phase, and time constant, were

manually set.  The bias current was then scanned, under computer control, through the

water vapor absorption line in 50 or 100 $\mu A$ steps.  At each current step, the computer

recorded the lockin amplifier error voltage and wavelength.  Figure 23 shows the

absorption signal for a weak water vapor absorption line centered at 815.769 nm.
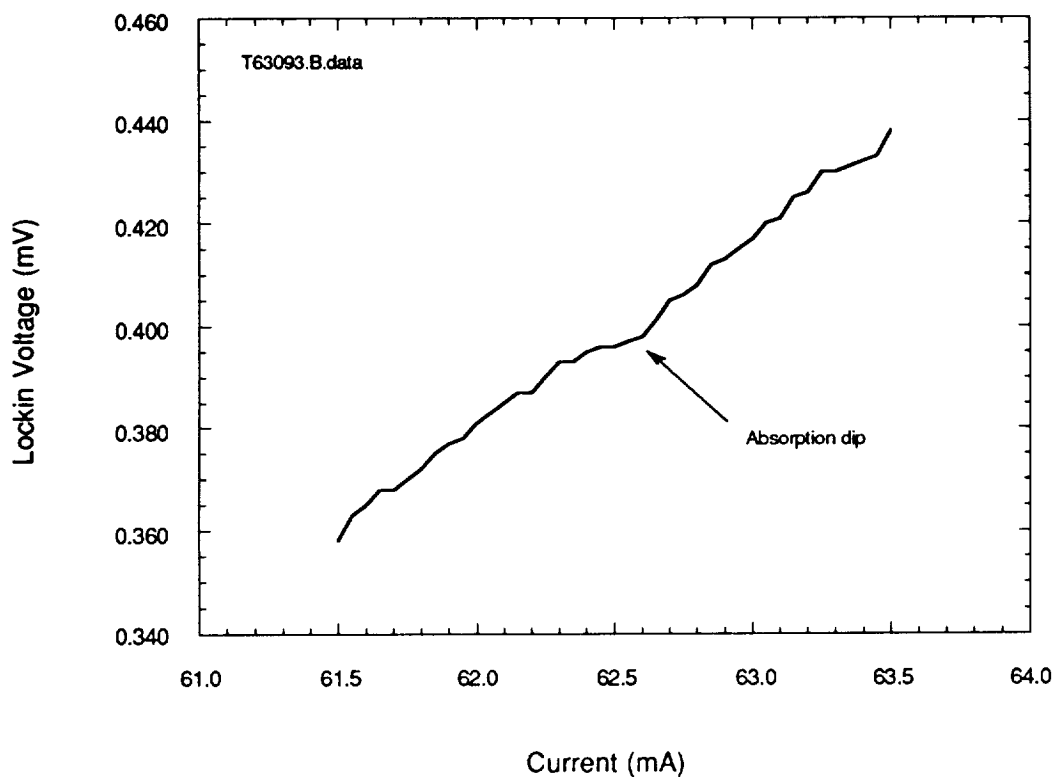
**Figure 23.** Weak absorption feature centered at 815.769 nm.

The vacuum wavelength of this line, recorded in the HITRAN database, is 815.772 nm and absorption line strength is $2.83 \times 10^{-26} cm^{-1}/molecule \cdot cm^{-2}$. The discrepancy in observed wavelength may be attributed to either a vacuum error in the wavemeter, which would tend to shorten the wavelength due to an increase in refractive index inside the interferometer, or the pressure shift effect of line center due to the partial pressure of water vapor in the White cell. This data was taken with an absorption cell path length of ~ 20 m, vapor pressure $\leq$ 20 Torr, and laser diode temperature of 19°C. The expected absorption for this line strength, vapor density, and path length is $\leq$0.01%.

66

A stronger absorption line was scanned and is shown in Figure 24. The vacuum wavelength of this line is 816.024 nm. The observed wavelength however was 816.027 nm. The absorption strength for this line is $1.51 \times 10^{-23}\ cm^{-1}/molecule \cdot cm^{-2}$. The expected absorption for this line strength, vapor density, and path length is ~5%.
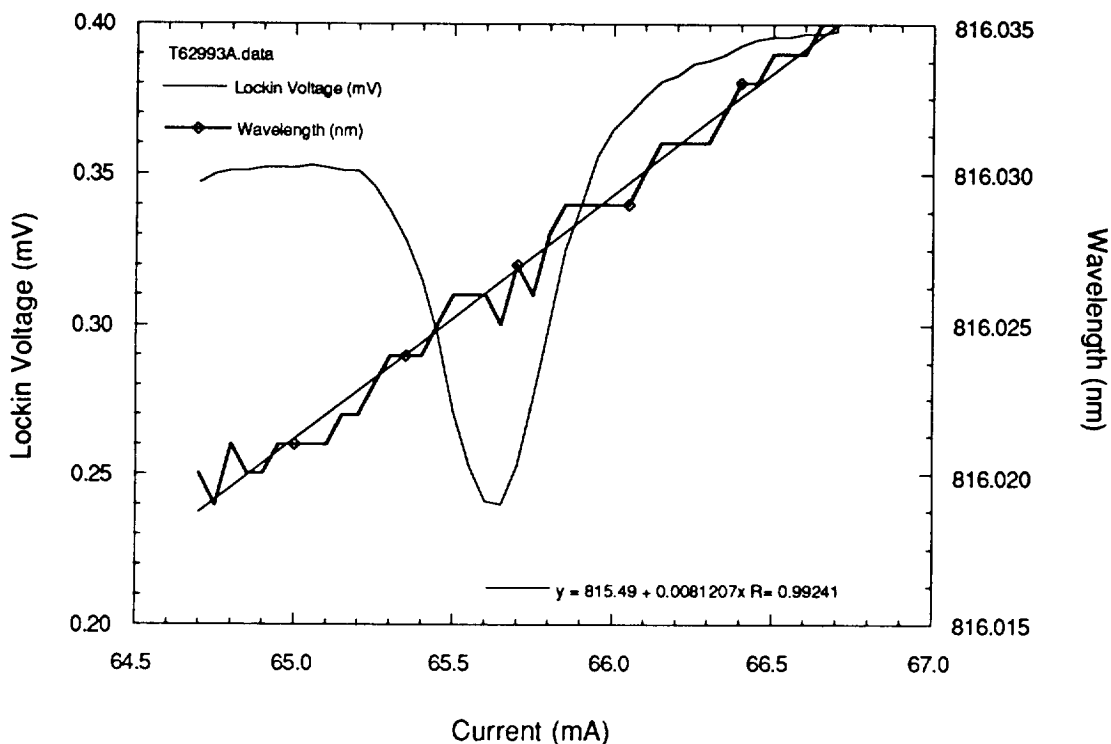


**Figure 24.** Profile of a strong absorption line centered at 816.024 nm.

The wavelength is also plotted in this figure. A simple line fit has been performed on the wavelength and its equation included. The slope of the fit indicates a wavelength tuning rate of approximately 8 pm/mA.

The linewidth and line strength of an absorption line may be estimated from measurements made using second harmonic spectroscopy techniques.[55,56] These

measurements used a low amplitude dither current to modulate the frequency of the laser

emission, a silicon photodiode to detect the light transmitted through an absorption cell,

and a lockin amplifier to observe the first, second, and third derivatives of the

absorption signal.

The chopper wheel was removed and a 4 kHz, 2 mV$_{pp}$ sine wave was superimposed

onto the laser via a 47 $\Omega$ series resistor. The 47 $\Omega$ resistor in series with the laser

diode creates a ~50 $\Omega$ load. The 2 mV sine wave translates to a ~40 µA dither current

which modulates the center frequency of the laser. The laser beam was directed through

the White cell and detected by an EG&G Si PIN photodiode. The photodiode signal was

demodulated by the lockin amplifier with an integer multiple of the dither frequency, $f$.

It has been shown that demodulating with a integer multiple of $f$ yields the integer

derivative, i.e. demodulating with $f$ yields the first derivative, demodulating with $2f$

yields the second derivative, etc.[57] Figure 25 shows the first derivative of the 815.769

absorption line shown in Figure 23.
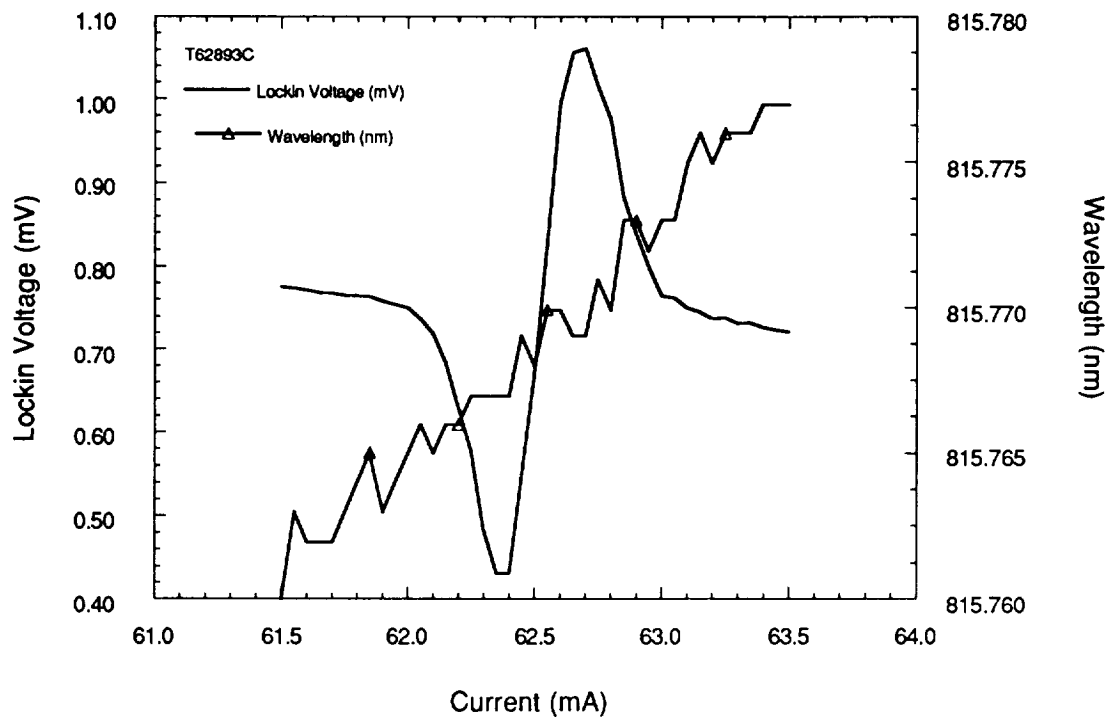
**Figure 25.** First derivative of water vapor absorption line at 815.769 nm. The wavelength is also shown.

The signal strength for the first derivative curve in Figure 25 is higher than the absorption signal in Figure 23 because neutral density filters were removed from the beam. These neutral density filter were used to attenuate the beam prior to entering the White cell so as to not saturate the photodiode. The first derivative of the 816.024 nm absorption line is shown in Figure 26. The wavelength has also been plotted in this figure.
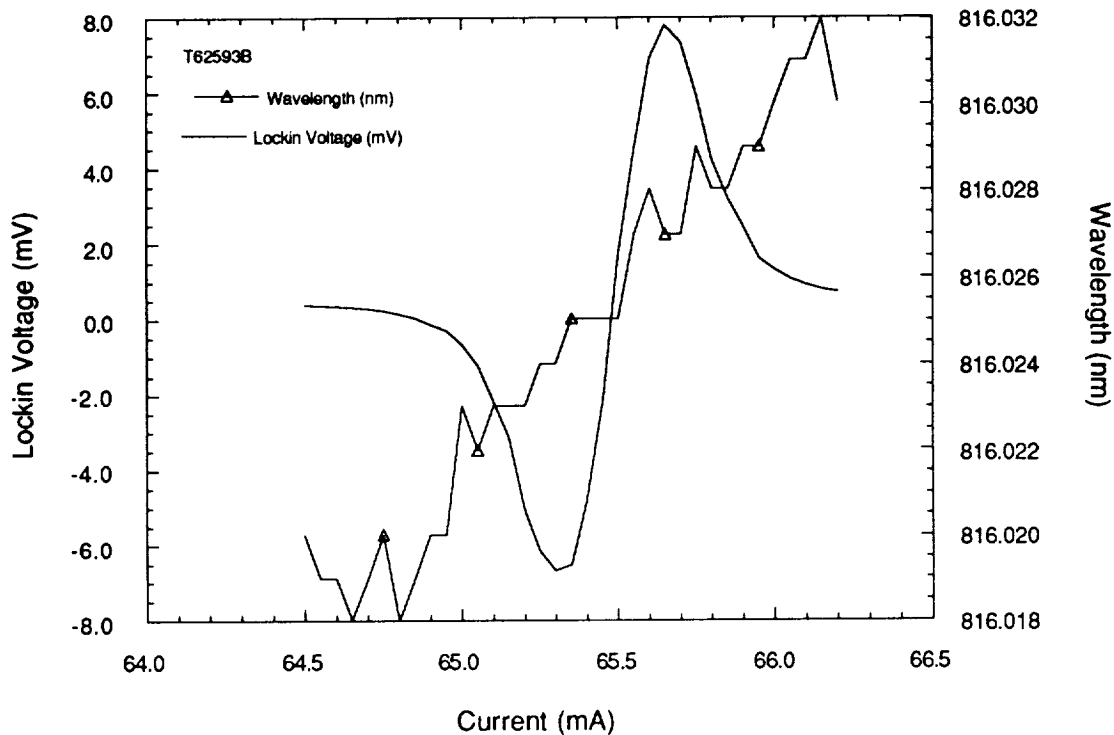
**Figure 26.** First derivative of water vapor absorption line at 816.024 nm. Also shown is the wavelength vs. bias current.

Demodulating the absorption signal with $2f$ yields the second derivative of the absorption signal with respect to current. Figures 27 and 28 show the second derivative of the absorption lines centered at 815.769 and 816.024 nm, respectively. The second derivative curves are all inverted in amplitude. The center of the second derivative should be a positive valued peak reflecting the steep positive slope of the first derivative. This problem has been traced to the autophase (AP) command sent to the lockin amplifier during the initialization and subsequently corrected. Estimation of linewidth and wavelength are unaffected by the relative phasing of the lockin however.
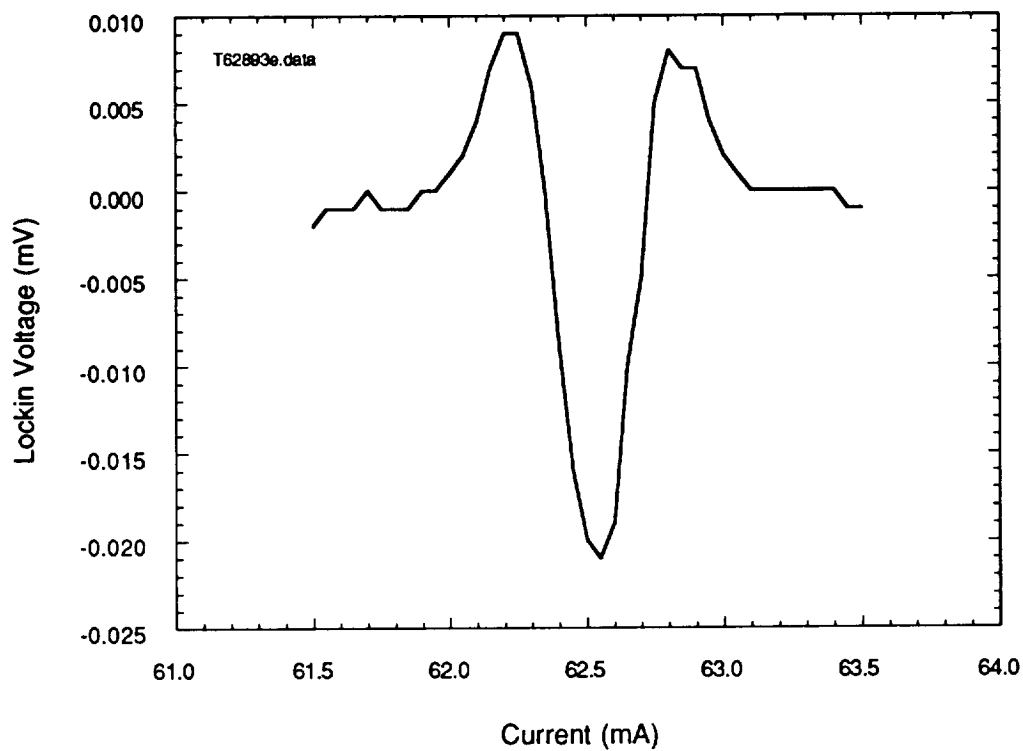
**Figure 27.** Second derivative with respect to current of the absorption feature centered at 815.769 nm.

The full width at half maximum (FWHM) of an absorption line may be estimated from the second derivative curve. The zero crossings of the central peak of the second derivative correspond to the peaks of the first derivative curve which in turn correspond to the points of steepest slope (inflection points) on the absorption line. These points are close to the half maximum points, as long as the absorption is small, $\leq$ 5%, and therefore can be used to define the linewidth. From Figures 27 and 28, the current linewidths are similar and estimated to be approximately 0.350 mA. Using the experimentally determined current tuning ratio of 8 pm/mA the lines are approximately $(0.350 mA) \cdot (8 pm/mA) = 2.8 pm$ wide or $1.4 pm$ halfwidth. Converting the halfwidth from $pm$ to $cm^{-1}$ yields a measured halfwidth of $0.021 cm^{-1}$. At 20 Torr

71

total pressure, the lineshape is dominated by Doppler broadening and the Doppler

halfwidth of this line may be calculated using

$$\alpha_D = \frac{v_o}{c}\left[2k\ln 2 \cdot \frac{T}{m}\right]^{\frac{1}{2}}$$

(91)

where $v_o(cm^{-1})$ denotes line center, $k(ergs/K)$ is Boltzmann's constant, $T(K)$ is the

temperature, $c(cm/\sec)$ is the speed of light, and $m(g/molecule)$ is the mass of the

water molecule. For the line at 816.024 nm the Doppler halfwidth is

$$\alpha_D = \frac{12,254cm^{-1}}{3\times10^{10}cm/\sec}\left[2\left(1.38\times10^{16}ergs/K\right)\ln 2 \cdot \frac{294K}{3\times10^{-23}g/molecule}\right]^{\frac{1}{2}}$$

(92)

or $\alpha_D = 0.0177cm^{-1}$. The difference between measured and calculated halfwidths is

18.8%. This difference is attributable to the choice of the zero crossings of the second

derivative curve to define the linewidth. The peak absorption should be estimated from

the absorption line profile, Figures 23 & 24, and the half-absorption points

determined. However, for weak absorption, ≤5%, the zero crossings of the second

derivative curve are an acceptable approximation to the FWHM.

72
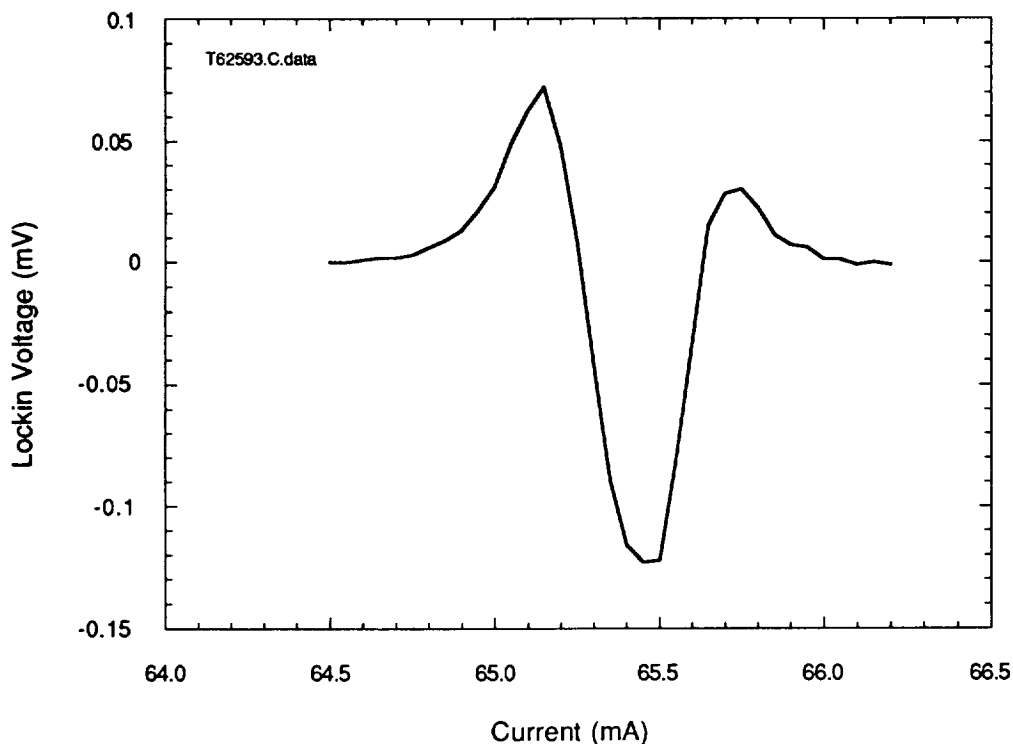
**Figure 28.** Second derivative with respect to current of the absorption feature centered at 816.024 nm.

Demodulating the absorption signal with $3f$ yields the third derivative of the absorption feature with respect to current. Figures 29 and 30 show third derivatives of the absorption lines centered at 815.770 and 816.024 nm. The third derivative is desirable for use as the frequency discriminant in the line locking electronics due to its long linear region through the line center and its nearly zero amplitude offset. The first derivative includes a nearly constant amplitude offset due to the positive slope of the absorption signal which is due to the linear intensity increase with laser diode bias current. This amplitude offset moves the zero crossing of the first derivative curve away from the absorption line center. Therefore locking the laser to the zero crossing of the first derivative would cause an underestimation of water vapor density, in an

73

atmospheric DIAL measurement, since the attenuation due to absorption would be less than it would be at line center.
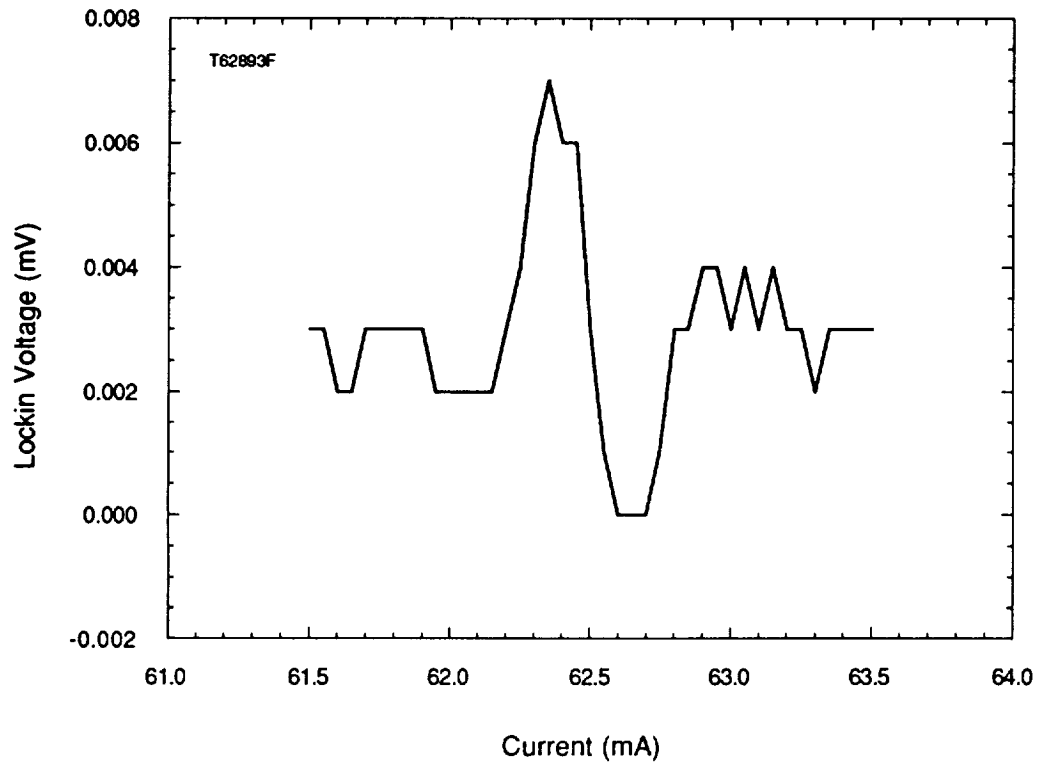


**Figure 29.** Third derivative of the absorption feature centered at 815.769 nm.
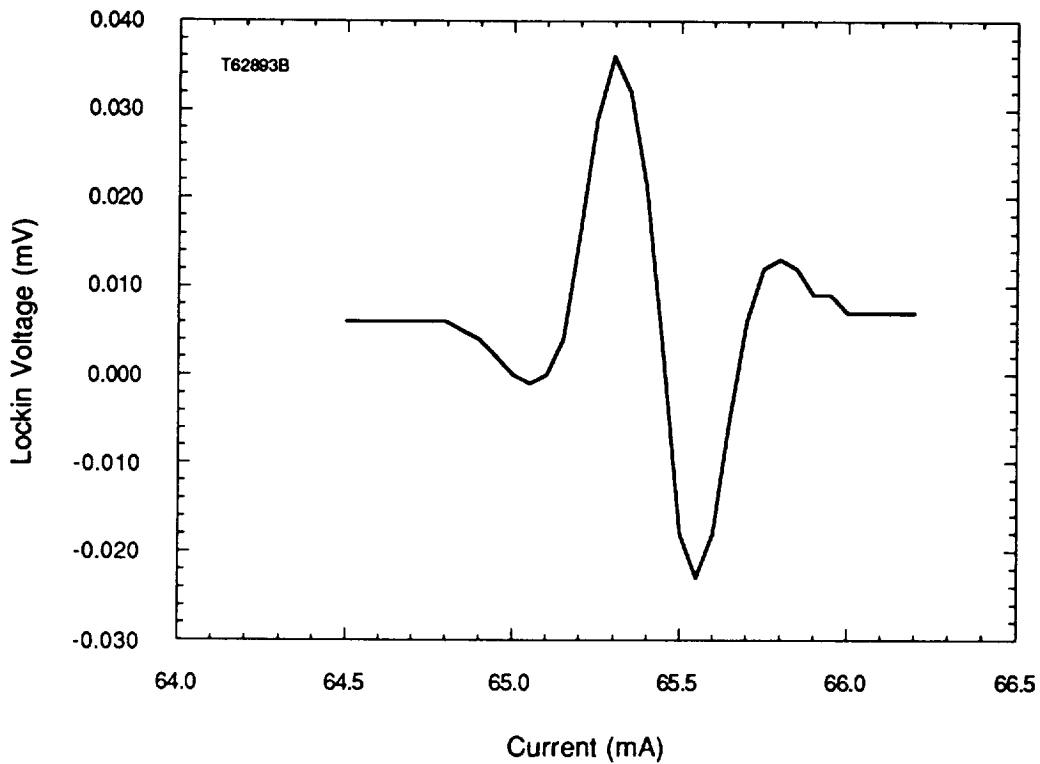
**Figure 30.** Third derivative of the absorption feature centered at 816.024 nm.

The requirements for closed loop frequency locking electronics have been

established from these water vapor absorption line profiling experiments. Pressure

broadened lines have Lorentzian lineshape Eq. (71) which determines how the

absorption coefficient, $k_m$, changes as the laser frequency varies from line center. To

ensure a change of less than 10% in the absorption coefficient, the laser must be locked

to 0.34 of the Lorentz halfwidth. For the Mitsubishi lasers, with ~8pm/mA wavelength

tuning rate, this corresponds to a bias and feedback current stability of ~0.2 mA.

The 100 mW AlGaAs lasers procured for the AlGaAs lidar transmitter (Spectra

Diode Labs SDL 5410) were specified at 816±5 nm. One laser at a time was mounted in

a laser diode header and collimated. Each laser was then checked with a current source and a fiber coupled optical spectrum analyzer. Each laser operated in a single longitudinal mode up to 100 mW and was centered in wavelength at ~812 nm. This required identifying several new candidate absorption lines at 812 nm and profiling these lines with the same water vapor spectroscopy set-up, Figure 16. Two moderately strong lines in this region, 811.006 and 811.617 nm, were selected for use later in the horizontal path water vapor DIAL measurements. These lines permitted using a shorter absorption cell path length. Consequently, a 30 cm long cell with angled windows was used in a multipass configuration. The cell was evacuated and backfilled with ~ 20 Torr of water vapor. The temperature of the cell was not controlled.

A first derivative scan of a line at 811.617 nm is shown in Figure 31. The line strength of this absorption line is $2.54 \times 10^{-24} cm^{-1} / molecule \cdot cm^{-2}$ and it has a pressure broadened linewidth of $0.0837 cm^{-1}$. Also shown in the figure is the wavelength vs. bias current curve. The SDL-5410 laser exhibits a slower current tuning rate, $3.3 pm / mA$, than the Mitsubishi ML5412N laser, $8 pm / mA$. This line was subsequently used in both the horizontal integrated path and the range-resolved water vapor DIAL measurements.
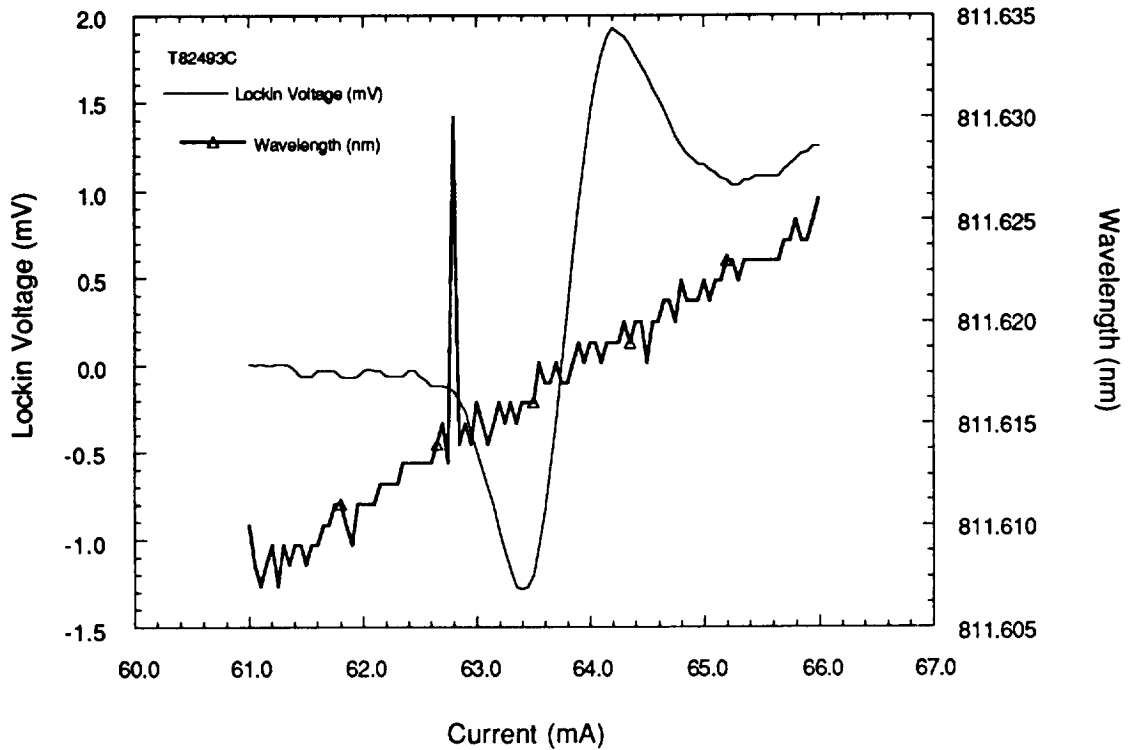
**Figure 31.** First derivative scan of 811.617 nm absorption line using 90 cm absorption path length in a 30 cm absorption cell.

The current linewidth measured from Figure 31 is 0.7 mA which corresponds to a linewidth of $(0.7mA) \cdot (3.3pm / mA) = 2.3\ pm$ and a halfwidth of $0.0175\ cm^{-1}$. This compares well with the calculated Doppler halfwidth of $\alpha_D = 0.0177 cm^{-1}$. The slope of the central portion of the of the first derivative curve is

$$\frac{3mV}{0.7mA} = 4.28\ mV / mA .$$

(93)

## 3.6 Locking an AlGaAs laser to a water vapor absorption line

An AlGaAs laser has been locked, in frequency, to an absorption line using a computer to close the feedback loop. Using a setup similar to the line profiling experiments, the AlGaAs laser was dithered with a 3 kHz, 0.4-0.8 mA sine wave. The collimated laser beam was transmitted through an absorption cell and a photodiode detected the absorption signal. The lockin amplifier demodulated the absorption signal at 3kHz. This generates the first derivative of the absorption signal with respect to current. The wavelength of the laser diode is controlled by a feedback current which is summed, at the laser, with the bias current. The feedback current is determined by the lockin voltage (which is manually set to zero at line center) and by the loop gain which is set by a computer program controlling the feedback current source. The software, which attempts to zero the lockin error, adjusts the gain by examining the lockin error voltages for the last five points. Figure 32 shows a flow chart of the computer algorithm which was used to stabilize the laser wavelength to the water vapor absorption line. The absolute value of the sum of five samples of the lockin voltage is compared with the sum of the absolute values of the same lockin voltages. If the absolute value of the sum is $\geq$ the sum of the absolute values, the loop gain is increased. Conversely if the absolute value of the sum is less than the sum of the absolute values, the loop gain is decreased.
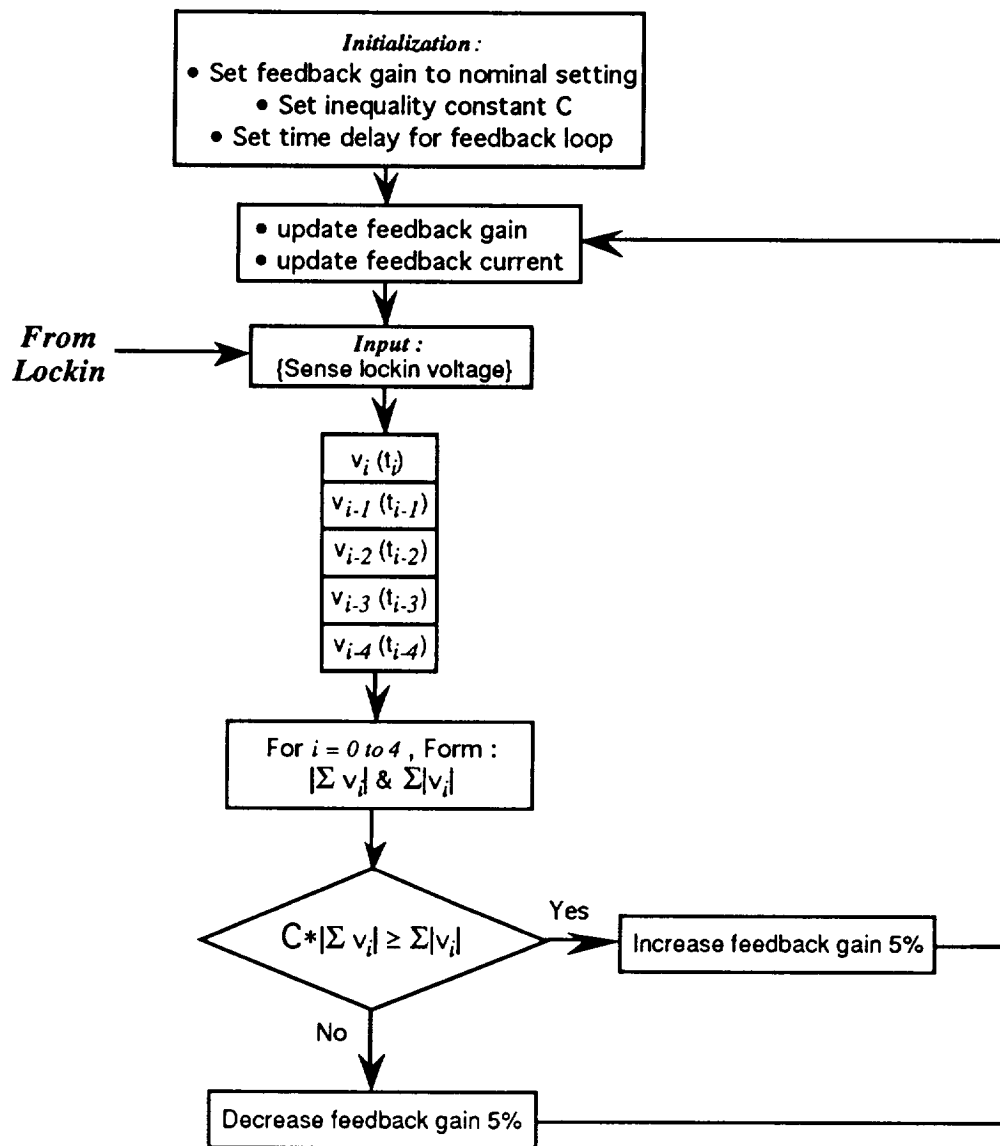
**Figure 32.** Algorithm for laser stabilization to water vapor absorption line.

Frequency stability of the stabilized laser has been measured and recorded using the White cell and lockin amplifier. By ensuring that the laser frequency is stable over the typical lidar measurement period (1-5 minutes), DIAL measurement errors due to wavelength drift of the laser will be reduced. The error signal, generated by the lockin amplifier sensing the transmission signal through the absorption cell, is proportional to

79

the fluctuations of the laser frequency.[58] Figure 33 shows the lockin error signal as a

function of time while the laser was actively stabilized to the center of the absorption

line at 811.617 nm. Each data point corresponds to approximately 1 second. The lockin

error voltage fluctuates approximately $+20 / -30 \, \mu V$ over the ~200 second measure-

ment period. From Figure 31 the amplitude (peak to peak voltage) of the first

derivative of the absorption line at 811.617 nm is measured to be $3 \, mV$. The slope of

the central portion of this curve is estimated to be $4.28 \, mV / mA$.
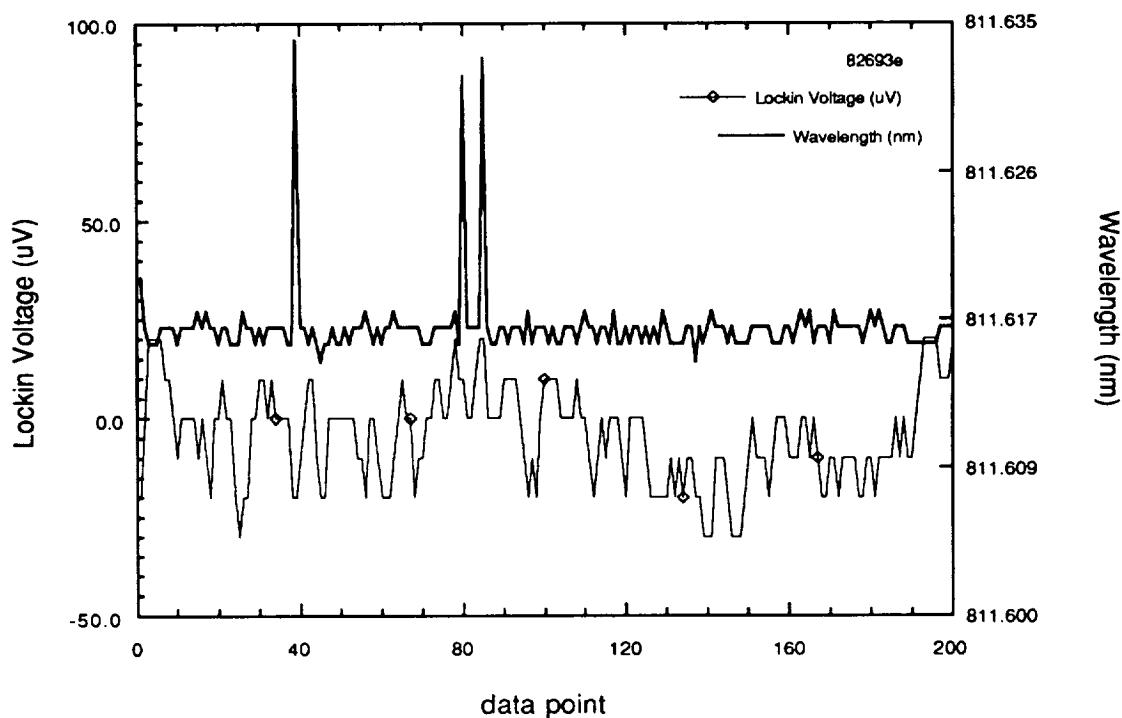


**Figure 33.** Scan of lockin voltage and laser wavelength while laser was actively
stabilized using the computer feedback loop. Each data point corresponds to ~1.0 second.

80

The fraction of the absorption linewidth over which the laser fluctuated during the measurement in Figure 33 is the ratio of the lockin error fluctuations to the amplitude of the first derivative,

$$\frac{50\mu V}{3mV} = 0.016,$$ (94)

or one part in 60. The center frequency stability of the laser is

$$\frac{0.05mV}{4.28mV\,/\,mA} \cdot 3.3pm\,/\,mA = 0.04pm,$$ (95)

over ~200 seconds.

The demonstrated frequency stability of the actively stabilized laser was sufficient to attempt DIAL measurements of atmospheric water vapor. The next chapter describes the hardware assembled for two prototype AlGaAs lidar systems, a single color cloud and aerosol lidar and a water vapor DIAL system.

# 4. PROTOTYPE AlGaAs LIDAR SYSTEMS

Two prototype AlGaAs lidar systems have been assembled and tested. The first is a single color cloud and aerosol lidar and the second is a water vapor DIAL system. Each system is based on a single 100 mW AlGaAs laser diode, a 20 cm diameter Schmidt-Cassegrain telescope, and a silicon Geiger-mode avalanche photodiode (APD). The primary difference between the two systems is the method used to modulate the intensity of the laser diode emission. Both systems use the same receivers and detectors as well as the same histogrammer, data acquisition software, and correlation software. The AlGaAs laser diode used for both lidar systems is discussed in this chapter followed by a detailed description and diagram of each transmitter subsystem. A complete description of the receiver common to both lidar systems is presented as is a description of the data acquisition and histogramming hardware and software.

## 4.1 AlGaAs laser diodes

The laser used in both transmitters is a Spectra Diode Labs SDL-5410-G1 AlGaAs diode laser. This is a single element index guided AlGaAs laser and has a nominal linewidth, inversely proportional to optical power, of 10-100 MHz. Linewidths of AlGaAs lasers have been narrowed to 330 kilohertz with electrical feedback[59]. Single element laser diodes tend to operate, spectrally, in a single longitudinal mode, although a small percentage of power is evident in neighboring modes. The amplitude of these side modes is typically 20-30 dB lower than the dominant mode. A plot of output power vs. bias current is shown in Figure 34. This PI curve shows the optical power for a laser

diode bias current between 50 and 100 mA. The slope of the line is very nearly 1 W/A

which is referred to as slope efficiency. The laser diode package is shown in Figure 35.
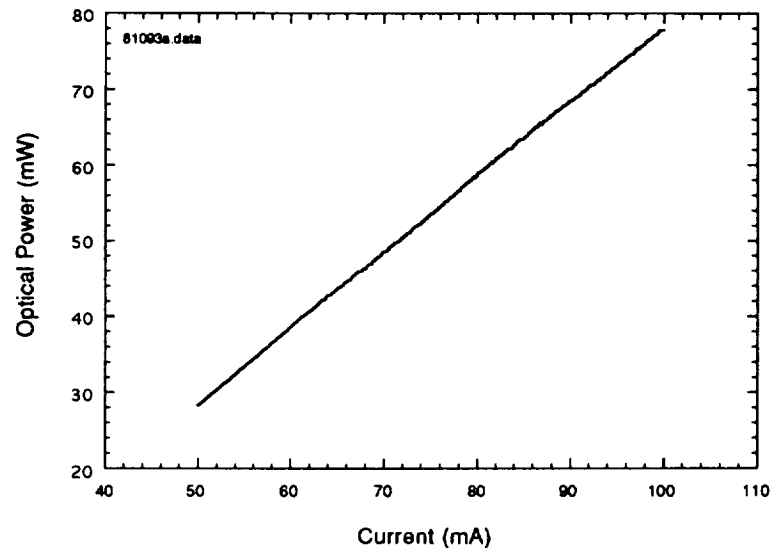


**Figure 34.** PI curve for SDL 5410 G1 AlGaAs laser diode.

The emission wavelength of semiconductor lasers is tunable in both temperature

and bias current. As mentioned in Chapter 3, typical tuning coefficients are 70 pm/°C

and 3.3 pm/mA. These tuning characteristics are used to stabilize the lidar transmitter

to the center of an absorption line for the water vapor DIAL system. The emission

aperture of a single element laser diode is ~ $1 \times 3 \mu m$ and light diverges rapidly with a

3:1 aspect ratio into a cone ~10°×30°. This requires using collimating optics with a

high numerical aperture to collect as much light as possible into a usable beam. Two

commercially available collimating lenses were used. A 0.5 numerical aperture lens

was used in the single color cloud and aerosol lidar. This lens, the LDCO-53-N from

Optics Plus Inc., has three spherical elements with special multilayer anti-reflective

(AR) coatings on all air-glass interfaces. A 0.55 NA glass asphere from Corning, model

83

350150, was used in the water vapor DIAL system.  This singlet had broadband AR coatings on both sides.
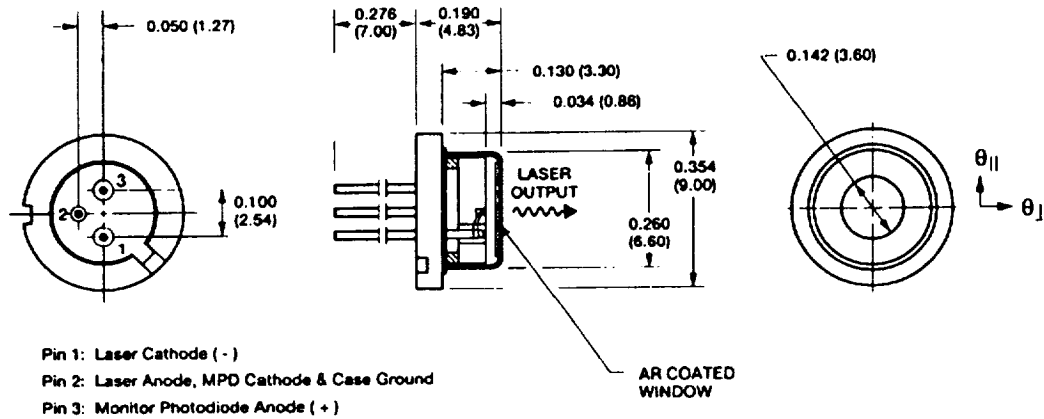


**Figure 35.** Laser diode in the SOT-148 window package [dimensions in inches(mm)]

The AlGaAs lasers used are single element, index guided AlGaAs lasers.  The Mitsubishi ML5412N used in the water vapor spectroscopy experiments are 30 mW, single mode lasers and were selected for their 815-822 nm emission wavelength and their wavelength stability.  The Spectra Diode Labs SDL 5410 used in the lidar systems are 100 mW, single mode lasers and were selected for their high average power, ruggedness, and reliability.

When the wavelength stability of the laser is not crucial, *i.e.* for aerosol and cloud lidar measurements, direct current modulation of the laser diode is used to modulate the intensity of the outgoing beam.  However, for DIAL measurements, the frequency deviation of the laser wavelength caused by modulating the drive current precludes maintaining the frequency stability required for these measurements.  For

this reason, an external, electro-optic modulator was used to modulate the intensity of a frequency stabilized CW AlGaAs laser.

## 4.2 Single color cloud and aerosol lidar transmitter

In the single color cloud and aerosol lidar, the current to the laser diode is modulated with a maximal length PN code. This current modulation directly modulates the intensity of the laser output. There is no monitoring of the laser diode wavelength. A system diagram is shown in Figure 36 and system components are listed in Table 10.
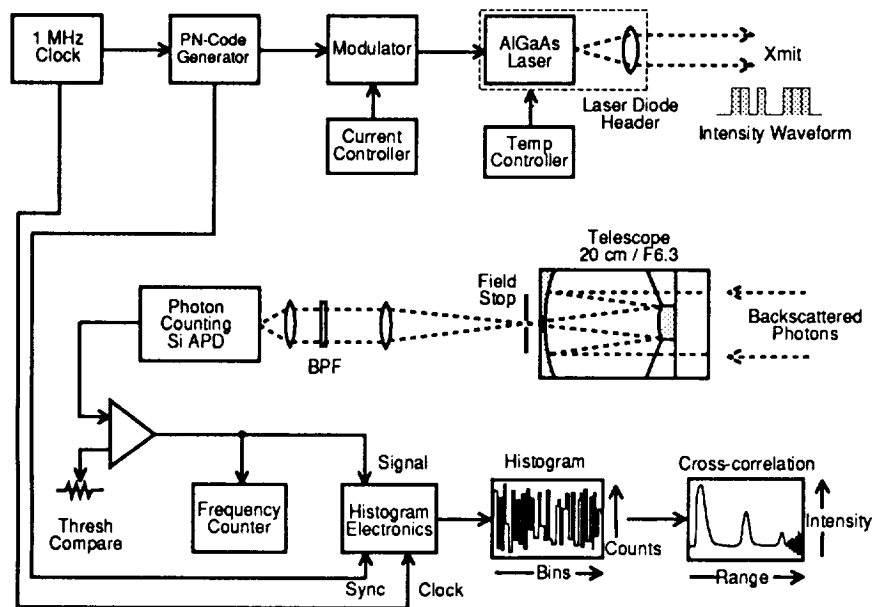


**Figure 36.** Cloud and aerosol AlGaAs lidar system diagram.

The laser transmitter for the single color cloud and aerosol AlGaAs lidar is based on the 100 mW laser diode, Spectra Diode Labs SDL-5410-G1. The cap which protects the laser diode has been removed so that a short focal length collimating lens can be used.

85

An optical and mechanical mount for the laser diode and collimating lens was designed previously[60] and is used in the AlGaAs lidar transmitter. The laser diode header provides a rugged optomechanical design, good thermal interface, and an electrical interface capable of ≥ 100 MHz modulation.

**Table 10**

Cloud and aerosol lidar system components.

| | |
|---|---|
| AlGaAs laser | Spectra Diode Labs, SDL 5410-G1 |
| Collimating lens | Optics-Plus LDCO-53-N, NA=0.5 |
| Beam expander | Rodenstock model #4401 2x-8x, adjust. |
| PN code generator | Custom, 1 MHz, 31-4095 bit codes |
| Receiver telescope | Meade 20 cm diameter F/6.3 |
| Optical bandpass filter | Andover, 810 nm, 10 nm FWHM |
| Detector | EG&G SPCM-200 Photon Counting Module |
| Discriminator | Tennelec, TC-453 |
| Histogrammer | Custom, 4095 bits long, 32 bit depth |
| System computer | Gateway 486/33 |

4.2.1 Current and temperature controller

The single color cloud and aerosol lidar requires only ±0.1 mA bias current accuracy and ±0.1°C temperature stability, therefore an integrated current-temperature controller was used in conjunction with a digital modulator circuit to control the laser diode. The proportional-integral temperature controller works with an Analog-Devices AD-590 integrated temperature sensor and a thermo-electric cooler (TEC) to form a closed loop temperature controller with 0.1°C accuracy. The current controller is manually adjusted to a bias current up to 60 mA with 0.1 mA accuracy and a modulation current up to 100 mA. The digital modulator circuit accepts an ECL digital signal and converts it to an analog modulation current which is summed with the bias current at the diode.

## 4.3  Water vapor DIAL transmitter

The water vapor DIAL system, using the same SDL-5410-G1 laser diode, requires that the laser wavelength be tuned in wavelength both to the center of a water vapor absorption line and to a nearby non-absorbing region.  To achieve this tuning and the necessary current stability, two programmable current sources are used.  A Hewlett-Packard computer was used to control both current sources.  A separate temperature controller was used in a closed loop configuration to stabilize the temperature of the laser diode header to within 0.02°C.  An electro-optic light intensity modulator was used to impress the PN code onto the laser intensity.  Therefore, the laser is run CW and no digital modulation circuitry is needed.  A smaller laser diode header was designed for the SDL-5410-G1 laser package, Figure 35, and single element aspheric collimating lens.  The laser diode cap including window, which covers the laser diode, was removed so that the Corning asphere lens could be used.  A system diagram is shown in Figure 37 and major system components listed in Table 11.

C-2.

Temp Controller

Bias Current Source

Laser Diode Header

AlGaAs Laser

-40 dB Isolator

BS

EO Modulator

Xmit

Feedback Current Source

3 kHz Dither

-40dB Isolator

Driver

Bias

Intensity Waveform

HP 9000 Computer

Lockin Amplifier

Si PIN Diode

10 m White Cell

Fiber Optic

BS

Wavemeter

Mirror

1 MHz System Clock

PN-Code Generator

Telescope 20 cm / F6.3

Field Stop

Backscattered Photons

Photon Counting Si APD

BPF

Thresh Compare

Frequency Counter

Signal

Histogram Electronics

Histogram

Cross-correlation

Counts

Intensity

Sync

Bins →

Range →

Clock

Gateway 486 Computer

Figure 37. AlGaAs lidar water vapor DIAL system diagram.

The transmitter for the water vapor DIAL system has more stringent wavelength requirements than the cloud and aerosol lidar. Therefore, the integrated current and temperature controller previously used for the cloud and aerosol lidar was replaced by two programmable current sources (Keithley model 220 programmable current source) running in parallel and a proportional-integral temperature controller (Alpha-Omega TC Series 2 temperature controller).

## Table 11

Water vapor DIAL system components.

| | |
|---|---|
| AlGaAs laser | Spectra Diode Labs, SDL 5410-G1 |
| Laser current sources | Keithley 220 program. current source |
| Beam expander | Rodenstock model #4401 2x-8x, adjust. |
| Collimating lens | Corning molded glass asphere, NA=0.55 |
| Xmit temperature controller | Alpha-Omega TC Series 2 |
| Xmit temperature sensor | 10 k$\Omega$ thermistor |
| Active temp. device | Marlow, SP-1666 Thermo-electric cooler |
| Absorption cell | Connecticut Instruments, Pathfinder Cell |
| Lockin amplifier | SRS Model 530 Dual phase lockin amp. |
| PN code generator | Custom, 1 MHz, 31 - 4095 bit codes |
| External light modulator | ConOptics Model 3, Electro-Optic Modulator |
| Receiver telescope | Meade 20 cm diameter F/6.3 |
| Optical bandpass filter | Andover, 810 nm, 5 nm FWHM |
| Detector | EG&G SPCM-200 Photon Counting Module |
| Discriminator | Tennelec, TC-453 |
| Histogrammer | Custom, 31-4095 bit length, 32 bit depth |
| Data acquisition computer | Gateway 486/33 |

### 4.3.2 Current sources and laser frequency control loop

The two programmable current sources were controlled by a Hewlett-Packard 9000 series computer via the IEEE-488 computer interface. One current source was used to bias the AlGaAs laser to its CW operating point while the second current source was used to provide the closed-loop feedback current to the laser. This feedback current was set by a computer program which senses the error signal, approximately once a second, from the lockin amplifier The wavelength of the laser diode is controlled with the feedback current using the 3.3 pm/mA transfer function of the laser previously measured in Chapter 3. The feedback current is determined by computer algorithm, Figure 32.

### 4.3.3 Temperature controller

The temperature control loop uses an proportional-integral temperature controller, a 10 kΩ thermistor, and a custom thermo-electric cooler (TEC) to close the loop. The use of a 10 kΩ thermistor with the temperature controller provides 0.02°C resolution in sensing temperature. The temperature controller is bipolar, capable of driving as well as sinking current. The TEC device, which uses the Peltier effect, is also a bipolar device which can heat as well as cool. The Peltier cooler uses many junctions of two dissimilar metals, which generates a heat flow at the junction when a voltage potential is placed across it.

### 4.3.4 Electro-optic light modulator

The EO modulator, Con-Optics Model 3 Light Intensity Modulator, employs a Potassium Dideuterium Phosphate (KD*P) electro-optic crystal to digitally modulate the polarization vector of the laser beam and a Glan-Thompson polarizer, oriented at 90° to the input polarization, to convert the polarization modulation into intensity modulation. This technique is attractive for AlGaAs lasers since they have polarization ratios greater than 100:1. The EO crystal is electrically biased to the half-wave voltage and the digital TTL modulation signal rotates the polarization between maximum extinction and maximum transmission. A linear polarizer or analyzer on the input improves the performance of the modulator by initially rejecting any unpolarized light. KD*P was chosen because of its ≥ 90% transmission at 820 nm and its 80% modulation depth at a modest (<100VDC) half-wave voltage.

The modulator has been characterized with the transmitter laser using a fast Si APD detector and power meter. The optical power and modulation depth were first

optimized by adjusting alignment, rotation, and bias voltage of the modulator. The power

was measured at the output of the laser diode header, after the beam splitter, at the input

of the EO modulator, and again at the output of the EO modulator. This data is shown in

Figure 38. Optical PN code waveforms were recorded at the output of the EO modulator

and are shown in Figure 39. The input power to the modulator was 5.17 mW and the

average output power from the modulator was 1.71 mW. The peak transmission is

therefore 66% assuming a 50% duty cycle of the PN code modulation.
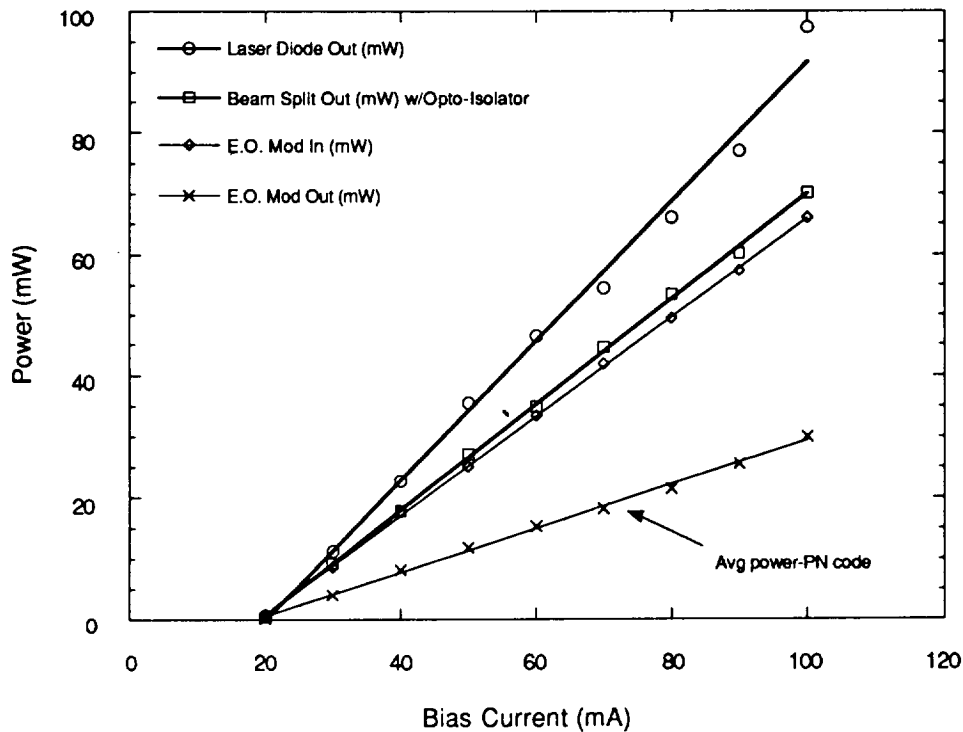


**Figure 38.** Power vs current characterization of the AlGaAs DIAL transmitter.
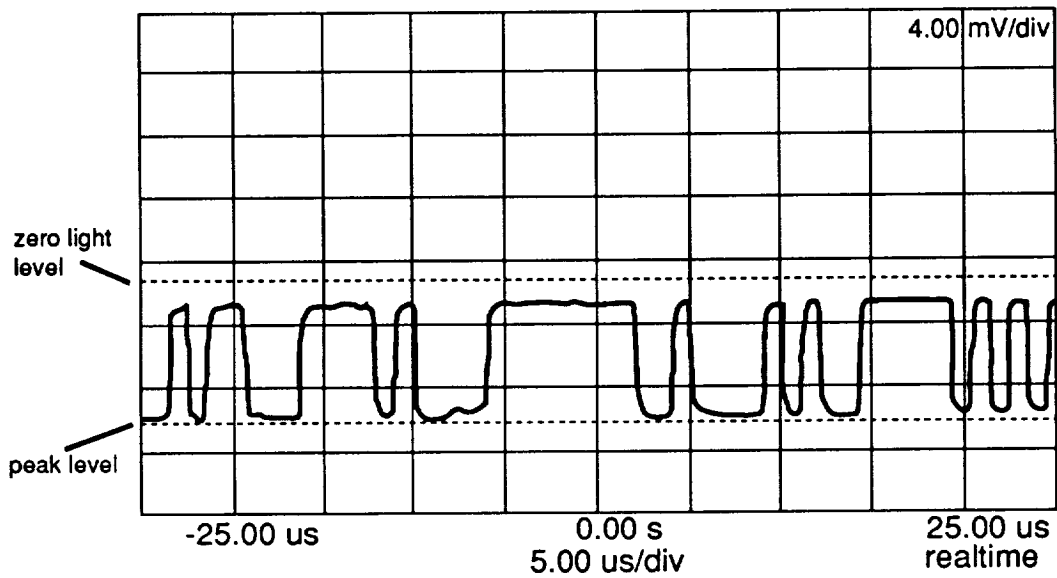
**Figure 39.** PN code optical waveform produced by the EO modulator with a -125 VDC bias.

With the laser blocked, the detector output was -1.125 mV. The digital zero and one light levels were -2.55 mV and -9.875 mV respectively. The modulation depth is

$$\frac{\left|(-9.875mV)-(-2.550mV)\right|}{8.750mV} = 0.84 , \tag{96}$$

for a modulation depth of 84%.

## 4.4 PN code generator

In preparation for this work, shift register code generator circuit designs were reviewed and a general purpose maximal length sequence generator was designed. The design was implemented in TTL fast logic (74F-series) to ensure good quality modulation waveforms up to 10 MHz bit rates. A schematic diagram of the PN code generator is shown in Figure 40. Twelve D flip-flops form the shift register elements of the PN code generator. Selected outputs are fedback to the input of the first shift register element via a network of exclusive-OR gates.

The code generator is capable of driving ECL, TTL, and 50 $\Omega$ loads and provides a synchronization pulse at the start of every code sequence. The code generator produces sequence lengths from 31 bits to 4095 bits. To test that the circuit correctly produced maximal length PN codes, a sequence at each code length was accumulated and cross-correlated with an ideal code generated by a computer algorithm. Each code sequence produced by the code generator correlated perfectly with the computer generated codes.
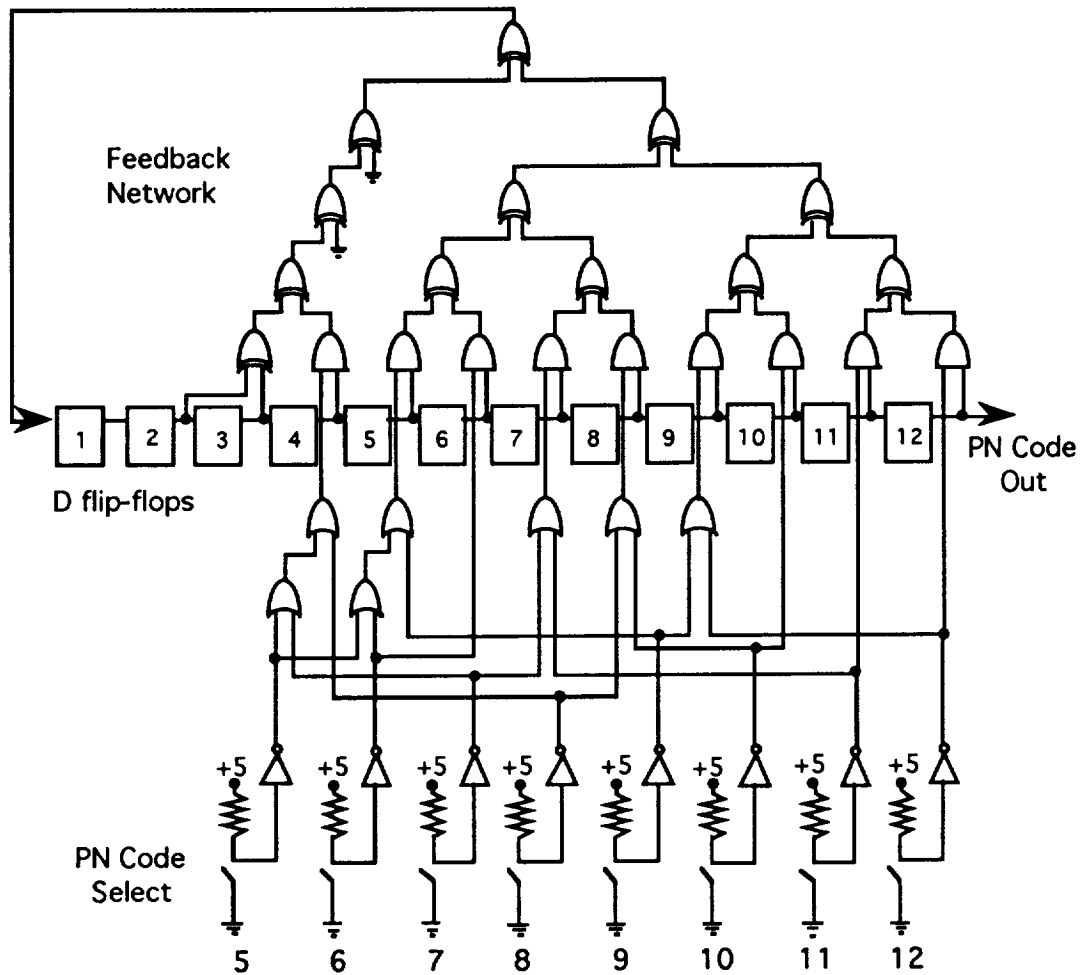
**Figure 40.** Schematic diagram of PN code generator with adjustable code lengths from 31 to 4095 bits.

4.5 Beam expander & pointing mirror

The laser diode beam divergence must be known and less than the receiver FOV. The diffraction-limited divergence, $\theta$, of a $TEM_{00}$ mode laser, measured at the $1/e^2$ points, is

$$\theta = \frac{4\lambda}{\pi d_o},$$ (97)

where $\lambda$ is the wavelength and $d_o$ is the diameter of the beam waist. An adjustable beam expander is used to increase the outgoing laser beam waist, $d_o$, in order to reduce the laser divergence to less than 100 μrad. The beam expander, Rodenstock model #4401 2x-8x expander, has a maximum exit aperture of 31 mm at 8x expansion. This corresponds to a diffraction limited divergence of ~3.5 μrad. A precision mirror mount is used to direct the outgoing beam to within the receiver FOV.

## 4.6 Receiver

The receiver system used for both the single color cloud and aerosol lidar and the water vapor DIAL system is based on a 20 cm telescope, additional aft optics, bandpass filter, and a silicon avalanche photodiode used in the photon counting or Geiger mode.

### 4.6.1 Telescope/receiver optics

The lidar receiver uses a commercially available, Meade 20 cm diameter, F/6.3 Schmidt-Cassegrain telescope. A 200 μm pinhole was placed at the primary focus of the telescope creating a field stop. The receiver field of view (FOV) is

$$FOV = \frac{200 \mu m}{1280 mm} \approx 156 \mu rad.$$ (98)

Light passing through the field stop is recollimated by a 50 mm focal length achromat. The field stop and achromat are mounted to the rear of the telescope in an adjustable black delrin housing. Once assembled, the telescope, including recollimation optics, was

95

mounted to the azimuth/elevation (AZ/EL) stage of a 40 cm white light collimator. The collimator filled the aperture of the receiver telescope with plane waves of white light. The pointing of the telescope was adjusted until light passed through the field stop. The focus of the telescope was adjusted to maximize light through the field stop. Telescope pointing was checked and adjusted often during this process. Once the telescope focus was optimized, the aft optics were adjusted to provide collimated light to the detector module. A small autocollimating telescope was used to monitor the output of the lidar telescope and aft optics to ensure that collimation was achieved. Once collimated, the aft optics were marked and the threads of the adjustable delrin housing tacked in place with adhesive.

### 4.6.2 Si Geiger-mode APD/photon counting detector

The detector used was a silicon avalanche photodiode (Si APD) biased in the Geiger-mode of operation.[61] In this mode, single photons may be detected as electrical pulses. An incoming photon is absorbed and produces a photoelectron which is amplified in the avalanche process. A circuit compares the pulse voltage with a preset level and outputs a TTL signal when the pulse voltage exceeds the preset level. One drawback of the Geiger-mode APD is the dead time between output pulses. The device, which is passively quenched, requires approximately 200 nsec to recharge. Hence, it is limited to count rates below $10^6 counts/$ sec for a linear response and $10^7 counts/$ sec using a correction factor.

The maximum sensitivity of this detector is confined to a radius of 50 $\mu$m from its center which makes the receiver optical design critical. A 20 mm focal length laser doublet focuses the light onto the active area of the detector. To reduce the background

photoelectron count rate, an optical bandpass filter was mounted in front of the focusing doublet. The bandpass filter and laser doublet fit in an adjustable aluminum housing which mounts to the front of the photon counting module. This black anodized housing effectively seals the detector from stray light. The assembled detector module was mounted to the AZ/EL stage of the 40 cm white light collimator and adjusted while monitoring the photoelectron count rate on a frequency counter. The pointing of this module was sensitive due to the small active area of the detector and the short focal length lens. Therefore, pointing was checked and adjusted whenever the focus of the detector module was adjusted. Once optimized, a knurled ring was used to lock the focus adjustment.

### 4.6.3 Alignment of integrated receiver

The telescope, with its integral aft optics, and detector subsystem were integrated to a common aluminum breadboard. The optical alignment of these two subsystems is critical. The telescope and field stop define the lidar receiver optical axis and the detector subsystem must be aligned to it. The integrated receiver was mounted to the AZ/EL stage of the 40 cm white light collimator. Initially, the detector was blocked with a small piece of cardboard to prevent saturation. The AZ/EL of the collimator was adjusted to maximize light through the receiver optics. The detector position was adjusted visually to the center of the recollimated light. The collimator light intensity was then attenuated, the detector turned on, and the photoelectron count rate monitored on a frequency counter. Detector position was adjusted to optimize the photoelectron count rate. Once the detector was bolted in place no further adjustments to the receiver were necessary.

## 4.7 Data acquisition & histogramming

A histogramming circuit, shown in Figure 41, was developed [37] which accumulates received photoelectrons into memory elements synchronously with the transmitted PN code sequence. There is one memory element per bit of the PN code sequence and the unit is capable of accumulating counts at a 2 MHz count rate continuously with no dead time. The histogrammer was built as a single AT expansion board to fit within the Gateway 486 system computer. Software has been developed to control the histogrammer, transfer data from the histogramming memory to the computer hard drive, and compute the cross-correlation function.
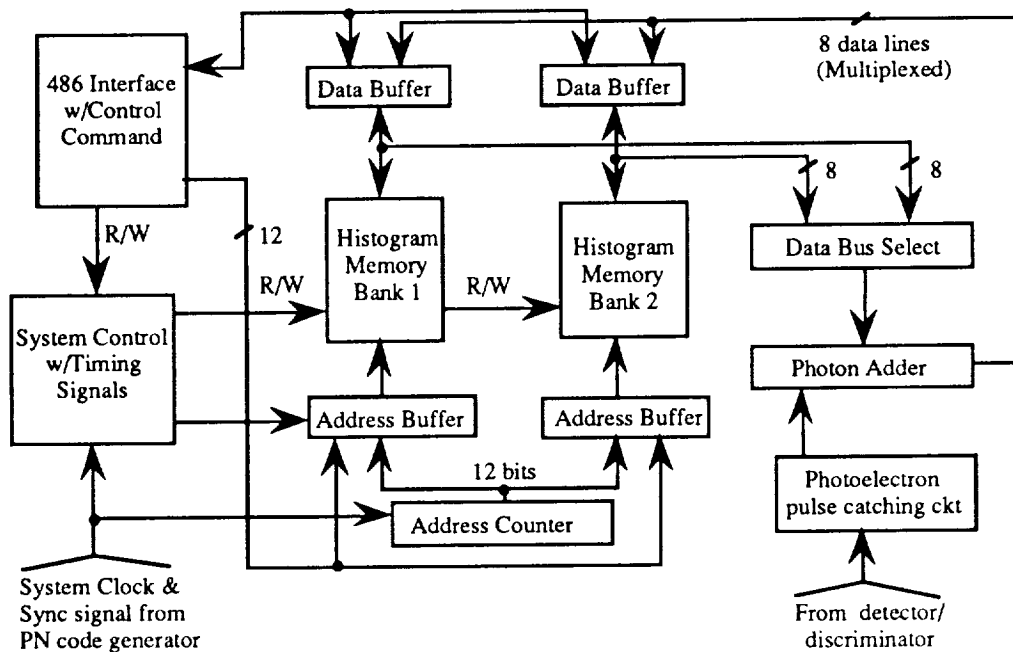


Figure 41. Block diagram of histogramming electronics on an AT expansion card.

### 4.7.1 Histogrammer operation

The histogrammer and PN code generator are clocked by an external frequency generator. The histogrammer senses an 8 bit long sync pulse from the PN code generator which determines the start of the histogram. The sync pulse resets the address counter in the histogrammer. The address counter begins counting and continues counting until the next sync pulse. Meanwhile, a pulse catching circuit consisting of several D flip-flops latches an in-coming photoelectron pulse generated by the detector and simultaneously latches the address, where the detected pulse occurred, into an address buffer. The memory contents at this address are moved to a photon adder where its value is incremented by one. The new value is moved back to the data buffer and written to the same memory address. Two parallel memory units, each 4 Kbits long by 32 bits deep, are used to eliminate any dead time associated with transferring the memory contents to the computer. While one memory unit is accumulating photoelectron counts the other is writing data to the computer. When the counting memory unit gets to half full, a flag is set and the computer disables this unit and enables the empty memory unit to start counting incoming pulses. The computer then begins transferring the memory contents of the nearly full memory unit to the hard drive.

Software has been developed to control the histogramming electronics as well as manage the accumulated histograms, compute correlation functions, and display the histograms and correlations on the computer display.

The histogrammer was tested by applying clock and sync signals while holding the input to the pulse catching circuit first at ground and then to a high TTL signal. The histogrammer was allowed to accumulate for several seconds. With a grounded input, the

99

histogrammer performed as expected and recorded no counts in any histogrammer bin. With the input tied high however, the histogrammer did not perform perfectly. There was typically a discrepancy of one count per bin between the bins in the first half of the histogram and the bins in the second half. Also, the last bin of the histogram would not accumulate counts. The one count per bin discrepancy had a negligible effect on correlation functions of long integration time measurements and was ignored. The zero count in the last bin of the histogram was found to have significant impact on the correlation function, especially during long integration periods or during measurements with high average count rates. For this reason the system software was modified to set the count in the last bin to the average count in all of the histogrammer bins. While this is not correct, simulations have shown that it does not induce a significant error in the correlation function and that it does reduce the error caused by the zero count in the last bin.

The next chapter presents lidar measurements made with the two prototype AlGaAs lidar systems. The lidar data is analyzed and compared with theory wherever possible.

# 5. LIDAR MEASUREMENTS & DATA ANALYSIS

Once assembled and boresighted, the AlGaAs lidar was used to make several different lidar measurements. These lidar measurements consisted of ranging over horizontal paths to terrestrial targets and measurements of clouds and aerosols over slant paths. In addition, DIAL measurements of atmospheric water vapor were made over horizontal paths in both integrated path and range resolved modes. This chapter summarizes results from these measurements and provides analysis of the data, including range correction, SNR calculation, and an estimate of laser diode frequency stability. Also, an error analysis of the water vapor DIAL measurements is performed.

## 5.1 Horizontal path measurements to terrestrial targets

The AlGaAs lidar was used to range over horizontal paths to terrestrial targets at ranges of 0.5 to 13 km. The lidar was operated at a single, unstabilized wavelength with direct current modulation by a PN code. The AlGaAs lidar is a biaxial lidar system with a small transmitter divergence, $\leq 100\,\mu rad$, and a narrow receiver FOV, $160\,\mu rad$, it is therefore susceptible to small changes in the boresight alignment (the transmitter to receiver alignment). The overlap function was optimized for ranges >5 km. This was done by adjusting the transmitter pointing mirror while observing photoelectron count rates from distant targets. The strong backscattered signals from these targets reduced integration times and permitted near real-time correlation of the received signal with the transmitted signal which facilitated the alignment process. By comparing the backscattered photoelectron count rate with the expected count rate, calculated using

101

the single scattering lidar equation and the system parameters, any serious problems could be identified.

### 5.1.1  Alignment method #1

Two methods were used to align the transmitter and receiver axes of the AlGaAs lidar.  The first boresight method used a target board on which cross-hair marks were made at positions with the same vertical and horizontal separation distances as the transmitter pointing mirror and receiver telescope.  A 20 mW HeNe laser was mounted to the lidar transmitter to provide a visible (632.8 nm) laser pointer.  A third mark was added to the boresight board corresponding to the HeNe's position.  The telescope was focused to its respective mark on the boresight board by viewing through the receiver telescope with either an eyepiece or a charge coupled device (CCD) camera.  The HeNe laser and AlGaAs laser transmitter were turned on and their pointing adjusted until each laser overlapped its proper mark on the boresight board.  Using a CCD camera made the AlGaAs laser spot visible on the video display.  The boresight board was then moved farther away from the lidar while the position of the boresight marks and laser spot were monitored.  The telescope was refocused and the AlGaAs laser transmitter pointing mirror adjusted to bring it back into alignment.  Finally, the telescope was focused at objects on the local horizon, 12-15 km away.  This insured that the telescope was focused effectively at infinity.

### 5.1.2  Alignment method #2

The second alignment method employed a 12.7 cm hollow corner cube retro-reflector (CCR) to redirect the transmitter laser light back into the telescope.  With the

AlGaAs laser operating above laser threshold, the transmitted light was directed into the edge of the CCR. The manufacturing tolerance on the CCR was 2 $arc$ sec $(9.7\mu rad)$. Since the CCR translates the return beam by approximately its aperture size it allowed the transmitter to reflect directly into the telescope. A piece of translucent mylar was placed at the exit aperture of the telescope. With an infrared (IR) viewer, the transmitter pointing mirror was adjusted until a bright spot appeared on the mylar. The intensity of this spot was maximized with further fine adjustment of the pointing mirror.

With adequate neutral density filters in the transmitter path, the photon-counting detector was turned on and the photoelectron count rate monitored with a frequency counter. The photon counting detector had been previously aligned to the axis of the telescope using the 16" white light collimator. The transmitter pointing mirror alignment was adjusted to maximize the count rate. Once the alignment was optimized, the laser drive current was reduced to less than 1.0 mA and the neutral density filters were removed. This was to check for angular misalignment due to using multiple neutral density filters. Since the optical system alignment was preserved, the need for ND filters was eliminated and in all subsequent experiments this alignment method was used for boresighting the AlGaAs lidar.

### 5.1.3 Measurements to terrestrial targets

Several horizontal path lidar measurements to terrestrial targets were made from the rooftop lidar laboratory of Building 22. Several terrestrial targets are visible from this lab, including trees at various ranges, a water tower at ~5 km range, and power line towers near the local horizon, approximately 12 to 15 km range. Figure 42

shows an altimetry measurement to a water tower at ~5 km. System parameters for this measurement are listed in Table 12. This nighttime measurement was made with 35 mW of average power and an integration time of one-second. A 4095 bit PN code was used at a bit rate of 1 MHz. The horizontal measurement resolution was 150 m and the data has not been smoothed nor range-corrected. The background count rate was 300 counts/second during the measurement.



**Figure 42.** Nighttime, horizontal path lidar measurements to a water tower with 35 mW average transmit power and a 1 second integration time.

Table 12

Lidar system parameters for lidar measurement shown in Figure 42.

| | |
|---|---|
| Avg. laser power | 35 mW |
| PN code length | 4095 bits |
| Count rate | 220 Kcounts/sec |
| Background count rate | 300 counts/sec |
| Transmitter divergence | ≤ 100 urad |
| Receiver FOV | 160 urad |
| Bit rate | 1 MHz |
| Integration time | 1 sec |

The calculated signal-to-noise ratio (SNR) for the water tower return in Figure 42 is

$$SNR = \frac{S_n}{\sqrt{\sum_{i=0}^{4095} N_i}} = \frac{1.34 \times 10^5 \, counts}{\sqrt{2.1 \times 10^5 \, counts}} = 292. \tag{99}$$

Here $S_n$ is the photoelectron count of the correlation peak corresponding to the water tower and the denominator of Eq (99) is the sum of all counts in the histogram. Using the single scattering lidar equation Eq. (19) and the lidar system parameters, Table 12, the expected photoelectron count rate for a 5 km horizontal path at sea level from a target with a diffuse surface reflectivity of 0.5 is calculated to be $\dot{N} = 5 \times 10^5$ counts / sec. A system transmission constant, $\tau_{sys} = 0.5$, and atmospheric attenuation coefficient $\kappa = 0.1 \, km^{-1}$ are assumed. This attenuation coefficient is the sum of the aerosol scattering and absorption terms and a molecular scattering term for mid-latitude summer with 23 km visibility. The molecular absorption term has been assumed negligible. The total counts received in the one-second integration period was $N = 2.1 \times 10^5 counts$. The observed count is approximately a factor of two lower than the calculated count rate. The lower rate is likely attributable to errors in the assumed values of the attenuation coefficient $\kappa$, the system transmission $\tau_{sys}$, and the diffuse reflectivity of the water tower. A better estimate of the target reflectivity is ~0.9 which is based on the diffuse reflectivity of magnesium oxide paint on steel.[62] However this would lead to a larger discrepancy between observed and estimated count rates.

Figure 43 shows a lidar measurement to a terrestrial target at approximately 13 km. This measurement was made at night with 35 mW of average power and a one-

second integration time. A 255 bit PN code was used at a 1 MHz bit rate. The lidar

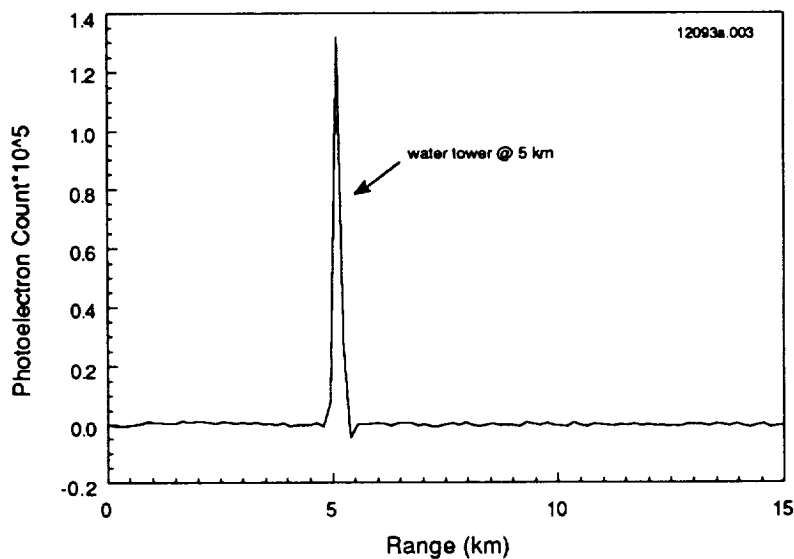system parameters for this measurement are listed in Table 13.
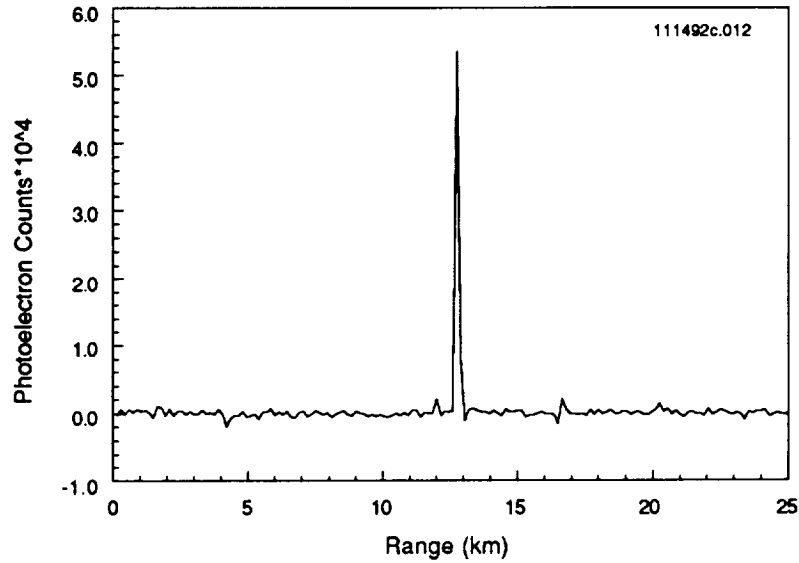


**Figure 43.** Nighttime lidar measurements to a power-line tower with 35 mW average transmit power and a 1 second integration time.

## Table 13

Lidar system parameters for lidar measurement shown in Figure 43.

| | |
|---|---|
| Avg. laser power | 35 mW |
| PN code length | 255 bits |
| Count rate | >150 Kcounts/sec |
| Background count rate | 5.2 Kcounts/sec |
| Transmitter divergence | ≤ 100 urad |
| Receiver FOV | 320 urad |
| Bit rate | 1 MHz |
| Integration time | 1 sec |

The calculated SNR for the target return in Figure 43 is

$$SNR = \frac{S_n}{\sqrt{\sum_{i=0}^{255} N_i}} = \frac{3.4 \times 10^4 counts}{\sqrt{9.4 \times 10^4 counts}} = 175.$$

(100)

The expected photoelectron count rate for this measurement as calculated by the lidar equation, using the system parameters in Table 13 and atmospheric parameters as in the previous calculation, is $1.54 \times 10^4 counts / sec$. The total received counts in the one-second measurement was $9.4 \times 10^4 counts$. The target is believed to be a power line tower with a large cross section central support. Daytime observations with binoculars reveal a series of these large power line towers in the target area, all painted with a highly reflective white paint. The only other targets in the area are trees. Previous lidar measurements to trees have never yielded such strong correlation peaks. The observed count rate is approximately a factor of six higher than the calculated count rate. It is possible that the strong lidar return is due to a high reflectivity paint used on power line towers to improve their visibility to low flying aircraft. The paint likely has characteristics which enhance its specular reflectivity.

## 5.2 Cloud & aerosol lidar measurements

The single-color, direct-current modulated, AlGaAs lidar system was also used to make lidar measurements of clouds and aerosols over slant paths. Once alignment was verified over a horizontal path, the system was pointed above the horizon, at several different elevation angles, and permitted to integrate for many minutes. Figure 44 shows a measurement taken on the night of January 20, 1993 with 20 minutes of

integration time.  The laser was operated at 35 mW average power and modulated with

4095 bit code at a 1 MHz bit rate.  The lidar system parameters are listed in Table 14.

The data has been smoothed with a two-bin running average.  Rayleigh scattering is

evident up to approximately 9 km.  Although that night was particularly clear with

numerous stars visible, a thin layer of cirrus clouds is evident in the data at an altitude

of approximately 13 km.  This data has been range-corrected but not corrected for the

overlap function.  The calculated SNR at the peak of the cirrus return, prior to range-

correction, is

$$SNR = \frac{S_n}{\sqrt{\sum_{i=0}^{4095} N_i}} = \frac{3.2 \times 10^4 \, counts}{\sqrt{5.1 \times 10^6 \, counts}} = 13.9 \ .$$

(101)
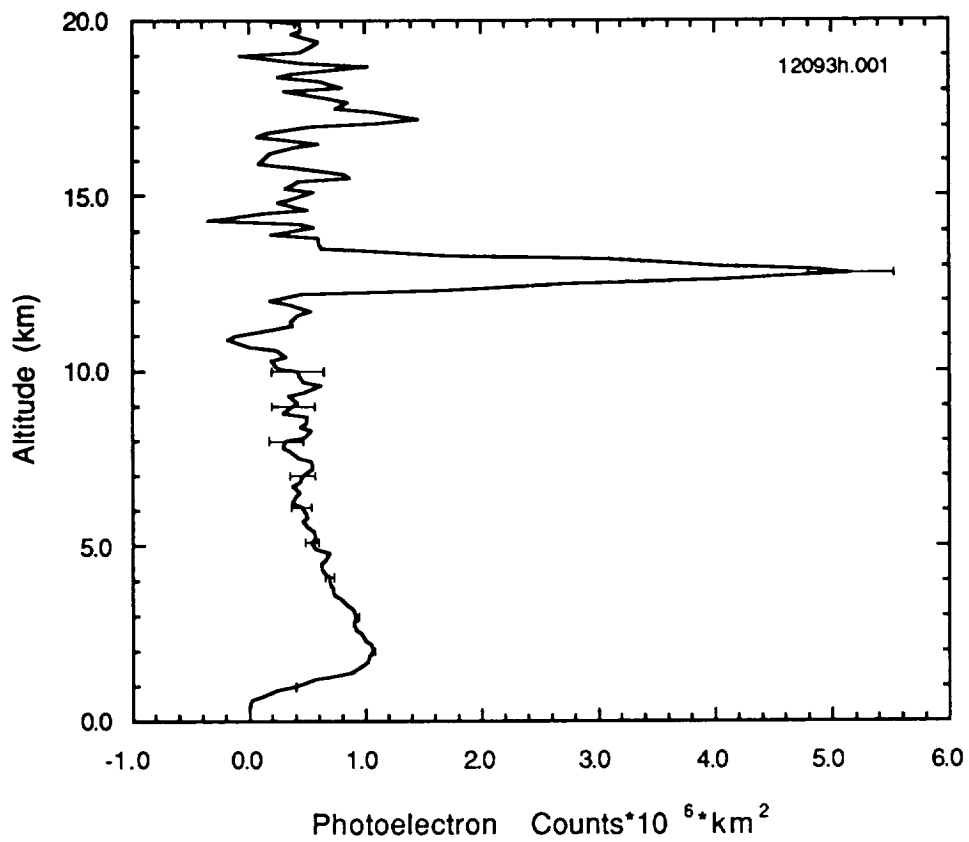
**Figure 44.** Slant path lidar measurements to thin cirrus clouds at night.

The Rayleigh backscatter, visible in Figure 44 to 9 km, may be compared with a model

of the atmospheric molecular backscatter and the total attenuation coefficient at

$0.82\,\mu m$. Figure 45 shows a plot of the product of the volume backscatter coefficient and

the attenuation coefficient.[63]
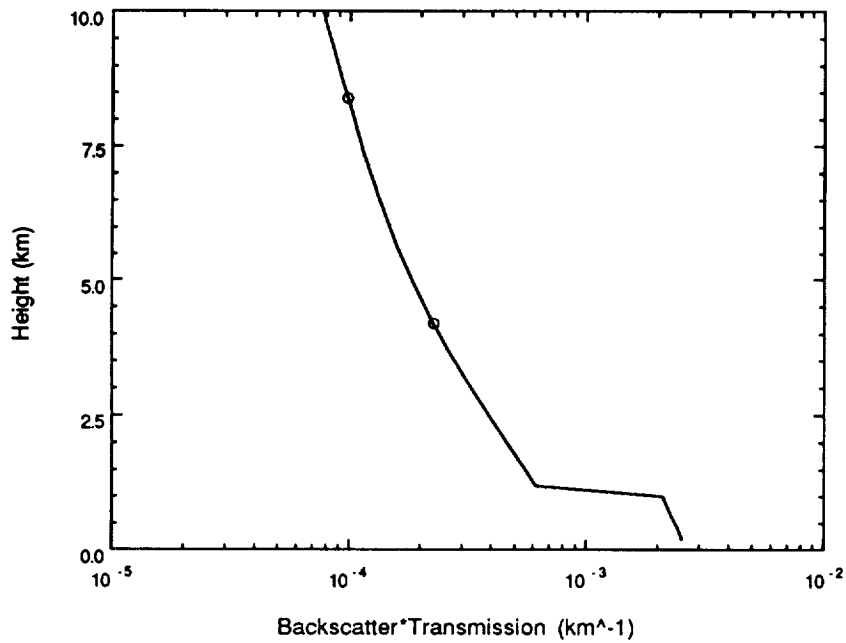
**Figure 45.** Model of atmospheric backscatter and total attenuation coefficient vs altitude. [Spinhirne]

The lidar data in Figure 44 does not show the increased boundary layer particulate scattering seen in the model. This is due to the lidar transmitter not completely overlapping the receiver until ~2 km altitude. However, the slopes of both the lidar data and the model atmosphere are similar in the region from 2-10 km. This comparison is shown in Figure 46.
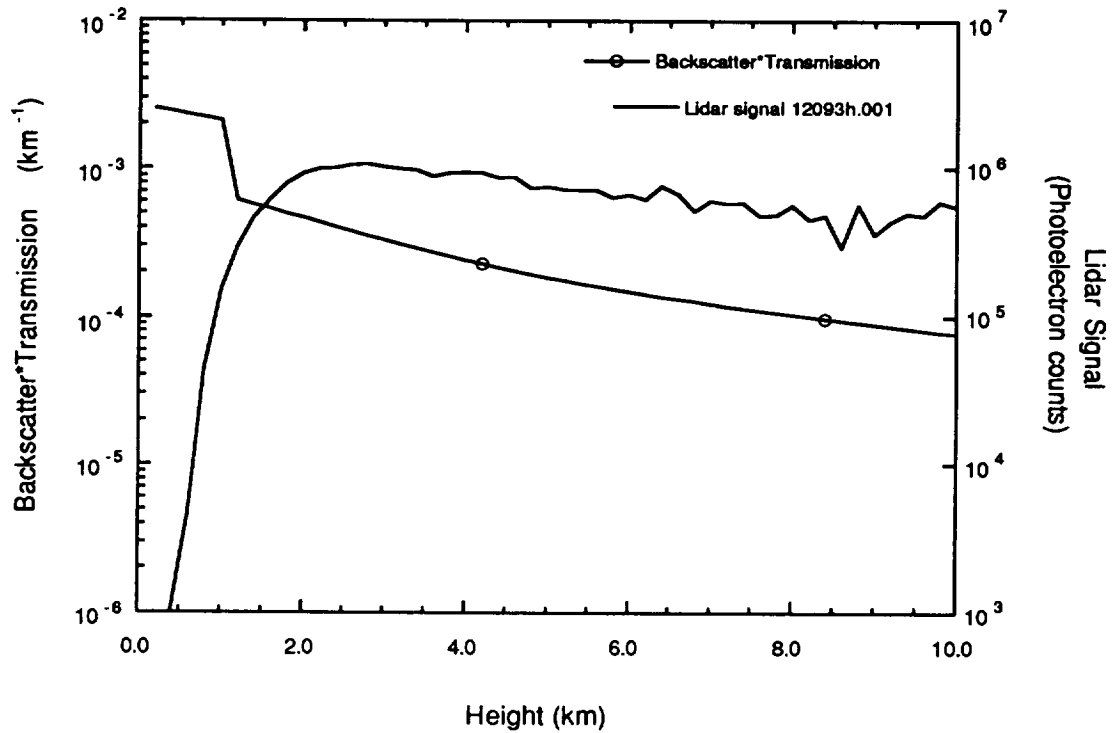
**Figure 46.** Comparison of model atmosphere with lidar data shown in Figure 44.

Figure 47 shows a 20 minute lidar measurement taken immediately following the measurement shown in Figure 44. System parameters are listed in Table 14. A new cirrus layer forming below the layer in Figure 44 is apparent.

**Table 14**

Lidar system parameters for cirrus cloud lidar measurements.

| | |
|---|---|
| Avg. laser power | 35 mW |
| PN code length | 4095 bits |
| Count rate | 7-9 Kcounts/sec |
| Background count rate | 140 counts/sec |
| Transmitter divergence | ≤ 100 urad |
| Receiver FOV | 160 urad |
| Bit rate | 1 MHz |
| Integration time | 1200 sec |
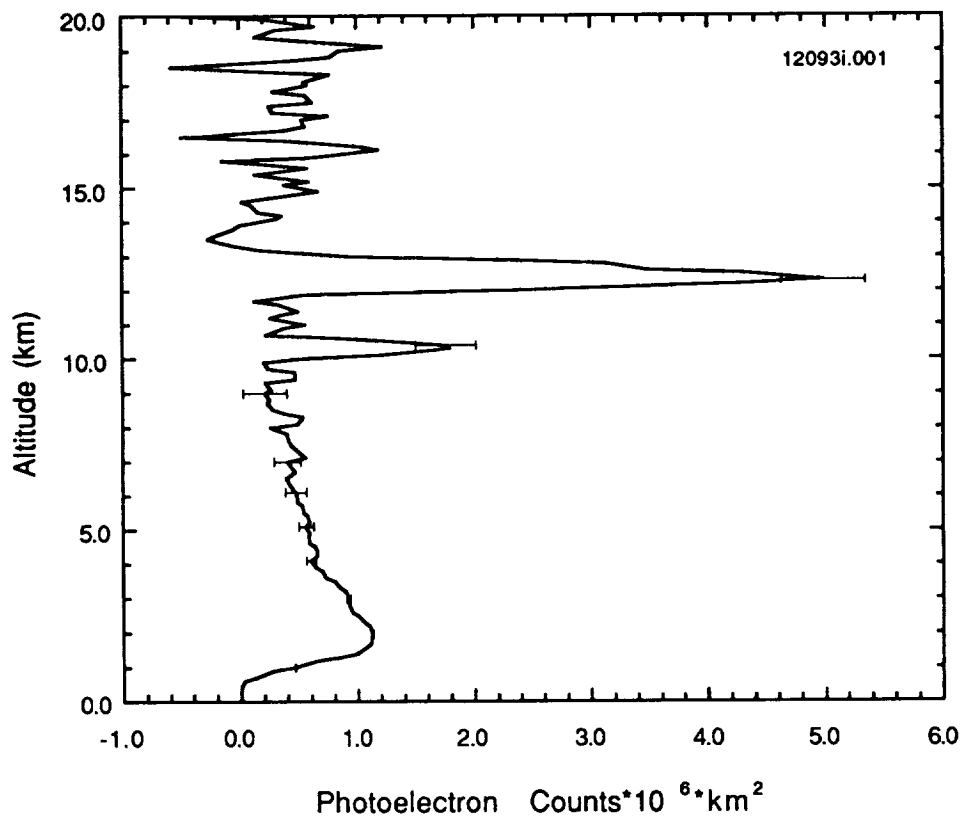
**Figure 47.** Slant path lidar measurements to thin cirrus cloud layers at night.

## 5.3 Integrated path water vapor DIAL measurements

The lidar system depicted in Figure 37 has been used to make integrated path DIAL measurements of water vapor over a horizontal path through the boundary layer at night. Integrated path measurements return the average water vapor density over the measurement path, and allow greater measurement sensitivity at the expense of range information. For the on-line measurement, the AlGaAs laser was locked to an absorption line at 811.617 nm. This line has a halfwidth, $\gamma$, of 0.0837 $cm^{-1}$ at STP and a line strength, $S$, of $2.54 \times 10^{-24} cm^{-1} / molecules \cdot cm^{-2}$. The off-line measurement, made after the on-line, used the same laser actively stabilized at 811.640 nm, 23 pm away

from the absorption line. Figure 48 shows a 75 second integration for each on-line and

off-line measurement. System parameters for the measurement are listed in Table 15.

The largest peak in the figure is due to the reflection from a water tower at 5.1 km.
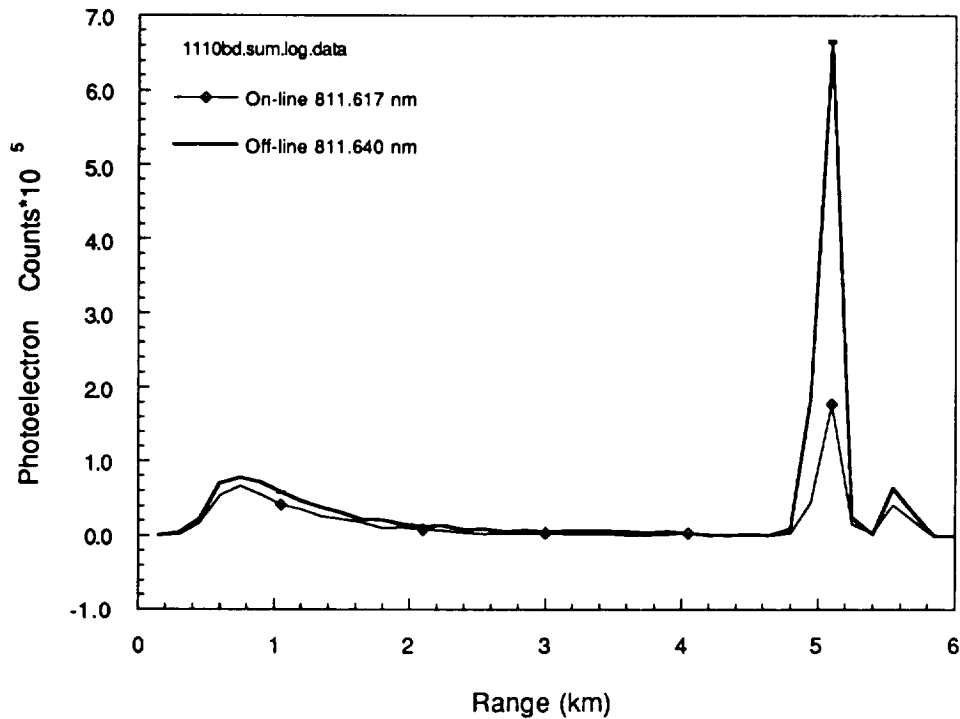


**Figure 48.** Integrated path DIAL measurements of water vapor over a horizontal path at night. Error bars are shown but very small due to strong signal.

**Table 15**

System parameters for water vapor lidar measurements shown in Figure 48.

| | |
|---|---|
| Avg. laser power | 25 mW |
| PN code length | 1023 bits |
| On-line count rate | 10.5 Kcounts/sec |
| Off-line count rate | 23 Kcounts/sec |
| Background count rate | 150 counts/sec |
| Transmitter divergence | ≤ 100 urad |
| Receiver FOV | 160 urad |
| Bit rate | 1 MHz |
| Integration time | 75 sec |

113

The ratio of the on-line to off-line peak is 0.268 and represents the integrated path attenuation due solely to water vapor. The integrated path absorption coefficient may be estimated using the Beer-Lambert attenuation law,

$$e^{-2k_{H_2O} R} = 0.268. \tag{102}$$

This yields a measured absorption coefficient, $k_{H_2O}$, of 0.129 $km^{-1}$. At the time of the measurement, the mean surface pressure reported by a local airport was 1025 mb with a vapor pressure of 5.64 mb. The absorption coefficient at line center for this vapor pressure, assuming a pressure broadened Lorentz line shape, is defined as

$$k_o = n \cdot S_o / \pi \cdot \gamma_o, \tag{103}$$

and is calculated to be 0.138 $km^{-1}$. The measured absorption coefficient is 6.5% lower than calculated. The error is due to four possible sources (1) the lidar is separated 30 km from the airport, where the reported surface and vapor pressure were measured, (2) the 0.8 mA sinusoidal current dither on the laser diode which causes a sinusoidal wavelength variation of ±1.3 pm around the absorption line center, (3) the frequency offset involved with manually closing the feedback loop, and (4) interference from a weak absorption line very close in wavelength to the absorption line at 811.617 nm.

The first error source may be minimized by making humidity measurements at the lidar's location. The second error source, which leads to an underestimation of the water vapor density, may be accounted for by calculating the average or effective absorption coefficient rather than the line center absorption coefficient. The third error source, which also leads to an underestimation of the water vapor density, is more

114

difficult to account for in the data and is best dealt with by using the third derivative of the absorption line as the locking signal. Error sources (2) and (3) are dealt with in section 5.5, Error analysis. The fourth error source should lead to an overestimation of absorption and is best dealt with by selecting better isolated lines.

## 5.4 Range resolved water vapor DIAL measurements

The AlGaAs water vapor DIAL system was pointed above the horizon, to several different elevation angles, in order to eliminate returns from terrestrial targets. Again, both on-line and off-line data sets were accumulated with the laser wavelength stabilized throughout each one-minute measurement. Due to the proximity of the paths, the horizontal range-resolved humidity measurements should agree with the average humidity estimated from the integrated path measurements of the previous section. Figure 49 shows a single on-line measurement from the night of October 28, 1993. The lidar was pointed 2-3° above the horizon. The AlGaAs laser was actively stabilized to the 811.617 nm absorption line throughout the one-minute measurement. System parameters for the lidar measurements are listed in Table 16.

**Table 16**

System parameters for range-resolved DIAL measurements of atmospheric water vapor.

| | |
|---|---|
| Avg. laser power | 20 mW |
| PN code length | 255 bits |
| On-line count rate | 0.38 Kcounts/sec |
| Off-line count rate | 0.55 Kcounts/sec |
| Background count rate | 50 counts/sec |
| Transmitter divergence | ≤ 100 urad |
| Receiver FOV | 160 urad |
| Bit rate | 1 MHz |
| Integration time | 60 sec |
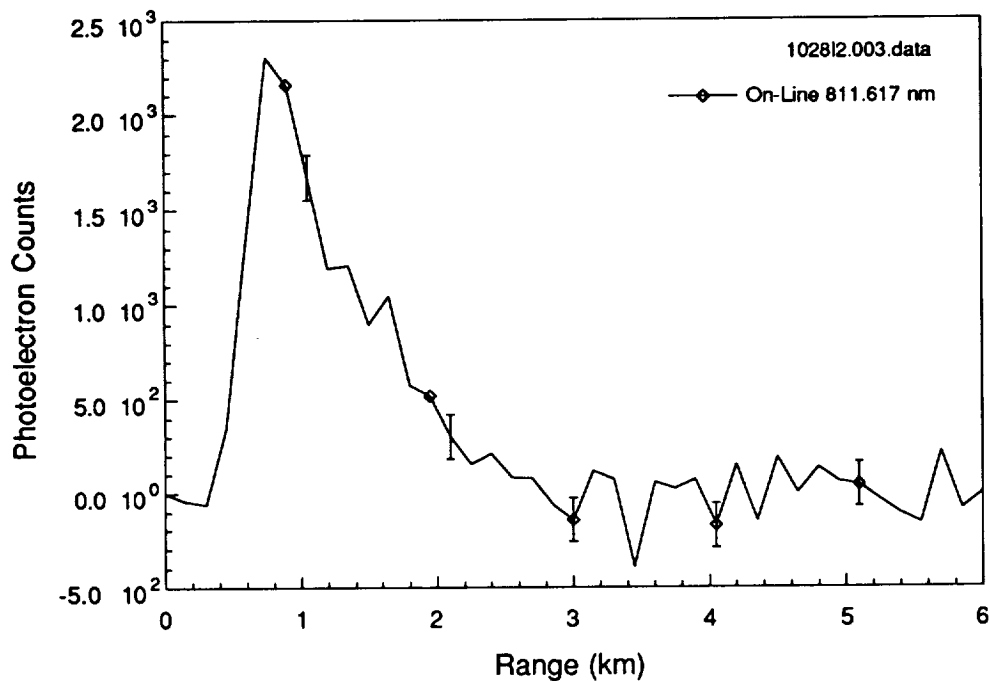
**Figure 49.** Range resolved lidar measurement of water vapor with laser tuned to line center of the 811.617 nm water vapor absorption line. Trajectory is 2-3° above the horizon with a one minute integration time and 20 mW average power.

This data has not been range corrected or smoothed. From the figure, it is evident that the transmitter beam is not completely overlapped by the receiver FOV until a range of nearly 1.0 km. The exponential attenuation of the lidar signal from 1 to 3 km agrees with the $1/R^2$ losses and the Beer-Lambert attenuation law. The off-line measurement, Figure 50, was made shortly after the on-line measurement. The integration time was one-minute and the trajectory was 2-3° above the horizon. The laser was actively stabilized to 811.635 nm for the duration of the one minute measurement.
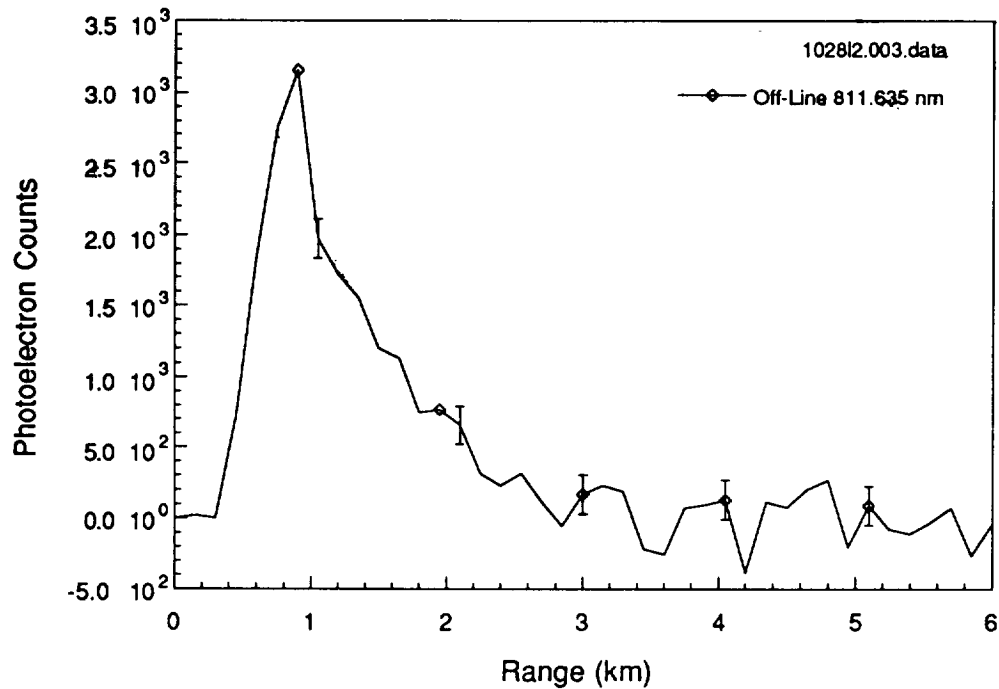
**Figure 50.** Range resolved lidar measurement with laser tuned to 811.635 nm, away from the water vapor. Trajectory is 2-3° above the horizon.

This data has not been range corrected or smoothed. For ease of comparison, Figures 49 and 50 are replotted on the same axes, Figure 51. The difference between the on-line and off-line lidar signals is primarily the absorption due to water vapor and to a lesser extent, the difference in transmitted power caused by tuning the laser wavelength with bias current. If we assume a slope efficiency of 0.3 mW/mA for the AlGaAs lidar transmitter, Figure 38, then the difference in on-line to off-line average transmitted power is ~1.5 mW or approximately a 5% change in the transmitted power. The difference in the peak photoelectron counts between on-line and off-line, at 1 km range, is ~25%. Therefore, the change in transmitted power accounts for ~20% of the difference in the on-line to off-line lidar signals.
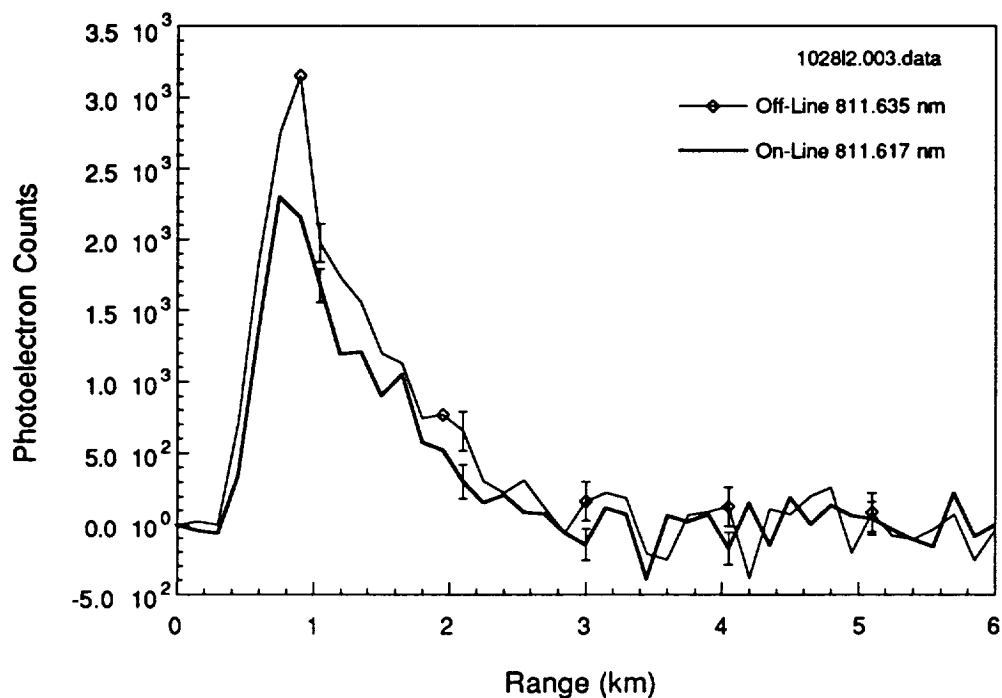
**Figure 51.** Overlay of one-minute on-line and off-line range resolved water vapor DIAL measurements.

By increasing the integration times, the signal to noise ratio (SNR) of the measurements may be improved. To retain some temporal information however, individual one or two minute histograms are accumulated consecutively rather than as one long histogram. Afterwards, the histograms are added together and then cross-correlated with the PN code. Figure 52 shows on-line and off-line lidar profiles of two twelve minute measurements. The system parameters are listed in Table 17. The laser was actively stabilized to the 811.617 nm absorption line for the on-line measurement and to 811.640 nm, ~23 pm away from the absorption line center, for the off-line measurement. The correlation functions of twelve one minute histograms were summed together for each lidar profile.

118

## Table 17

System parameters for water vapor lidar measurements shown in Figure 52 & 53.

| Avg. laser power | 25 mW |
| PN code length | 255 bits |
| On-line count rate | 0.38 Kcounts/sec |
| Off-line count rate | 0.55 Kcounts/sec |
| Background count rate | 50 counts/sec |
| Transmitter divergence | $\leq$ 100 urad |
| Receiver FOV | 160 urad |
| Bit rate | 1 MHz |
| Integration time | 60 sec |

Since the data accumulation (histogramming) and cross-correlation are linear operations, the correlation functions may be directly summed to yield the same result as adding the histograms prior to correlating.
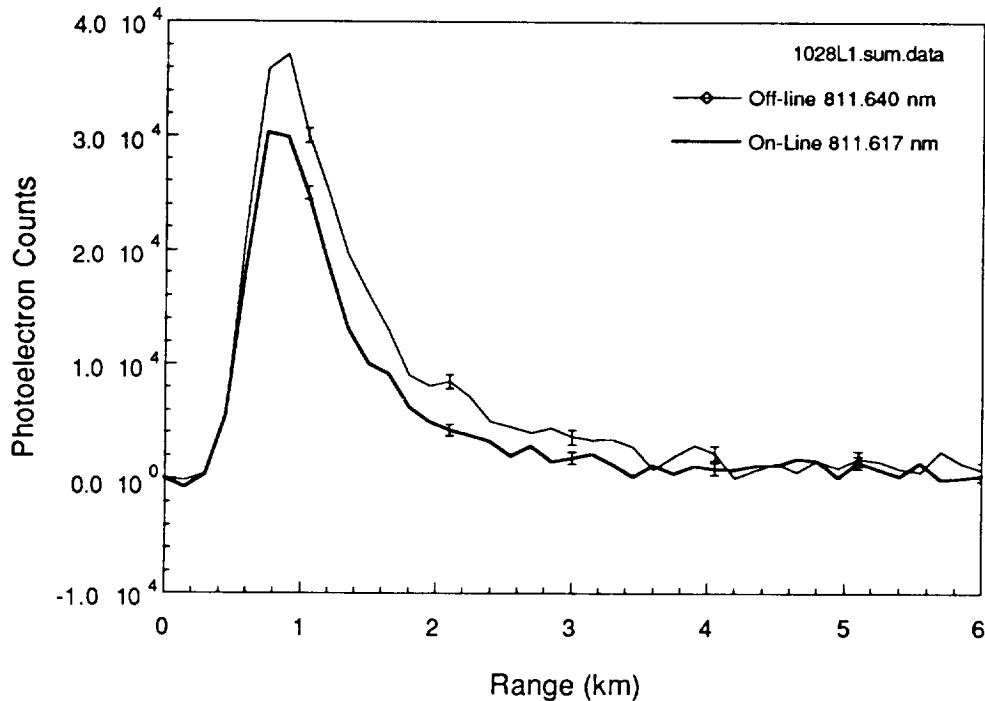


**Figure 52.** On-line and off-line range resolved water vapor lidar measurements. Each lidar profile is the sum of 12 one minute integrations.

In Figure 53, the lidar data from Figure 52 has been range corrected and plotted on a logarithmic scale. The range correction involves multiplying the photoelectron count in each range bin by the square of the distance from the receiver. If the dominant signal loss factor of the off-line signal is the $1/R^2$ losses then the slope of the off-line signal should then be very nearly zero. Since the dominant attenuation of the on-line signal is due to $1/R^2$ losses and absorption by water vapor then the on-line signal should have a nearly constant negative slope, which is evident in the figure.
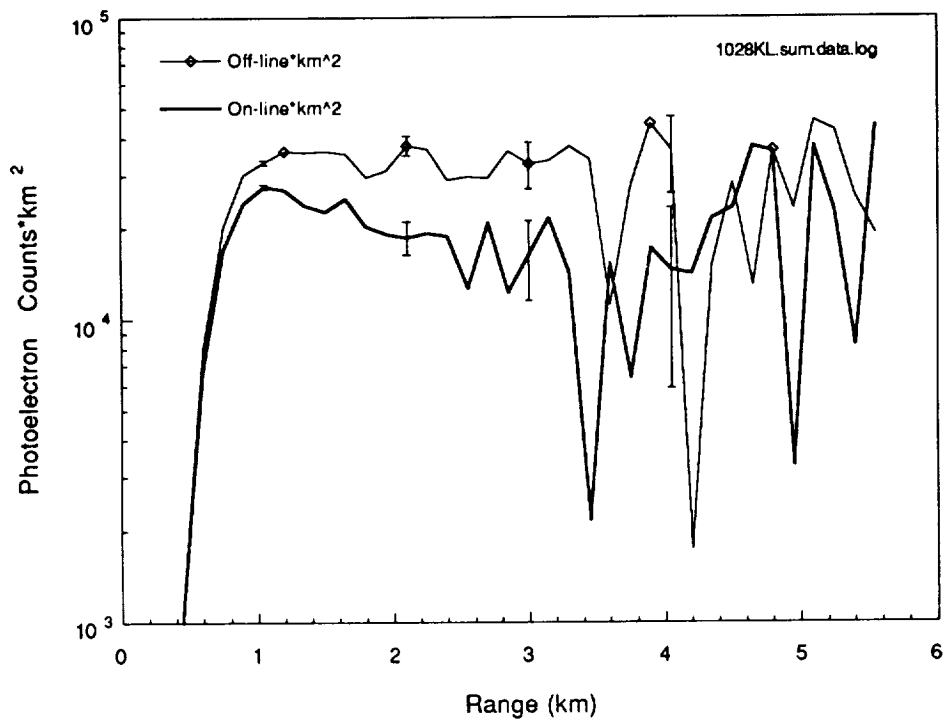


Figure 53. Horizontal path water vapor DIAL data, from Figure 52, range corrected and plotted on a logarithmic scale. Integration time was 12 minutes.

It should be noted that the error bars which previously were constant in size have also been multiplied by the square of the range.

120

Water vapor lidar data was taken on the night of November 4, 1993 and is shown in Figure 54. This data has also been range corrected. System parameters for these measurements are listed in Table 18.
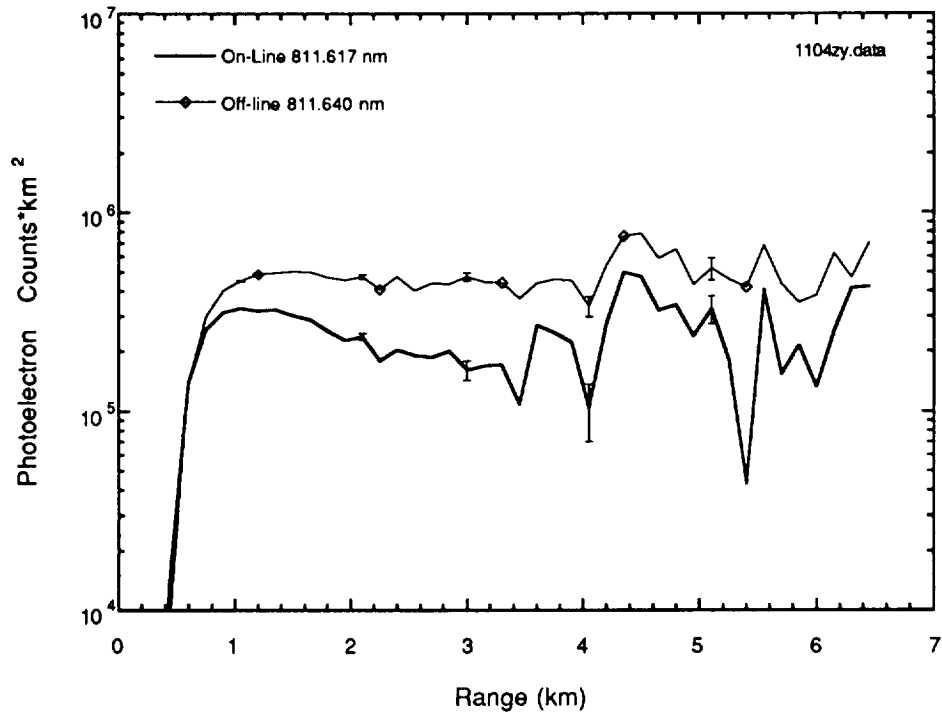


**Figure 54.** Horizontal path water vapor DIAL data, range corrected and plotted on a logarithmic scale. Integration time was 11 minutes.

**Table 18**

System parameters for lidar measurements shown in Figure 54.

| | |
|---|---|
| Avg. laser power | 20 mW |
| PN code length | 255 bits |
| On-line count rate | 6.2 Kcounts/sec |
| Off-line count rate | 9.0 Kcounts/sec |
| Background count rate | 80 counts/sec |
| Transmitter divergence | $\leq$ 100 urad |
| Receiver FOV | 160 urad |
| Bit rate | 1 MHz |
| Integration time | 11 minutes |

The higher SNR in Figure 54, seen as smaller error bars, is due to an improvement in the receiver optical alignment between the data taken on October 28 and November 4, 1993. This improvement resulted in more than an order of magnitude increase in signal count rate. Figure 55 shows range-resolved water vapor DIAL measurements taken on the night of November 10, 1993. Each on-line and off-line measurement was integrated for 20 minutes with the lidar pointed 2-3° above the horizon. The data has been range corrected. The system parameters for these measurements are listed in Table 19.

**Table 19**

System parameters for water vapor lidar measurements shown in Figures 55 & 56.

| | |
|---|---|
| Avg. laser power | 25 mW |
| PN code length | 1023 bits |
| On-line count rate | 7.4 Kcounts/sec |
| Off-line count rate | 10.0 Kcounts/sec |
| Background count rate | 150 counts/sec |
| Transmitter divergence | $\leq$ 100 urad |
| Receiver FOV | 160 urad |
| Bit rate | 1 MHz |
| Integration time | 20 minutes |

A lidar measurement through the boundary layer should experience a nearly constant extinction coefficient. This should yield a constant slope when range corrected and plotted on a logarithmic scale, which is evident in the figure.
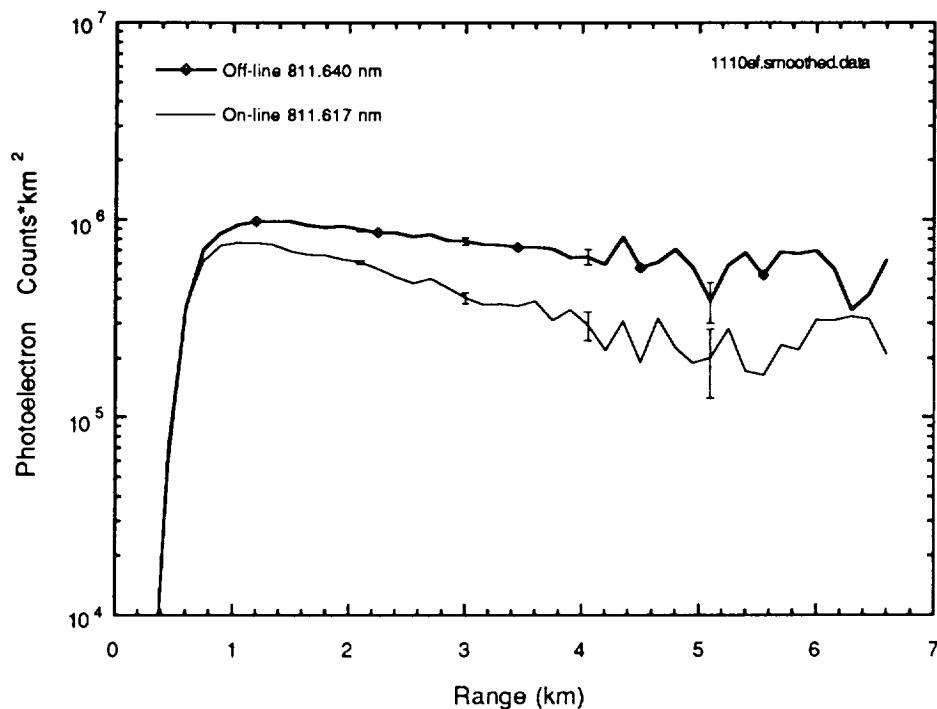
**Figure 55.** Horizontal path, range-resolved DIAL measurements of atmospheric water vapor made on the night of 11/10/93. Integration time was 20 minutes for each profile.

The water vapor absorption coefficient was estimated from the slopes of the on-line and off-line measurements in Figure 54 to be $0.109\,km^{-1}$. At the time of the lidar measurement, the mean surface pressure was 1025 mb and the vapor pressure was 5.41 mb. This vapor pressure corresponds to a water vapor number density of $1.37 \times 10^{17}\,molecules\,/\,cm^3$. The calculated absorption coefficient for the 811.617 nm absorption line, using this number density, is $0.132\,km^{-1}$. The lidar measurement is 17.4% lower than the calculated which is likely due to the same error sources listed in section 5.3. These error sources are addressed in section 5.5.

Estimates of range-resolved water vapor number density can be made by applying the DIAL equation Eq. (6) to the data shown in Figure 55. However, the data is

123

somewhat noisy so a two-bin (300 m resolution) running average has been performed

and the data plotted in Figure 56.
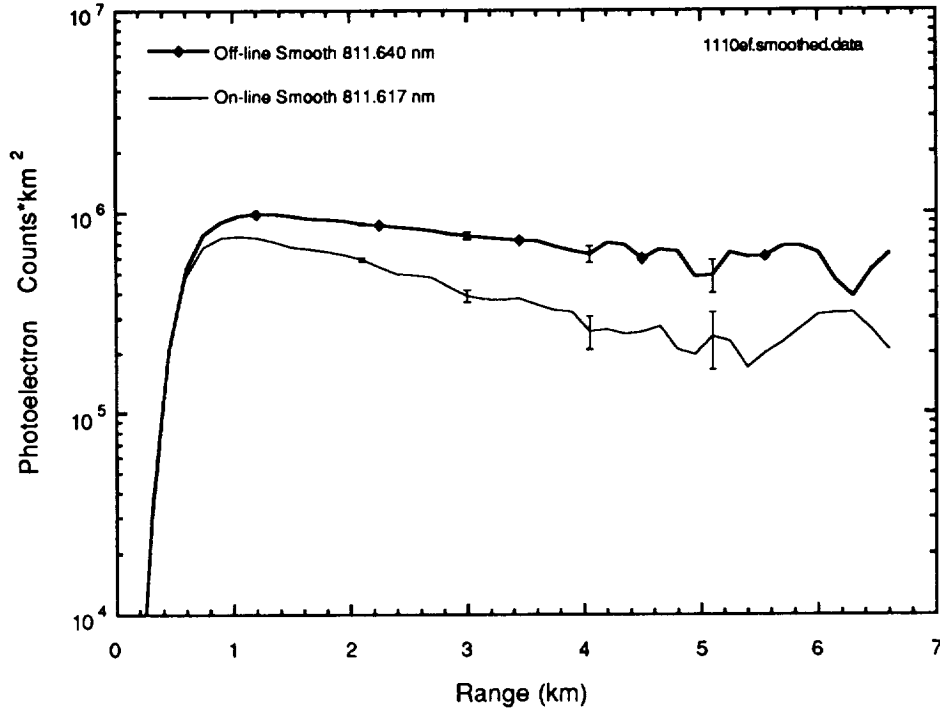


**Figure 56.** Water vapor DIAL data from 11/10/93 (Figure 55) smoothed in range with a two-bin running average. Range resolution = 300 m.

The range resolved water vapor number density can be estimated by using the DIAL

equation,

$$n(\Delta R) \cong \frac{1}{2\Delta\sigma\Delta R}\ln\left[\frac{N_{on}(R_1)N_{off}(R_2)}{N_{on}(R_2)N_{off}(R_1)}\right],$$

(104)

where $\Delta\sigma = 9.659 \times 10^{-24} cm^2 / molecules$ and $\Delta R = 300m$. Applying Eq. (104) to the

lidar data in Figure 56 yields an estimate of the range-resolved number density of water

molecules in the atmospheric path. The zero and negative values of $n(\Delta R)$ prevent the

data from being plotted on a log axis. Since zero and negative values of atmospheric water vapor number density are not realistic they have been dropped and the remaining data plotted in Figure 57. Missing data has been interpolated. The mean water vapor density over the atmospheric path, calculated from all data points including negative and zero values, is $0.48 \times 10^{17} molecules / cm^3$. This average water vapor density may be taken as the lower bound. The mean water vapor density calculated with only the positive values of $n(\Delta R)$ yields $1.49 \times 10^{17} molecules / cm^3$, which may be taken as the upper bound.
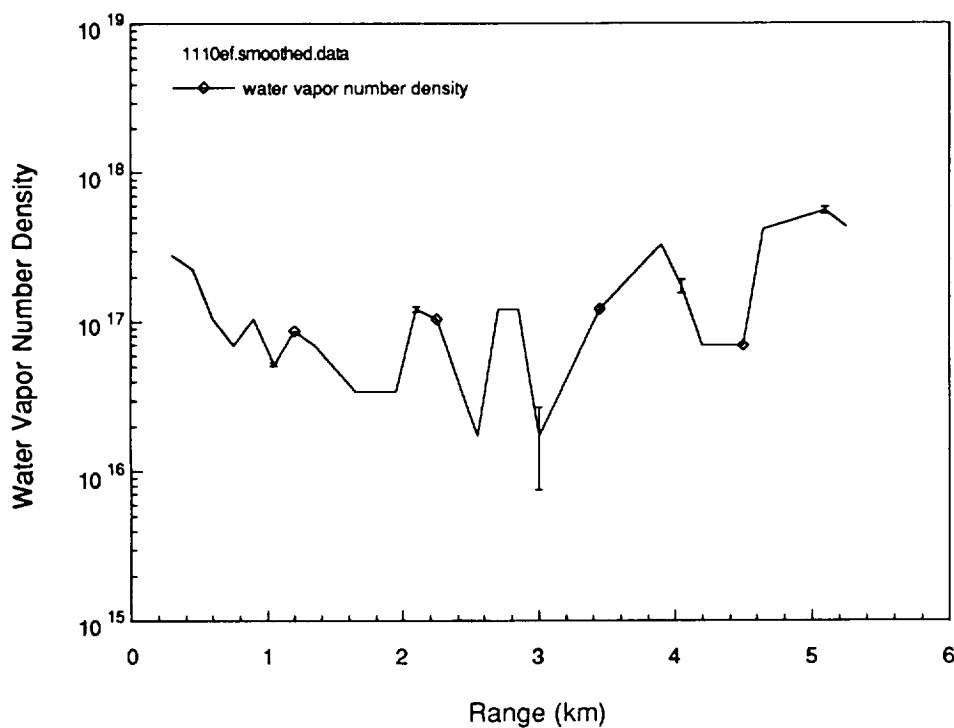


**Figure 57.** Range-resolved water vapor number density estimated from lidar measurements made on 11/10/93. Negative and zero values of water vapor density have been dropped. Trace connecting data points interpolates between dropped data points.

125

Further smoothing of the lidar data should eliminate the zero and negative values of $n(\Delta R)$ at the expense of range information. As the number of bins added together increases, the estimated water vapor density should approach the mean absorption coefficient calculated by fitting a line to the same data. The mean absorption coefficient was estimated to be $0.109 km^{-1}$. This absorption coefficient corresponds to a mean water vapor number density of $1.13 \times 10^{17} molecules / cm^3$ or a mixing ratio of $2.73 g / kg$.

At the time of the water vapor DIAL measurement, the water vapor mixing ratio, measured at BWI Airport, was reported to be $3.47 g / kg$ which corresponds to a number density of $1.37 \times 10^{17} molecules / cm^3$. The lidar underestimated the water vapor mixing ratio by 21% when compared with the humidity measurements reported by BWI.

### 5.5 Summary of water vapor DIAL measurements

The results of the water vapor DIAL measurements have been tabulated and are listed in Table 20. Columns 2 & 3 present the water vapor absorption coefficient calculated from the mean surface pressure and vapor pressure as reported by Baltimore Washington International Airport and Andrews Air Force Base (ADW). Column 4 shows the water vapor absorption coefficient estimated from the AlGaAs lidar measurements. Column 5 shows the difference between the measured and calculated values of the water vapor absorption coefficient. The arrows indicate whether the lidar estimate was higher ($\Uparrow$) or lower ($\Downarrow$) than the reported values. With only two exceptions, the AlGaAs lidar measured a lower water vapor absorption coefficient than was reported by BWI or ADW. The errors which would cause the AlGaAs lidar to underestimate the water vapor absorption coefficient are addressed in Section 5.6.

## Table 20

Summary of water vapor lidar measurements made from 10/28/93 to 11/10/93. The "*" denotes intermittent rain showers during the measurements.

| Date | BWI (km⁻¹) | ADW (km⁻¹) | AlGaAs Lidar Estimate (km⁻¹) | Difference($\Downarrow$ or $\Uparrow$) BWI/ADW |
|------|------------|------------|------------------------------|------------------------------------------------|
| 11/10/93 | 0.145 | 0.139 | 0.129 integrated path | 11% / 7% ($\Downarrow$) |
| | 0.138 | 0.133 | 0.110 range resolved | 20% / 17% ($\Downarrow$) |
| 11/09/93 | 0.143 | 0.150 | 0.156 range resolved | 9% / 4% ($\Uparrow$) |
| | 0.143 | 0.170 | 0.125 integrated path | 13% / 26% ($\Downarrow$) |
| 11/08/93 | 0.149 | 0.132 | 0.129 range resolved | 13% / 2% ($\Downarrow$) |
| | 0.138 | 0.126 | 0.137 range resolved | 1% / 9% ($\Downarrow\Uparrow$) |
| | 0.143 | 0.132 | 0.115 range resolved | 19% / 13% ($\Downarrow$) |
| 11/04/93* | 0.263 | 0.245 | 0.167 range resolved | 36% / 31% ($\Downarrow$) |
| 11/02/93 | 0.150 | 0.143 | 0.079 range resolved | 47% / 44% ($\Downarrow$) |
| 10/28/93 | 0.158 | 0.119 | 0.113 range resolved | 28% / 5% ($\Downarrow$) |

## 5.6 Error analysis

Both the integrated path and range resolved DIAL measurements made with the AlGaAs lidar underestimated the water vapor absorption coefficient and the water vapor number density. Since there is a significant distance between BWI and GSFC it is not unusual for there to be a discrepancy between the measured and estimated water vapor density. However, if the discrepancy were solely due to the spatial variation of water vapor in the atmosphere (*i.e.* no instrument or measurement technique effects), one would expect the lidar measurements to return with equal likelihood both higher and lower absorption coefficients compared with the meteorological reports. Over the period of water vapor measurements, Oct. 28 through Nov. 10, the AlGaAs lidar consistently measured lower absorption coefficients than were reported at either Baltimore

Washington International Airport or Andrews Air Force Base. This implies a bias in the instrument or measurement technique which must be dealt with as an error source.

There are two known error sources in the present DIAL technique which result in an underestimation of the absorption coefficient. They are (1) the manual zeroing of the lockin amplifier to the center of the absorption line and (2) the wavelength detuning effects of the dither current to the laser.

The offset error induced by manually zeroing the lockin amplifier may be estimated by from Figures 61 and 62. This error may be represented as the ratio of short term lockin voltage fluctuations to the first derivative amplitude. From Figure 62, the maximum change in lockin voltage between two consecutive data points is approximately 1 mV. The amplitude of the first derivative, from Figure 61, is ~ 17 mV. This ratio is

$$\frac{1mV}{17mV} = 0.058 \tag{105}$$

which implies an offset error of 0.058 times the Doppler linewidth. The slope of line center of the first derivative curve, Figure 61, is

$$\frac{17mV}{0.7mA} = 24.3mV / mA. \tag{106}$$

The estimated offset error of ~1 mV pp corresponds to $(1mV)/(24.3mV / mA) = 0.04 \, mA$ which translates to a wavelength fluctuation of

$$(0.04mA) \cdot (3.3pm / mA) = 0.13 \, pm, \tag{107}$$

128

or approximately one-tenth of a linewidth, which corresponds to less than 2% change in the absorption coefficient.

The most significant error source is the wavelength detuning effect of the 0.8 mA dither current used to frequency lock the laser to the water vapor absorption line. By scanning the laser wavelength sinusoidally across the center of the absorption line, the laser experiences a lower effective absorption coefficient. This results in the AlGaAs lidar underestimating the water vapor absorption coefficient and, hence, the water vapor number density.

By calculating this effective absorption coefficient, this error may be estimated and subsequently corrected for in the data. The effective, *i.e.* time averaged, absorption coefficient can be estimated by integrating the product of the Lorentz absorption line shape with the probability density of the sinusoidal wavelength dither signal. The Lorentz line shape is described by the equation,

$$k_{H_2O} = \frac{S}{\pi} \cdot \frac{\gamma/2}{(v - v_o)^2 + (\gamma/2)^2},$$
(108)

where $S$ is absorption transition strength, $\gamma$ is the absorption linewidth, and $v$ is the frequency. Figure 58 shows a plot of the normalized Lorentz linewidth with a halfwidth equal to unity and line center $v_o = 0$.
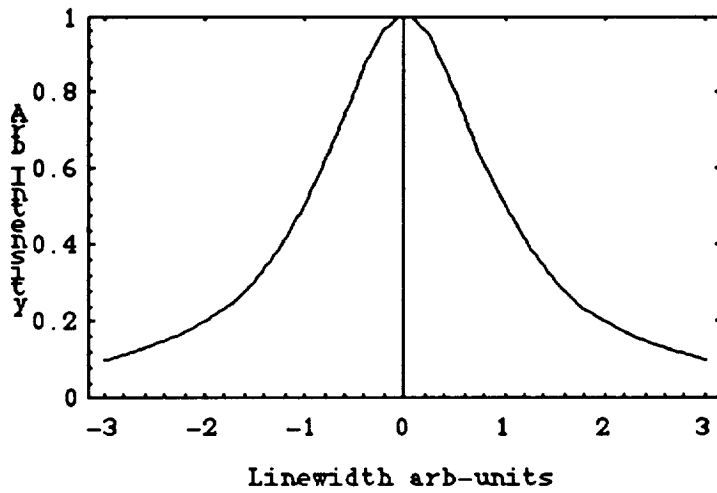
**Figure 58.** Plot of Lorentz lineshape with halfwidth $\alpha = 1$.

The probability density of a sine wave amplitude with peak amplitude 0.5 is given by[64]

$$p(v) = \begin{cases} \dfrac{1}{\pi \cdot \sqrt{(0.5)^2 - v^2}} & |v| < 0.5 \\ 0 & |v| \geq 0.5 \end{cases}, \tag{109}$$

and is shown in Figure 59.
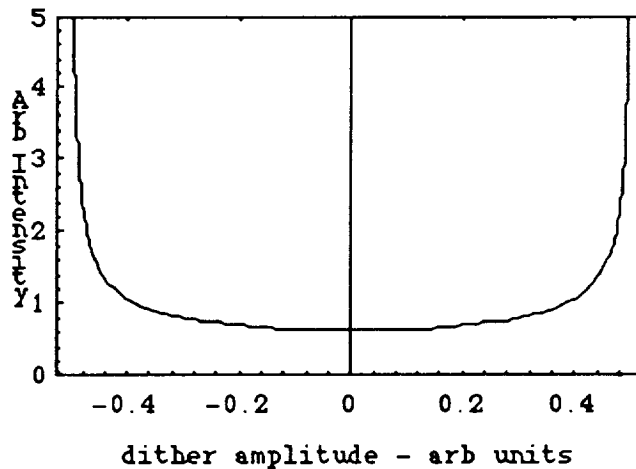


**Figure 59.** Plot of probability density of sine function amplitude with amplitude = 0.5.

130

Numerical integration of the probability density function over the interval,

$-0.5 < v < 0.5$, approaches unity as the limits approach $\pm0.5$. The time averaged

absorption coefficient $\overline{\sigma}(v)$ is the integral of the product of the normalized linewidth and

probability density is represented as

$$\overline{\sigma}(v) = \frac{1}{\pi} \int_{>-0.5}^{<+0.5} \left[ \frac{1}{v^2 + 1} \right] \cdot \left[ \frac{1}{\sqrt{0.25 - v^2}} \right] dv. \tag{110}$$

For the above values, numerical integration of Eq (110) yields a value of 0.89. This

implies that the absorption coefficient, estimated from the lidar data, will be

underestimated by ~11% when the laser is dithered with an amplitude of one-half the

linewidth. Figure 60 shows the normalized absorption coefficient as a function of dither

amplitude. As expected, the absorption coefficient is unity for zero dither amplitude and

decreases as the dither amplitude increases. As the dither amplitude grows to many

times the linewidth, the absorption coefficient asymptotically approaches zero.
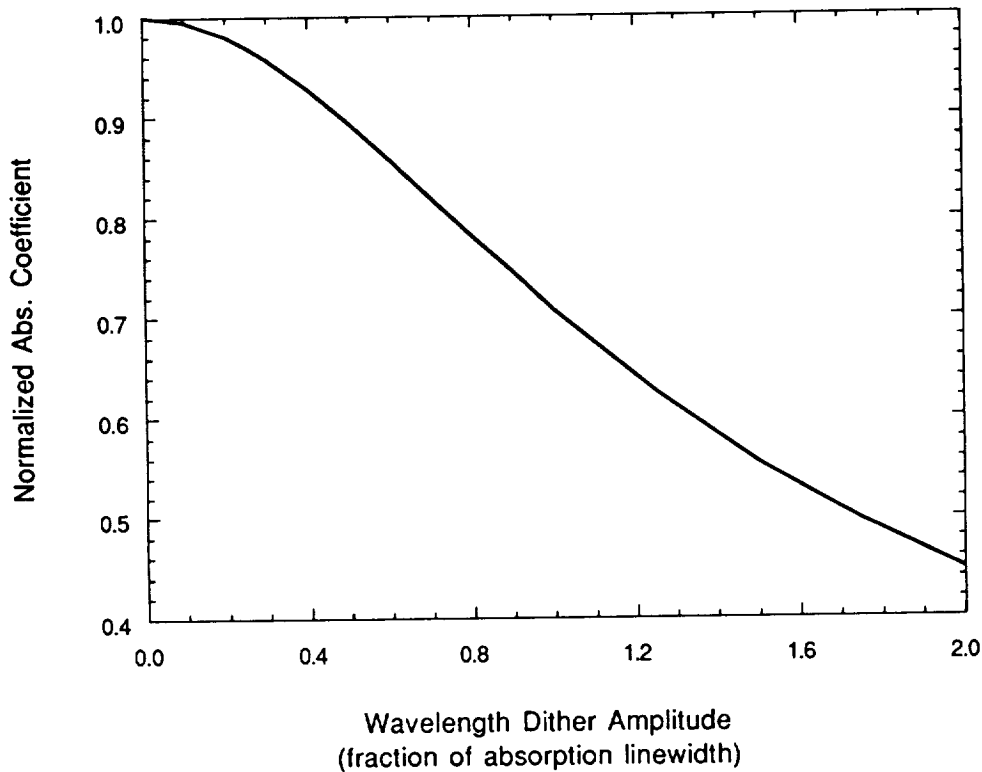
**Figure 60.** Normalized effective absorption coefficient vs wavelength dither amplitude. The peak dither wavelength is given as a fraction of absorption linewidth.

The applied dither current was typically $(40mV)/(50\Omega) = 0.8mA$. This current corresponds to a peak wavelength dither of $(0.8mA)\cdot(3.3pm/mA) = 2.64pm$ or $\pm1.32pm$. The Lorentz or pressure broadened linewidth of the 811.617 nm absorption line is $10.98pm$. This implies that the dither amplitude was approximately one-quarter of the linewidth. Calculating the integral in Eq (110) with a dither amplitude of 0.25 yields a value for the normalized absorption coefficient of 0.97. This implies that the water vapor coefficients, and subsequently the water vapor number densities, estimated in sections 5.3 and 5.4 should be underestimated by ~3%.

132

Fluctuations in the wavelength of the laser represent another error source in the DIAL measurements. As the laser drifts away from the center of the absorption line, the laser will experience a reduced absorption coefficient which will result in an underestimation of the water vapor number density. The laser wavelength stability can be estimated by taking a ratio of the peak-to-peak excursions of the lockin error voltage and the peak-to-peak amplitude of the first derivative curve of the 811.617 nm absorption line. Figure 61 shows a first derivative scan of the absorption line at 811.617 nm made with the absorption cell and AlGaAs lidar transmitter laser. The scan was made in an absorption cell with a 10 m path length which was evacuated and backfilled with ~26 Torr of water vapor. The first derivative curve of the water vapor absorption line is centered at 92.9 mA bias current and the linewidth is ~0.7 mA. This linewidth corresponds to $2.3\,pm$ or $0.035\,cm^{-1}$ (FWHM). The halfwidth, $0.017\,cm^{-1}$, agrees with the Doppler halfwidth calculated in Eq (92).

The fluctuations surrounding the first derivative curve in Figure 61 may be attributed to an etalon effect created in the absorption cell. The curve in Figure 61 represents the sum of the etalon effect and the first derivative absorption signal at 811.617 nm. Although the laser is stabilized to the absorption line at 811.617 nm, Figure 62, the etalon effect could cause an offset error of the laser center wavelength which would lead to an error in estimating the water vapor absorption coefficient.

The peak to peak excursion of the first derivative curve in Figure 61 is 17 mV. A scan of lockin error signal and laser wavelength, made during the water vapor DIAL measurements (Figure 55, data set 1110ef), is shown in Figure 62. The top trace shows the laser wavelength during the lidar measurement. The bottom trace is the

lockin error voltage and shows a peak to peak excursion of 3 mV. The ratio of lockin

error voltage to the first derivative amplitude is

$$\frac{3mV}{17mV} = 0.17.$$ (111)
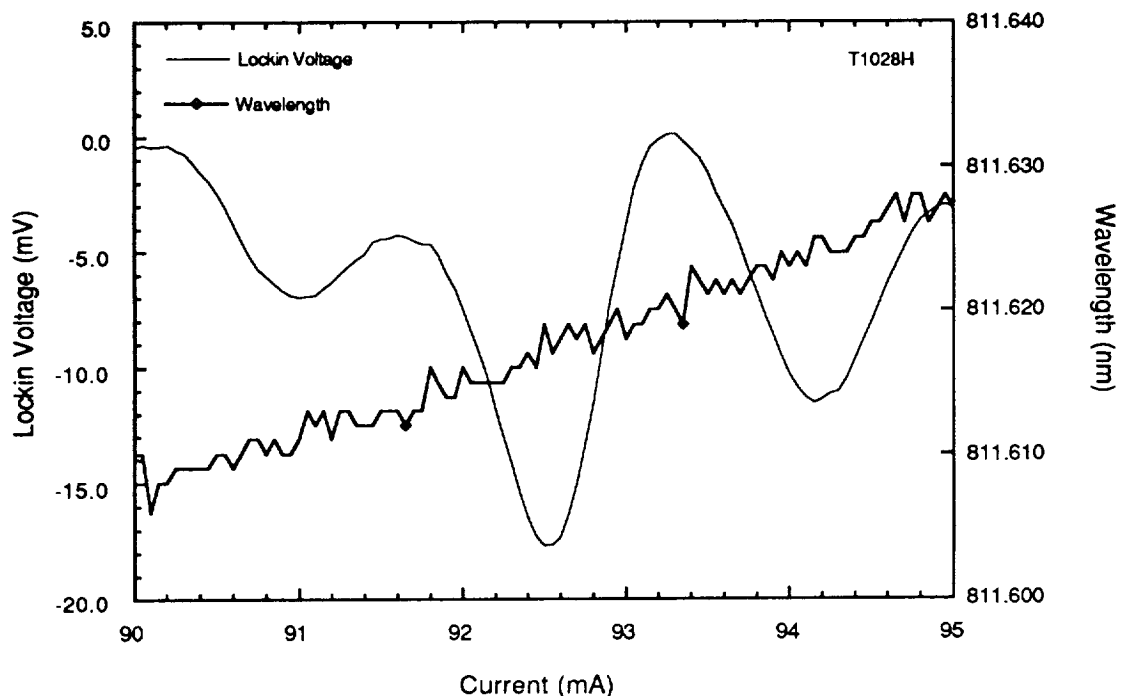


**Figure 61.** First derivative scan of 811.617 nm water vapor absorption line.

This ratio implies that the laser fluctuated less than one-fifth of the absorption

linewidth during the DIAL measurement. The slope of line center of the first derivative

curve, Figure 61, is $24.3mV / mA$. The laser fluctuated ~3 mV pp during the water

vapor DIAL measurement, which corresponds to $(3mV)/(24.3mV / mA) = 0.123mA$.

This translates to a wavelength fluctuation of

$$(0.123mA) \cdot (3.3pm / mA) = 0.4 \ pm.$$ (112)

Therefore the laser center wavelength fluctuated $0.4\,pm/2.3\,pm$, or 0.17 of the

absorption linewidth, which is in agreement with the stability estimate from Eq (111).
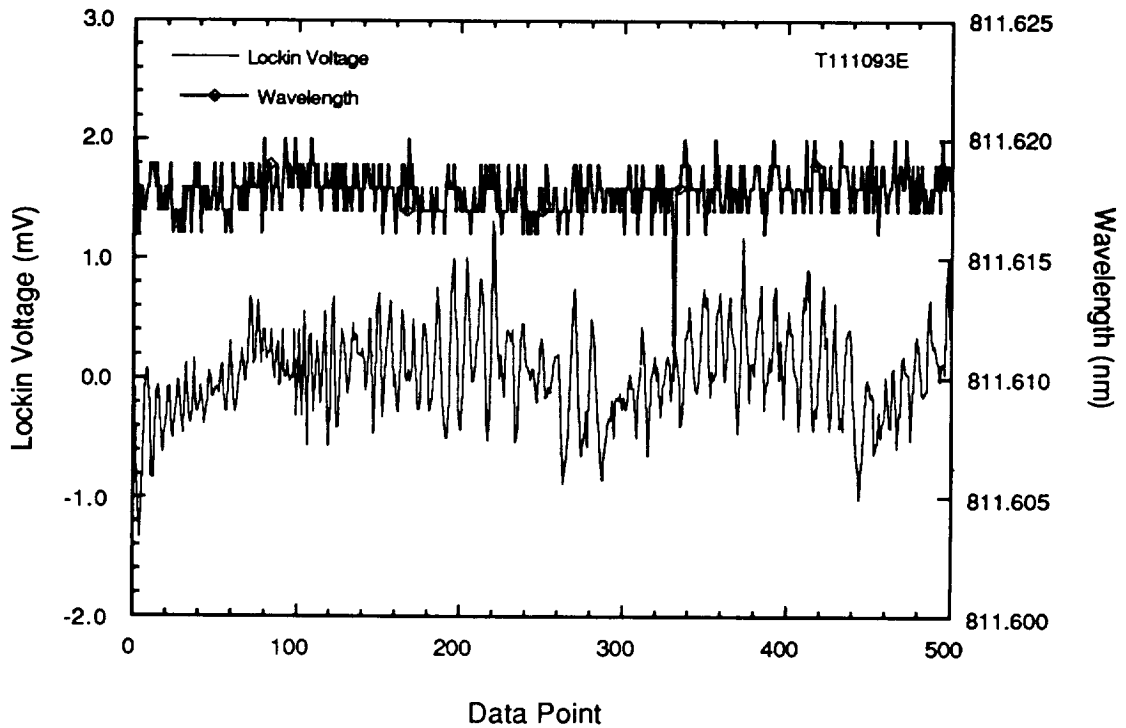


**Figure 62.** Frequency stability of AlGaAs laser during on-line water vapor lidar measurement of 11/10/93. Top trace is wavelength and bottom trace is lockin error voltage.

It is important to note that the Doppler width of the absorption line at 811.617

nm is approximately one-fifth of the Lorentz or pressure broadened linewidth,

$(0.0177\,cm^{-1})/(0.0837\,cm^{-1}) = 0.21$. The laser center wavelength was stable to better

than one-fifth of the Doppler width, therefore, with respect to the Lorentz linewidth,

the laser was stable to $(0.2)\cdot(0.2)$ or 0.04 times the Lorentz linewidth. The absorption

coefficient, Eq (108), can be calculated for a laser frequency drift from line center of

0.04, *i.e.* $(v-v_o)^2 = 0.0016$. The resultant absorption coefficient is 0.998 the value at line center, implying a DIAL measurement error of approximately 0.16%.

A summary of error sources and the estimated error in the absorption coefficient is presented in Table 21.

**Table 21**

Summary of error sources in AlGaAs water vapor DIAL measurements and magnitudes of these errors in estimates of the water vapor absorption coefficient.

| Error Source | Estimated error to absorption coefficient |
|---|---|
| Physical Separation of lidar and ground truth humidity measurements | ~0-40% |
| Dither current induced wavelength variation ~0.3 linewidth | ~3-5% |
| Manual zeroing of lockin amplifier ~0.25 linewidth from linecenter | <2% |
| Drift of laser center wavelength <0.04 of Lorentz linewidth | <<1% |
| Interference from neighboring lines | ~0.2% |

# 6. SUMMARY AND CONCLUSIONS

Single color lidar measurements over horizontal paths to terrestrial targets were made at night. Horizontal path measurements to a water tower at 5 km were used to check and optimize the alignment of the lidar transmitter with the receiver and to compare the operation of the lidar system with theory via the single scattering lidar equation. Calculated performance agreed with experimental to within a factor of two which is reasonable considering the accuracy of assumed values for the target reflectivity and the total atmospheric attenuation coefficient.

Nighttime cloud and aerosol lidar measurements were made over near vertical paths. Rayleigh backscatter was visible in 20 minute lidar measurements to an altitude of approximately 9 km. Thin cirrus clouds at 10 and 13 km altitudes were profiled with an average laser power of 35 mW and an integration time of 20 minutes.

The cloud and aerosol lidar measurements made in these experiments represent a significant increase in measurement range and accuracy compared to previous measurements reported with PN code AlGaAs lidar systems.

DIAL measurements of atmospheric water vapor have been made for the first time using a PN code modulated AlGaAs laser. An external EO modulator was used to impress the PN code onto the laser diode beam. Integrated path measurements were made to a terrestrial target over a one-way path length of ~5 km. The estimated water vapor absorption coefficient agreed to within 6.5% of the measured humidity reported by Baltimore Washington International Airport at the time of the lidar measurement.

Range resolved DIAL measurements of water vapor were made over a 4 km horizontal path. The estimated mean water vapor coefficient from these measurements agreed to within 20% of the measured humidity. The humidity values used to compare with both integrated path and range resolved water vapor lidar estimates were removed from the lidar system by approximately 30 km.

Error sources in the DIAL measurements were identified and quantified where possible. The 30 km separation of the lidar system and meteorological station represents an indeterminate error. This error source may be reduced by making humidity measurements at the location of the lidar. The wavelength stability of the AlGaAs laser was measured and the resulting DIAL measurement error due to laser drift was estimated to be less the 0.2%. The most significant error source was the dither current used to frequency lock the AlGaAs laser to the water vapor absorption line. This error was a function of the dither amplitude. The resulting error ranged from 3% for a dither amplitude equal to one-quarter of the absorption linewidth to 60% for a dither amplitude equal to the full linewidth. However, this was a systematic error which, once quantified can be removed from the data by applying a multiplicative correction factor.

The DIAL measurements of water vapor are the first reported measurements of atmospheric water vapor using a compact lidar based on PN code modulated AlGaAs lasers.

## 6.1 Future work

Work is underway to replace the AlGaAs laser transmitter with a 1 Watt CW master oscillator-power amplifier (MOPA) device. This could potentially eliminate the

138

need for the external EO modulator by permitting current modulation of the power amplifier section of the MOPA device. This depends on whether modulating the power amplifier effects the spectral properties, *i.e.* linewidth and center frequency, of the master oscillator. The master oscillator would be frequency locked to a water vapor absorption line.

The optical bandpass filter currently used in the lidar receiver (810 nm center wavelength, 5 nm FWHM) will be replaced with a custom optical bandpass filter with <0.1 nm bandwidth. This should permit daytime operation of the AlGaAs lidar.

An improved histogramming circuit has been designed and will be implemented on a custom printed circuit board. This new histogramming circuit will eliminate measurement errors due to the existing histogrammer.

Improved opto-mechanical design of the lidar system should result in a more compact lidar and better alignment stability. Also, improvements to the thermal design of the laser diode header are needed to reduce temperature induced fluctuations of the laser diode wavelength. This should also improve the frequency locking of the AlGaAs laser to water vapor lines.

An improved frequency locking algorithm is being developed. This will incorporate a true proportional-integral-derivative (PID) feedback loop which should improve both the short term, < 1 minute, and long term, ~1 hour, frequency stability. Also, techniques will be investigated to permit simultaneous on-line and off-line DIAL measurements. It is not clear at this time whether a single laser, frequency hopping between the on-line and off-line wavelengths, is simpler than two separate laser transmitters, orthogonally polarized, operating at the on-line and off-line wavelengths

simultaneously. This latter technique would require two photon count detectors and a polarization beam splitter in the receiver path.

The multipass absorption cell will be investigated and the etalon effect minimized or eliminated. The frequency locking technique used to stabilize the laser to water vapor absorption lines is susceptible to this etalon effect. Improved frequency locking to more lines, and weaker lines, should be realized with elimination of the etalon effect.

A prototype AlGaAs altimeter will be assembled and tested. The AlGaAs altimeter will use a single element, 150 mW CW AlGaAs laser modulated with a 2047 bit PN code at >100 MHz. The range resolution will be less than 1.5 meters. This prototype altimeter could be flown on a NASA aircraft and compared with existing laser altimeter instruments.

## REFERENCES

1. D. O'C. Starr and S. H. Melfi, "The Role of Water Vapor in Climate," NASA Conference Publication 3120, (1991).

2. U.S. Weather Bureau, Radiosonde Observations, Federal Meteorological Handbook #3, (U.S. Dept. of Commerce, U.S. Dept. of Defense 1969).

3. World Meteorological Organization, Guide to Meteorological Instrument and Observing Practices, 4th Ed. (Secretariat WMO 1971).

4. W.P. Menzel (Editor), "1ST International TOVS Study Conference-Technical Proceedings, Igls, Austria, Aug. 29-Sept. 2, 1983.

5. Amer. Meteoro. Soc.,"2ND Conference on Satellite Meteorology/Remote Sensing and Applications," Amer. Meteoro. Soc. Williamsburg, VA, May 13-16, 1986.

6. H. D. Chang, P. H. Hwang, T. T. Wilheit, and T. C. Chang, "Monthly Distributions of Precipitable Water from Nimbus 7 SMMR Data," J. Geophys. Res., 89 (D4) 5328-5334, (1984).

7. S. H. Melfi, J. D. Lawrence, and M. P. McCormick, "Observation of Raman scattering by water vapor in the atmosphere, " Appl. Phys. Lett. 15(9), 295-297 (1969).

8. J. A. Cooney, "Remote measurements of atmospheric water vapor profiles using the Raman component of laser backscatter," J. Appl. Meteorol., 9(1), 182-184 (1970).

9. R. G. Strauch, V. E. Derr, and R. E. Cupp, "Atmospheric water vapor measurement by Raman lidar," Rem. Sens. Environ. 2(2), 101-108 (1972).

10. W. Grant, "Differential absorption and Raman lidar for water vapor profile measurements: a review," Optical Engineering, 30(1) pp 40-48 (1991).

11. LOWTRAN, Air Force Geophysics Laboratory.

12. G. Herzberg, Molecular Spectra and Molecular Structure, II, Infrared and Raman Spectra of Polyatomic Molecules, Van Nostrand Reinhold Company Inc. pg 106, 1945.

13. T. D. Wilkerson and J. Brasseur, "Proposed $H_2O$ line list for measurements of strength and width: $\lambda$ =7147-7321 Å," U. Maryland Technical Note BN-846 (Nov. 1976).

14. T. D. Wilkerson, G. Schwemmer, B. Gentry, and L. P. Giver, "Intensities and $N_2$ collision broadening coefficients measured for selected $H_2O$ absorption lines between 715 and 732 nm, " J. Quant. Spectosc. Radiat. Transfer **22**(4), 315-331 (1979).

15. J. Y. Mandin, J. P. Chevillard, C. Camy-Peyret, J. M. Flaud, and J. W. Brault, "High resolution spectrum of water vapor between 13200 and 16500 $cm^{-1}$," J. Molec. Spectrosc. **116**(1), 167-190 (1986).

16. B. E. Grossman and E. V. Browell, "Spectroscopy of water vapor in the 720 nm wavelength region: Line strengths, self-induced pressure broadenings and shifts, and temperature dependence of linewidths and shifts," J. Molec. Spectrosc. **136**(2), 264-294 (1989).

17. B. E. Grossman and E. V. Browell, "Water vapor line broadening and shifting by air, nitrogen, oxygen, and argon in the 720 nm wavelength region," J. Molec. Spectrosc. **138**(2), 562-595 (1989).

18. L. P. Giver, G. K. Schwemmer, B. Gentry, and T. D. Wilkerson, "Water absorption lines , 931-961 nm: Selected intensities, $N_2$ collision broadening coefficients, self broadening coefficients, and pressure shifts in air, " J. Quant. Spectrosc. Radiat. Transfer **27**(4), 423 (1982).

19. E. V. Browell, S. Ismail, and B. E. Grossman, "Temperature sensitivity of differential absorption lidar measurements of water vapor in the 720 nm region," Appl. Opt., in press.

20. C. B. Farmer,"The Strengths of H2O Lines in the 8200 Å Region and their Application to High Dispersion Spectra of Mars," Icarus. **15**, 190-196 (1971).

21. W. Baumann and R. Mecke, Z. Phys. **81** pg 445 (1933).

22. C. Cahen, G. Megie, and P. Flamant, "Lidar monitoring of water vapor cycle in the troposphere," J. Appl. Meteorol. **21**(10), 1506-1515 (1982).

23. P. Ponsardin, N. S. Higdon, B. E. Grossman, E. V. Browell, "Spectral control of an alexandrite laser for an airborne water vapor DIAL system," Appl. Opt. submitted.

24. R. M. Schotland, "Some observations of the vertical profile of water vapor by means of a ground based optical radar," in Proc. Fourth Symposium on Remote sensing of the Environment, pp 271-273, Univ. of Michigan (1966).

25. R. M. Measures, Laser Remote Sensing. Fundamentals and Applications, Wiley Interscience, New York (1984).

26. R.A. McClatchey, R.W. Fenn, J.E.A. Selby, F.E. Volz, and J.S. Garing, "Optical Properties of the Atmosphere, 3$^{rd}$ Edition," Air Force Cambridge Research Laboratories, AD-753 075, (N73-18412) 24 August 1972.

27. E. J. McCartney, _Optics of the Atmosphere_, Wiley, New York (1976).

28. S. Ismail, E.V. Browell, "Airborne and Spaceborne lidar measurements of water vapor profiles: A sensitivity analysis," Appl. Opt., **28**, 3603-3615, (1989).

29. E.V. Browell, N.S. Higdon, C.F. Butler, M.A. Fenn, B.E. Grossman, P. Ponsardin, W.B. Grant, and A.S. Bachmeirer, "Tropospheric water vapor measurements with an airborne lidar system," Preprints, Seventh Symposium on Meteoro. Obs. and Instr., American Meteorological Society, Boston, MA, 250-251, (1991).

30. M. P. McCormick (Editor), "Third International Lidar Research Directory," NASA Langley Research Center, February 1993.

31. H. Kressel and J. K. Butler, _Semiconductor Lasers and Heterojunction LEDs_, Academic Press, Orlando (1977).

32. R. C. Dixon, _Spread Spectrum Systems_, Wiley Interscience, New York, 1984.

33. N. Takeuchi, N. Sugimoto, H. Baba, and K. Sakurai, "Random modulation cw lidar," Appl. Opt. **22**, 1382 (1983).

34. N. Takeuchi, H. Baba, K. Sakurai, and T. Ueno, "Diode-laser random-modulation cw lidar," Appl. Opt. **25**, 63 (1986).

35. D. M. Norman and C. S. Gardner, "Satellite laser ranging using pseudonoise code modulated laser diodes," Appl. Opt. **27**, 3650 (1988).

36. J. B. Abshire, J. A. R. Rall, S. S. Manizade, "Altimetry and Lidar Using AlGaAs Lasers Modulated with Pseudo-Random Codes," 16th International Laser Radar Conference, NASA Conference Publication 3158 Part 2, pp 441, Boston, MA July 20-24, 1992.

37. J. A. R. Rall, J. B. Abshire, S. S. Manizade, "Lidar Measurements of Clouds and Aerosols Using AlGaAs Lasers Modulated with Pseudorandom Codes," IEEE Lasers and Electro-Optics Society 1992 Annual Meeting Conference Proceedings, Boston MA, November 16-19, 1992.

38. J. B. Abshire and J. A. R. Rall, "AlGaAs Lidar-Theory & Measurement," in _Optical Remote Sensing of the Atmosphere Technical Digest_, 1993 (Optical Society of America, Washington D.C., 1993), Vol 5, postdeadline papers.

39. Unknown, "Applications of pseudo-random sequences."

40. A. V. Oppenheimer, A. S. Willsky, & I. T. Young, _Signals and Systems_, Prentice-Hall signal processing series, 1983.

41. C. Nagasawa, M. Abo, H. Yamamoto, and O. Uchino, "Random modulation cw lidar using new random sequences," Appl. Opt. **29** (10) pp 1466-1470, April 1, 1990.

42. P. R. Bevington, Data Reduction and Error Analysis for the Physical Sciences, McGraw-Hill, Inc. 1969.

43. N. Sissenwine, "Humidity up to the Mesopause," Rept AFCRL-68-0550, Air Force Surveys in Geophysics No. 206. AFCRL, Bedford, MA (1968).

44. E. J. McCartney, Optics of the Atmosphere, Wiley, New York (1976).

45. S. Ismail and E. V. Browell, "Airborne and spaceborne lidar measurements of water vapor profiles: a sensitivity analysis," Appl. Opt., 28 17, (1989).

46. T. D. Wilkerson, G. Schwemmer, B. Gentry, L. P. Giver, "Intensities and $N_2$ Collision-Broadening Coefficients Measured for Selected $H_2O$ Absorption Lines Between 715 and 732 nm," J. Quant. Spectrosc. Radiant. Transfer, 22, pp 315-331, (1979).

47. B. E. Grossman and E. V. Browell, "Water Vapor Line Broadening and Shifting by Air, Nitrogen, Oxygen, and Argon in the 720-nm Wavelength Region," J. Mol. Spect., 138, pp 562-595, (1989).

48. R. M. Measures, Laser Remote Sensing. Fundamentals and Applications, Wiley Interscience, New York (1984).

49. P. W. Atkins, Molecular Quantum Mechanics, Oxford University Press, 2 Ed., New York (1983).

50. D. M. Gates, "Line Parameters and Computed Spectra for Water Vapor Bands at 2.7 $\mu$m," Washington, D.C., National Bureau od Standards, U.S. Govt. Printing Office, (1964).

51. R. A. McClatchey,W. S. Benedict, S. A. Clough, D. E. Burch, R. F. Calfee, K. Fox, L. S. Rothman, J. S. Garing, "AFCRL Atmospheric Absorption Line Parameters Compilation," AFCRL-TR-73-0096, 26 January, 1973.

52. L. P. Giver, B. Gentry, G. Schwemmer, T. D. Wilkerson, "Water Absorption Lines, 931-961 nm: Selected Intensities, $N_2$-Collision-Broadening, Self-Broadening Coefficients, and Pressure Shifts in Air," J. Quant. Spectrosc. Radiant. Transfer, 27, pp 423-436, (1982).

53. W. B. Grant, "Differential absorption and Raman lidar for water vapor profile measurements: a review," Opt. Eng., 30 (1), pp 40-48, (1991).

54. R. A. McClatchey, R. W. Fenn, J. E. A. Selby, F. E. Volz, J. S. Garing, "Optical Properties of the Atmosphere (Third Edition)," AFCRL-72-0497, Environmental Research Papers, No. 411, 24 August, 1972.

55. K. Nakagawa and T. Shimizu, "Highly Sensitive Spectrometer with 0.78 $\mu$m AlGaAs Diode Lasers, Jpn. J. Appl. Phys. 26, L1697-L1700 (1987).

56. N. Goldstein, S. Adler-Golden, J. Lee, and F. Bien, "Measurement of molecular concentrations and line parameters using line-locked second harmonic spectroscopy with an AlGaAs diode laser," Appl. Opt. **31** 18, (1992).

57. J. Reid & D. Labrie, "Second-Harmonic Detection with Tunable Diode Lasers-Comparison of Experiment and Theory," Appl. Phys. B. **26**, pp 203-210 (1981).

58. H. Tsuchida, S. Sanpei, M. Ohtsu, and T. Tako, "Frequency Stability Measurement of Feedback Stabilized AlGaAs DH Laser," Jpn. J. Appl. Phys. **19** 12, L721-L724 (1980).

59. M. Ohtsu and S. Kotajima, "Linewidth Reduction of a Semiconductor Laser by Electrical Feedback," IEEE J. Quantum Elec. **QE-21**(12) 1905-1912, (1985).

60. J. A. R. Rall and P. L. Spadin, "Optomechanical design of the grating laser beam combiner (GLBC) laser diode header," SPIE Proc. Vol. 1044, pg. 74 (1989).

61. Data Sheet, RCA Electro Optics/EG&G Optoelectronics SPCM-200-PQ, EG&G Canada, Ltd.

62. Handbook of Chemistry and Physics, CRC Press, Inc., 59th edition, ppE362, 1978-1979.

63. J. Spinhirne, computer model of atmospheric scattering and attenuation, personal communication, Dec. 21, 1993.

64. K. Miller, Engineering Mathematics, Rinehart & Company, New York, 1957, pg 328.

# REPORT DOCUMENTATION PAGE

Public reporting burden for this collection of information is estimated to average 1 hour per response, including the time for reviewing instructions, searching existing data sources, gathering and maintaining the data needed, and completing and reviewing the collection of information. Send comments regarding this burden estimate or any other aspect of this collection of information, including suggestions for reducing this burden, to Washington Headquarters Services, Directorate for Information Operations and Reports, 1215 Jefferson Davis Highway, Suite 1204, Arlington, VA 22202-4302, and to the Office of Management and Budget, Paperwork Reduction Project (0704-0188), Washington, DC 20503.

| 1. AGENCY USE ONLY (Leave blank) | 2. REPORT DATE<br>July 1994 | 3. REPORT TYPE AND DATES COVERED<br>Technical Memorandum |
|---|---|---|

**4. TITLE AND SUBTITLE**
Differential Absorption Lidar Measurements of Atmospheric Water Vapor Using a Pseudonoise Code Modulated AlGaAs Laser

**5. FUNDING NUMBERS**
924

**6. AUTHOR(S)**
Jonathan A.R. Rall

**7. PERFORMING ORGANIZATION NAME(S) AND ADDRESS(ES)**
Goddard Space Flight Center
Greenbelt, Maryland 20771

**8. PERFORMING ORGANIZATION REPORT NUMBER**
94B00103

**9. SPONSORING/MONITORING AGENCY NAME(S) AND ADDRESS(ES)**
National Aeronautics and Space Administration
Washington, D.C. 20546-0001

**10. SPONSORING/MONITORING AGENCY REPORT NUMBER**
TM-104610

**11. SUPPLEMENTARY NOTES**

**12a. DISTRIBUTION/AVAILABILITY STATEMENT**
Unclassified–Unlimited
Subject Category 43
Report available from the NASA Center for AeroSpace Information, 800 Elkridge Landing Road, Linthicum Heights, MD 21090; (301) 621-0390.

**12b. DISTRIBUTION CODE**

**13. ABSTRACT (Maximum 200 words)**

Lidar measurements using pseudonoise code modulated AlGaAs lasers are reported. Horizontal path lidar measurements were made at night to terrestrial targets at ranges of 5 and 13 km with 35 mW of average power and integration times of one second. Cloud and aerosol lidar measurements were made to thin cirrus clouds at 13 km altitude with Rayleigh (molecular) backscatter evident up to 9 km. Average transmitter power was 35 mW and measurement integration time was 20 minutes. An AlGaAs laser was used to characterize spectral properties of water vapor absorption lines at 811.617, 816.024, and 815.769 nm in a multipass absorption cell using derivative spectroscopy techniques. Frequency locking of an AlGaAs laser to a water vapor absorption line was achieved with a laser center frequency stability measured to better than one-fifth of the water vapor Doppler linewidth over several minutes. Differential absorption lidar measurements of atmospheric water vapor were made in both integrated path and range-resolved modes using an externally modulated AlGaAs laser. Mean water vapor number density was estimated from both integrated path and range-resolved DIAL measurements and agreed with measured humidity values to within 6.5% and 20%, respectively. Error sources were identified and their effects on estimates of water vapor number density calculated.

**14. SUBJECT TERMS**
Lidar, AlGaAs Lasers

**15. NUMBER OF PAGES**
153

**16. PRICE CODE**

| 17. SECURITY CLASSIFICATION OF REPORT | 18. SECURITY CLASSIFICATION OF THIS PAGE | 19. SECURITY CLASSIFICATION OF ABSTRACT | 20. LIMITATION OF ABSTRACT |
|---|---|---|---|
| Unclassified | Unclassified | Unclassified | Unlimited |